SANDIA REPORT
SAND2019-11696
Printed October 2019

Sandia National Laboratories

Geomechanical Simulation of Big Hill Strategic Petroleum Reserve - Calibration of Model Containing Shear Zone

Byoung Yoon Park

Prepared by
Sandia National Laboratories
Albuquerque, New Mexico
87185 and Livermore,
California 94550

Issued by Sandia National Laboratories, operated for the United States Department of Energy by National Technology & Engineering Solutions of Sandia, LLC.

Available to DOE and DOE contractors from
U.S. Department of Energy
Office of Scientific and Technical Information
P.O. Box 62
Oak Ridge, TN 37831

Telephone: (865) 576-8401
Facsimile: (865) 576-5728
E-Mail: reports@osti.gov
Online ordering: http://www.osti.gov/scitech

Available to the public from
U.S. Department of Commerce
National Technical Information Service
5301 Shawnee Rd
Alexandria, VA 22312

Telephone: (800) 553-6847
Facsimile: (703) 605-6900
E-Mail: orders@ntis.gov
Online order: https://classic.ntis.gov/help/order-methods/

ABSTRACT

A finite element numerical analysis model, that consists of a realistic mesh capturing the geometries of Big Hill (BH) Strategic Petroleum Reserve (SPR) site using the multi-mechanism deformation (M-D) salt constitutive model and including data taken daily of the wellhead pressure and level of the oil-brine interface, has been upgraded. The upgraded model contains the shear zone to examine the interbed behavior in a realistic manner. The salt creep rate is not uniform in the salt dome, and creep test data for BH salt is limited. Therefore, a model calibration is necessary to simulate the geomechanical behavior of the salt dome. Cavern volumetric closures of SPR caverns calculated from sonar survey reports are used for the field baseline measurement. The structure factor, A_2, and transient strain limit factor, K_0, in the M-D constitutive model are used for model calibration. An A_2 value obtained experimentally from the BH salt and K_0 value of WIPP salt are used as the baseline values. To adjust the magnitude of A_2 and K_0, multiplication factors *A2F* and *K0F* are defined, respectively. The *A2F* and *K0F* values of the salt dome and salt drawdown layer of elements surrounding each SPR cavern have been determined through a number of back fitting analyses. The trendlines of the predictions and sonar data match up well for BH 101, 103, 104, 106, 110, 111, 112, and 113. The prediction curves are close to the sonar data for BH 102 and 114. However, the prediction curves for BH 105, 107, 108, and 109 are not close to the sonar data. An inconsistency was found in the sonar data, i.e. the volume measured later is larger than that before in some time intervals, even if the leached volume is taken into account, for BH 101, 104, 106, 107, and 112. Project discussions are needed to determine possibilities on how to resolve the issues and determine the best path forward for future computer modeling attempts.

ACKNOWLEDGMENTS

This research is funded by SPR programs administered by the Office of Fossil Energy of the U.S. Department of Energy.
The author would like to thank Steven R. Sobolik of Sandia provided technical reviews. Barry Roberts and David Hart of Sandia provided the seismic and sonar data for meshing the dome and caverns; and the raw water movements data, respectively. Sandia department manager Donald Conley and Sandia SPR project manager Anna C. Snider Lord who supported this work. As always, the support of Diane Willard of DOE is greatly appreciated. Paul Malphurs of DOE also is greatly appreciated, as is his comprehensive review of this report. This report has been improved by these individuals.

CONTENTS

LIST OF FIGURES

LIST OF TABLES

This page left blank

ACRONYMS AND DEFINITIONS

Abbreviation	Definition
3D	Three-Dimensional
bbl	Barrel
BC	Bayou Choctaw
BH	Big Hill
D-P	Drucker-Prager
DOE	U.S. Department of Energy
EFF	Extended File Format
E-W	East-West
FE	Finite Element
ID	Identification
M-D	Multi-Mechanism Deformation
MIT	Mechanical Integrity Test
MMB	Million Barrels
EVS	Earth Volumetric Studio
N-S	North-South
NTESS	National Technology & Engineering Solutions of Sandia, LLC
OBI	Oil-Brine Interface
ONI	Oil-Nitrogen Interface
PLC	Power Law Creep
Sandia	Sandia National Laboratories
SMF	Structure factor Multiplication Factor
SPR	Strategic Petroleum Reserve
WIPP	Waste Isolation Pilot Plant

This page left blank

1. INTRODUCTION

1.1. Background

As of December 31, 2018, the U.S. Strategic Petroleum Reserve (SPR) held 649 million barrels (MMB) of crude oil stored in 60 underground salt dome storage caverns at four storage sites along the nation's Gulf Coast. Most of the caverns were solution mined by the U.S. Department of Energy (DOE) and are typified as cylindrical in shape. Sandia National Laboratories (hereafter 'Sandia'), on behalf of DOE, evaluates the structural integrity of the salt surrounding existing petroleum storage caverns in the Big Hill (BH) Salt Dome in Texas (Figure 1). The integrity of wellbores at the interbed between the caprock and salt is a concern because oil leaks occurred at the interbed in the Big Hill site [Park, 2014a and 2014b]. When oil is withdrawn from a cavern in salt using freshwater, the cavern enlarges. As a result, the pillar separating caverns in the SPR fields is reduced over time due to usage of the reserve. The enlarged cavern diameters and smaller pillars reduce underground stability [Park and Ehgartner, 2011]. It is necessary to establish a limit for the remaining pillar thickness between caverns without threatening the structural integrity of the caverns.

Figure 1. Big Hill Strategic Petroleum Reserve site location map

1.2. Objective

Sandia uses large-scale, three-dimensional (3D) computational models to model the geomechanical behavior of underground storage facilities consisting of solution-mined caverns in salt domes. Recent advances in the state-of-art in geomechanics modeling have enabled 3D analyses to be performed. 3D analyses capture the actual geometry and layout of a cavern field and result in more realistic simulations. The complexities within the BH cavern field require such advanced simulations as the field has a long history of development resulting in 14 caverns of various shapes, depths, and

states. This report attempts to model these conditions and addresses the resulting performance and stability issues.

Park and Roberts [2015] and Park et al. [2017] developed a three-dimensional finite element (FE) mesh capturing realistic geometries of Bayou Choctaw (BC) site was constructed using sonar, seismic, and borehole survey data obtained from the field. The steps and methodologies developed from the BC mesh are applied to construct the mesh of Big Hill site. The mesh consists of hexahedral elements because the salt constitutive model is coded using hexahedral elements. This report describes the model calibration to match the analysis results to the field observations

1.3. Advancement

There are several important advances in this new computational simulation over the historical simulations:

1. This simulation uses a three-dimensional finite element mesh capturing realistic geometries of the salt dome and caverns at the BH site. The process of converting complex cavern and dome geometries obtained from seismic and sonar measurements, into a finite element mesh suitable for large-scale geomechanical calculation of site performance, has evolved substantially over the past 28 years. Advances by Park and Roberts [2015] and Park et al. [2017] to create highly-realistic mesh geometries has improved our capability to understand complex physical processes, for example the stability of caverns in close proximity of the caverns to each other or to the salt dome boundary. In the previous models [Park et al., 2005; Park et al. 2006; Park and Ehgartner, 2012; Park, 2014a; Park, 2014b; Park et al., 2014], the shapes of all caverns were simplified by cylindrical shapes and an elliptical shape was applied to the section of the dome as an approximation for the actual shape of the dome.
2. This simulation uses the multi-mechanism deformation (M-D) model as a salt constitutive model. The previous analyses [Park et al., 2005; Park et al. 2006; Park and Ehgartner, 2012; Park, 2014a; Park, 2014b; Park et al., 2014] were conducted using the Power Law Creep (PLC) model. The PLC, a subset of M-D, considers only the secondary creep rate (steady-state, long term), while M-D considers not only the secondary but also the primary (initial stage, short term) and tertiary (beyond steady-state) creep rates. The M-D should provide more accurate numerical predictions considering the short term salt behaviors due to the daily changes of internal pressure of the caverns.
3. This simulation considers the interbed between the caprock and salt top, and the interface between the salt dome and surrounding in situ rock stratigraphy. The interbed will be used to check the integrity of wellbores at the salt top. The interface will allow for evaluating various models of the deformation and integrity of the salt dome boundary with the surrounding host rock.
4. A major shear zone (fault) extends approximately North-South along the entire length of the caprock and for an unknown depth into the salt. This fault zone has a pronounced effect on the subsidence measured above the site and is a consideration for future cavern placement [Ehgartner and Bauer, 2004]. The fault, which was ignored for the simplification in previous analyses [Park, 2018], is included in this model to perhaps better represent the large scale deformation considered in this study.

5. This simulation uses the daily wellhead pressure histories of SPR caverns that were recorded by the field office. The real wellhead pressure plus the oil/brine pressure gradient was applied on the inside boundary of each SPR cavern as a function of depth. The cavern internal pressure acts against the lithostatic pressure to impede the inward movement of the wall, floor, and roof of the cavern due to salt creep. The previous simulation used a simplified wellhead pressure given by an average pressure over a time period under normal operating conditions for each cavern. Zero wellhead pressure was used for workover[1] conditions.
6. This simulation considers the oil-brine interface (OBI) depth change over time. Previous analyses assumed that the SPR caverns were filled fully with oil. In reality however, the caverns were not always fully filled with oil. Brine filled the bottom portion of the cavern, and the brine volume changes with time. The difference between pressure gradients of oil (0.37 psi/ft of depth) and brine (0.52 psi/ft of depth) cannot be ignored. So, the amount of oil and brine in a cavern over time were considered.

1.4. Software

Create geometries and mesh generation:

Cubit 15.4.0 Software Build 415298 (64 bit)
Revised 2019-04-19
Copyright 2001 National Technology & Engineering Solutions of Sandia, LLC (NTESS)

Combine meshed blocks:

GJoin2 Version 1.34 (A GENESIS database combination program)
Revised 2016/09/06
Copyright 1988 NTESS

Solver:

SIERRA ADAGIO Version 4.48.2 (A 3-D Nonlinear Solid Mechanics Finite Element Application for Quasistatic, Implicit Transient Dynamics, and Explicit Transient Dynamics). ADAGIO is written for parallel computing environments, and its solvers allow for scalable solutions of very large problems. ADAGIO uses the SIERRA Framework, which allows for coupling with other SIERRA mechanics codes [SIERRA Solid Mechanics Team, 2018].
Copyright NTESS

Post-processors:

ParaView Version 5.4.1 64-bit (An open-source, multi-platform scientific data analysis and visualization tool that enables analysis and visualization of extremely large datasets)
Copyright (c) 2005-2017 NTESS, Kitware Inc.

Algebra Version 1.47 (An Algebraic Manipulation Program for Post-Processing of Finite Element Analyses Exodus II Version)
Revised 2019/01/25
Copyright 2008 NTESS
Sandia National Laboratories, New Mexico PO Box 5800 Albuquerque, NM 87185

[1] "Workover" is when the wellhead pressure of the cavern is dropped to atmospheric pressure for maintenance.

Blot II-2 Version 3.13 (A Deformed Mesh / Contour Plot Program with X-Y Plotting Capabilities for Post-Processing of Finite Element Analyses)
Revised 2018/09/17

2. SITE DESCRIPTIONS

Figure 2 shows a plan view of the BH site with contour lines defining the approximate location of the salt dome top. The locations of fourteen SPR caverns currently in-use (101-114). The figure also specifies the undeveloped area north of the DOE property line (Sabine Pass Terminal). The horizontal shape of the dome is approximated as being elliptical. The major and minor ellipse axes are measured as approximately 7000 ft and 5800 ft, respectively.

The West-East cross-section #1 through the northern-most row of caverns (Cavern 101-105) provides a geologic representation near the middle of the dome (Figure 3). The site has a thin overburden layer consisting of sandy soil; and an exceptionally thick caprock sequence comprised of two layers. The upper caprock is comprised mainly of gypsum and limestone, whereas the lower caprock is mostly anhydrite.

A major fault (shear zone) extends approximately North-South along the entire length of the caprock and for an unknown depth into the salt. This fault zone has a pronounced effect on the subsidence measured above the site and is a consideration for future cavern placement [Ehgartner and Bauer, 2004]. The salt dome is essentially two large salt spines. The two masses of salt are operating somewhat independently and while pushing up creating the shear zone separating the two spines and resulting in faulting in the caprock above. The shear zone is a region separating two salt spines, typically characterized by containing impurities, compositional changes, physical property variations, and possibly inclusions of hydrocarbons [Snider Lord, 2019].

Figure 4 shows a three dimensional representation of the BH salt dome constructed by digitally piecing together the separate models of the flank and top of salt. Figure 5 shows the salt dome with caprock as viewed from North-East. For numerical analysis purposes, the top layer of overburden is modeled as having a thickness of 300 ft, the upper caprock 900 ft thick, and the lower caprock 420 ft thick. The interbed layer of 20 ft thick is assumed to exist between the lower caprock and salt dome. The bottom boundary of the present analysis model is set at 6000 ft below the ground surface, so the height of salt dome is 4360 ft.

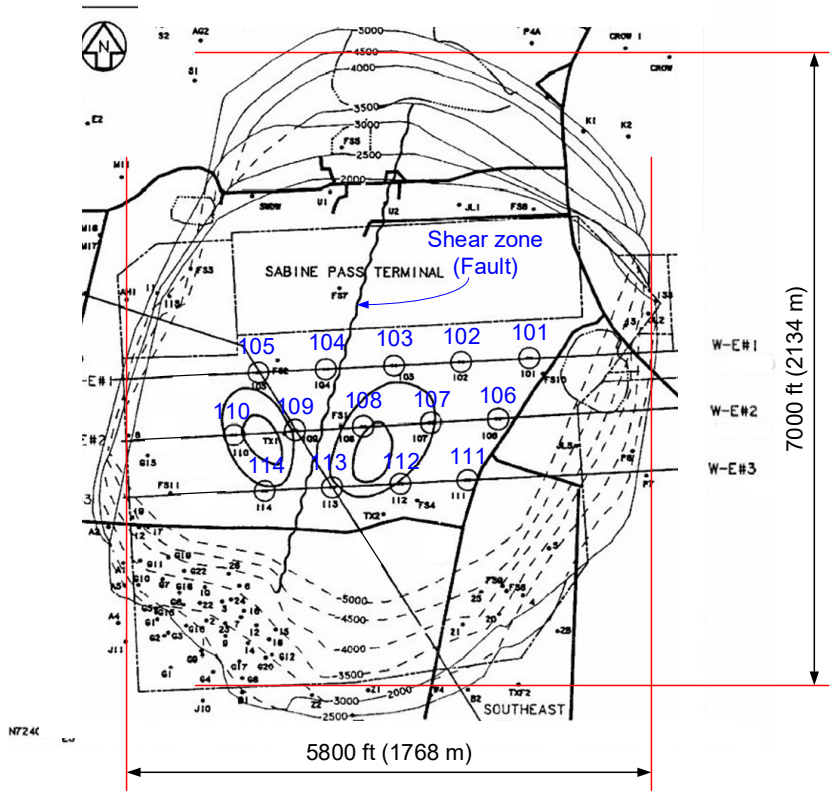

Figure 2. Big Hill site plan view [Magorian and Neal, 1988]

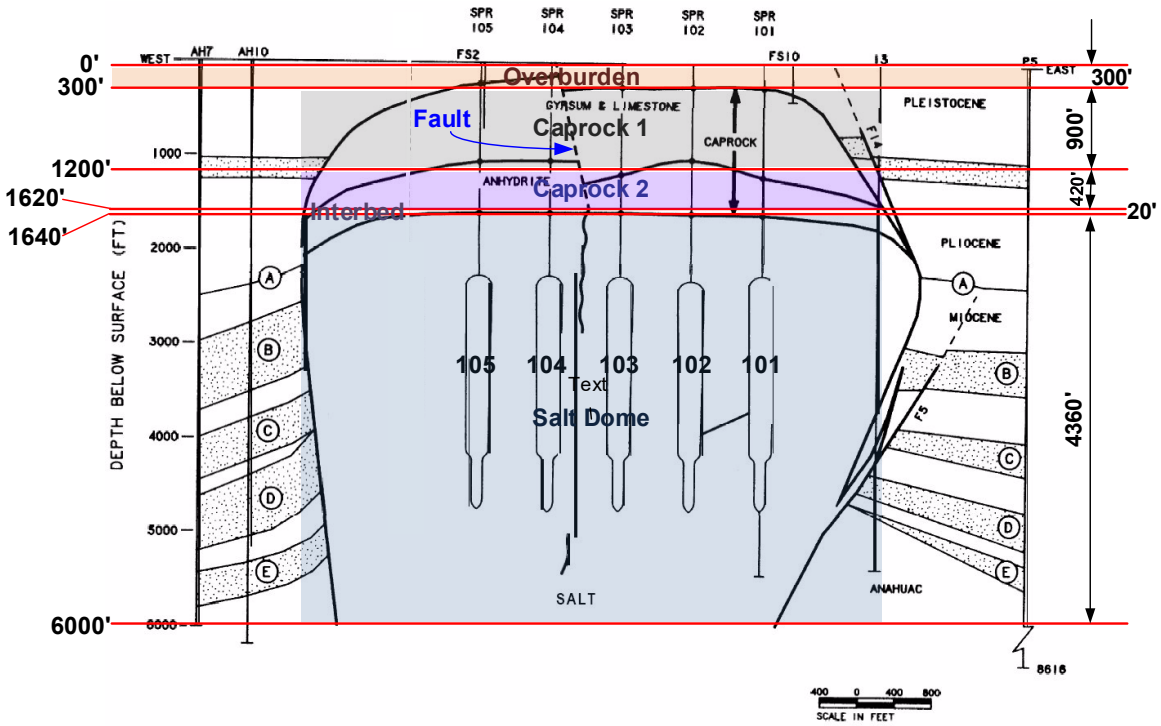

Figure 3. Cross-section (W-E #1 in Figure 2) near middle of dome [Magorian and Neal, 1988] looking North.

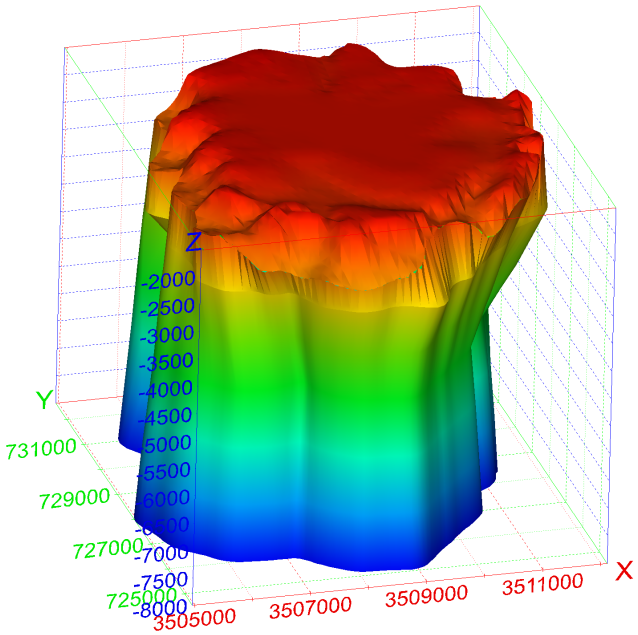

Figure 4: Three dimensional representation of the Big Hill salt dome. The color depicts the elevation. No overburden or caprock is shown.

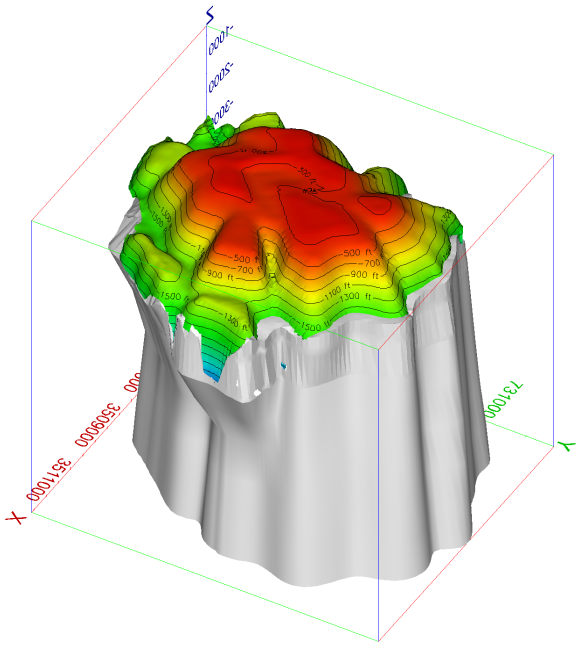

Figure 5: View of the caprock colored by elevation. The salt dome is shown in grey. View is from North-East at an inclination of 40º from the horizontal.

This page left blank

3. GEOMETRIC CONDITIONS

3.1. Basic Rules for Meshing

Finite element codes such as SIERRA/ADAGIO are designed to conduct simulations with finite elements that are either tetrahedral or hexahedral. Two constitutive material models, i.e. the Power Law Creep (PLC) model and the Multi-Mechanism Deformation (M-D) model, are available in ADAGIO to represent salt behavior. These two material models are programmed in SIERRA/ADAGIO using eight-node hexahedral elements. Therefore, the mesh for the BH SPR site must be constructed with hexahedral elements. Hexahedral elements include six convex quadrilateral sides, or facets, with the eight corners where these facets intersect being the eight nodes for the element. The cavern boundaries such as the ceiling, wall, and floor are obtained from sonar measurements, and the irregular geometries of these boundaries ultimately require various shapes of facets. Similarly, the geometry of the flank of the salt dome, obtained from seismic measurements, also consists of complicated shapes of facets. To construct a mesh with convex hexahedral elements for a geological volume keeping the complicated geometry as much as possible, the following rules were established and followed:

1. Each perimeter (cavern and dome) consists of the same number of vertices at each depth interval
2. The reference distance between vertices on a perimeter is:
    a. about 20 ft for caverns
    b. about 120 ft for dome
3. The vertical thickness of an element level is kept constant at 20 ft
4. A 16% cavern volumetric increase is used for each drawdown leach

Modeling of the leaching process of the caverns is performed by deleting a pre-meshed layers of elements that make up the walls of the cavern so that the cavern volume is increased by 16 percent per drawdown. A 15% volume increase is typical for a standard freshwater drawdown, but the BH salt quality is different from that of other sites. So a 16% volume increase is used for a drawdown. Also, typical leaching processes tend to increase a cavern radius more at the bottom of the cavern than at the top, with very little change to the roof and floor of the cavern, however this little change is ignored in this model. For the purposes of this modeling effort for Big Hill, leaching is assumed to add 16% to the volume of the cavern, and is assumed to occur uniformly along the entire height of the cavern, with no leaching in the floor or roof of the caverns. Each leaching layer, or onion skin, is built around the perimeter of the meshed cavern volume using the same rules stated previously. The detailed steps and methodologies to construct the FE mesh were provided by Park and Roberts [2015].

3.2. Salt Dome

The salt dome image is generated using the seismic data and 4DIM[2] tool. The three-dimensional hexahedral FE mesh is constructed using the seismic data and the CUBIT mesh generation tool as shown Figure 6. The 3D-coordinates of vertices are resampled from the seismic image. The real salt

[2] Four-Dimensional Interactive Model Player developed by C Tech.

dome top is not flat as shown in the seismic image. The uneven top surface should create poorly shaped elements. To avoid a poor shape, the vertex data above the elevation of -2240 ft are removed (a process called 'trimming'). The vertex data for the upper salt blocks are translated vertically upward up to -1640 ft from the vertex data of the top of trimmed salt dome block (-2240 ft). The dome mesh consists of 218 element levels each 20 ft thick. The bottom elevation is -6000 ft. The trace of the shear zone is shown on the top of the FE mesh.

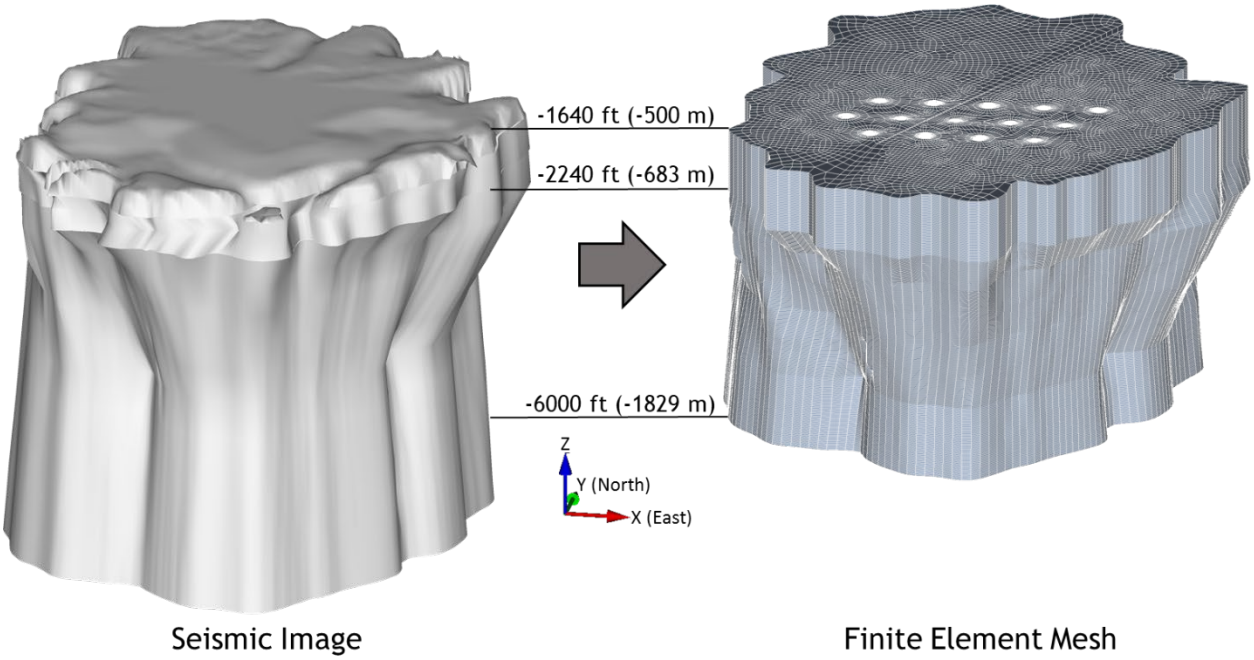

Figure 6 Images of Big Hill salt dome obtained from the seismic survey (left) and hexahedral finite element mesh using the seismic survey data

3.3. Lithologies Surrounding the Salt Dome

3.3.1. Overburden

The top layer of overburden, which consists of sand and soil, has a thickness of 300 ft. The bottom of the overburden layer (top of the caprock) is not flat as shown in Figure 3 and Figure 5. The bottom is simplified as a flat to avoid creating poorly-shaped elements. Figure 7 shows the meshed overburden block that is 12,400 ft width, 14,600 ft depth, and 300 ft thick. The thickness of each element layer is 20 ft, so the mesh has 15 element levels vertically.

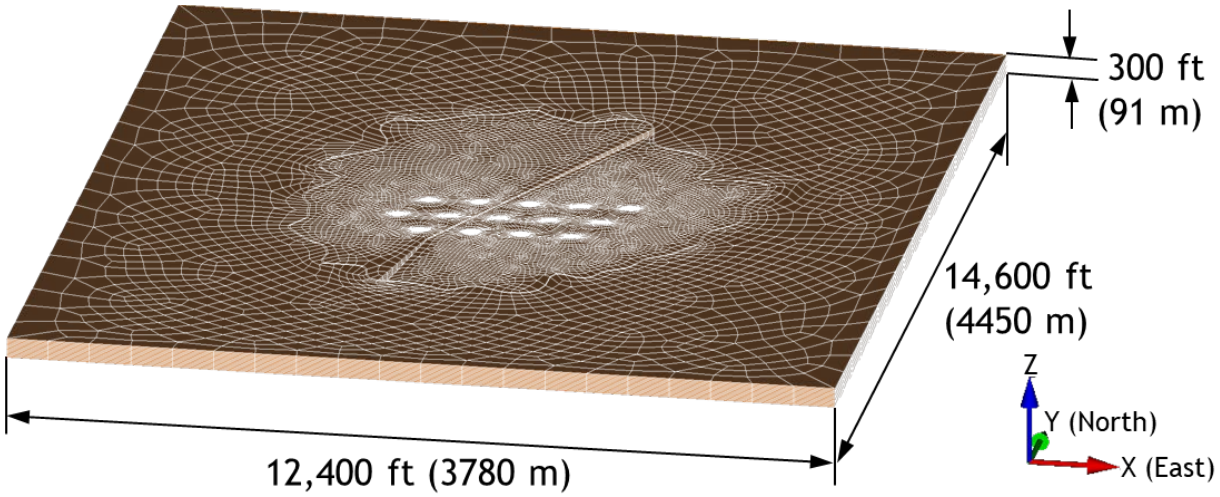

Figure 7 Overburden meshed block

3.3.2. Caprock

Two layers of caprock exist over the BH salt dome. The upper caprock, consisting of gypsum and limestone, is 900 ft thick. The lower caprock, consisting of anhydrite, is 420 ft thick as shown Figure 3. Figure 8 shows the BH caprock image and hexahedral FE mesh. The image was generated using the seismic and borehole data with the 4DIM tool. Since the seismic is hard to differentiate between the caprock and salt, the caprock map relied heavily on borehole data, but would have been tweaked based on the mapping of the salt with seismic and borehole control. The bottom of the caprock surface is based on the topography of the salt dome top. The actual caprock top and bottom are not flat. The uneven top and bottom may produce poorly-shaped elements. To avoid a poor shape, the vertex data for the caprock are translated vertically upward from the vertex data of the flat surface of salt dome top as shown in Figure 6. The thickness of each element layer is 20 ft in this model, so the meshes for the upper and lower caprocks have 45 and 21 element levels vertically, respectively, because the upper and lower caprock layers are simplified as flat slice blocks 900 ft and 420 ft thick for the numerical model as shown in Figure 8.

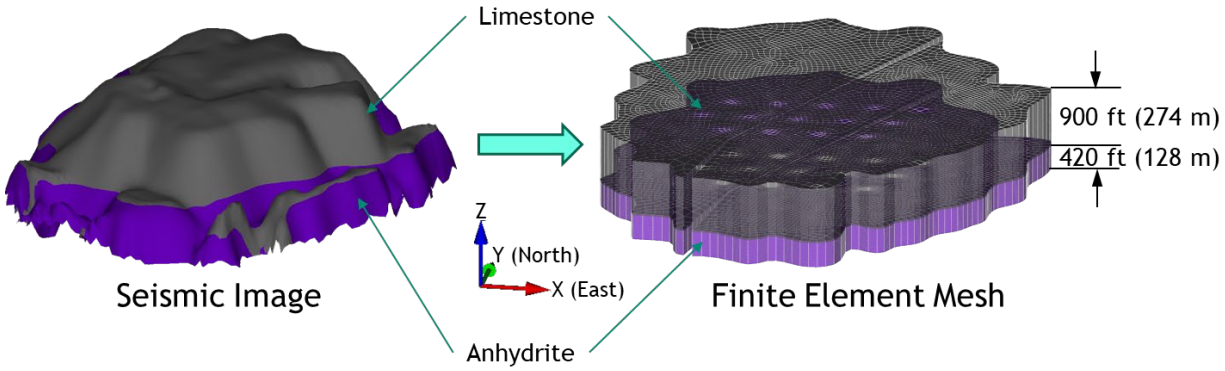

Figure 8 Image of Big Hill caprock obtained from the seismic and borehole survey (left) and hexahedral finite element mesh

3.3.3. Interbed

Loss of integrity were found in wellbores of Caverns 105 and 109 at the Big Hill SPR site in 2009 and 2010, respectively. According to the field observations, two instances of casing damage occurred at the depth of the interbed between the caprock bottom and salt top. A three dimensional finite element model was constructed to investigate horizontal and vertical displacements in each well as it crosses the interbed [Park, 2014a and 2014b]. The analysis results indicate that the casings of Caverns 105 and 109 failed, respectively, from shear stress that exceeded the casing shear strength due to the horizontal movement of the salt top relative to the caprock, and tensile stress due to the downward movement of the salt top from the caprock. The salt top subsides because the volumes of caverns in the salt dome decrease with time due to salt creep closure, while the caprock does not subside at the same rate as the salt top because the caprock is thick and stiff. This discrepancy causes deformation in the wells. ADAGIO has a contact surface algorithm for modeling contact and sliding behavior between two solid surfaces. However, this algorithm has a limitation on the number of elements in the model. The number of elements in the BH model was over the limit. In place of a contact surface, a thin soft layer of elements is used for the interface between lithologies. The thin, soft element layer is assumed to behave mechanically like a contact surface from a perspective of relative displacement between two lithologies [Park, 2014a and 2014b].

A similar interbed layer is implemented in the new model to represent the salt/caprock contact in this report. The contact zone is modeled by a thin, soft element interbed layer block to evaluate the caverns' geomechanical effect on wellbore integrity. Figure 9 shows the BH interbed FE mesh. The real interbed between the salt dome and caprock is not flat. The uneven interbed could cause poorly-shaped element to be generated. To avoid a poor shape, the vertex data for the interbed are translated vertically upward from the vertex data of the simplified flat surface of salt dome top. The thickness of interbed layer is assumed to be 20 ft, so it has one element level.

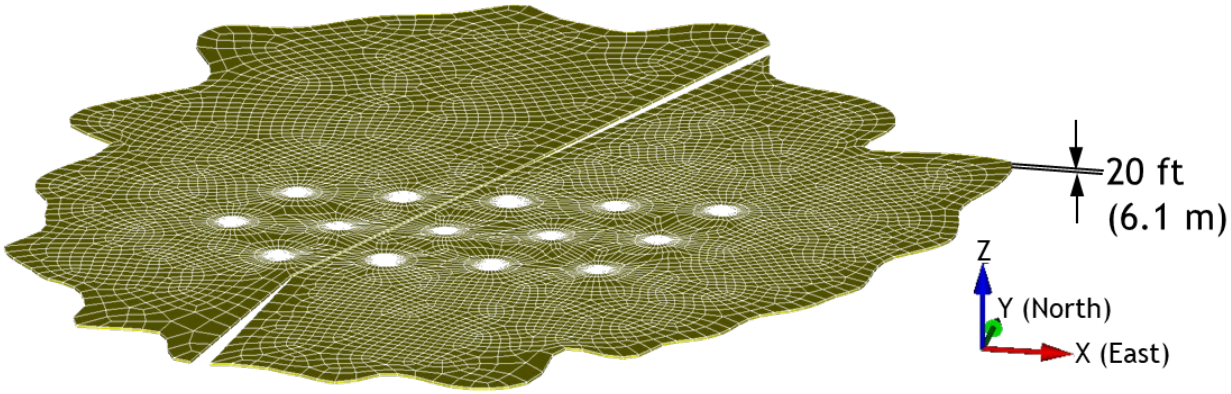

Figure 9 Finite element mesh of interbed between caprock and salt top

3.3.4. Shear zone (Fault)

The major fault (shear zone), which was ignored for the simplification in previous analyses [Park, 2018], is included in this model to perhaps better represent the large scale deformation considered in this study. To realize the fault which extends approximately North-South along the entire length of the caprock and for an unknown depth into the salt as show in Figure 2, the fault block as shown in Figure 10 is inserted into the previous model by Park [2018]. The shear zone in the salt dome is a region separating two salt spines, typically characterized by containing impurities, compositional changes, physical property variations, and possibly inclusions of hydrocarbons [Snider Lord, 2019].

It is assumed that the fault extends from the surface to the salt top. The fault only in the caprock layers is considered in this study, since we do not know the depth of it in the salt dome. The comparison of the results between with and without considering the shear zone in the salt dome will be provided in a follow-up report.

The meshed fault is not straight, and its width is increasing as far away from the cavern area, while the fault trace in Figure 2 is straight. These are to avoid the technical troubles during the construction of mesh. The troubles create the negative shape of mesh which is not hexahedral, and complicate the process of generating the mesh. The details of generation techniques are omitted in this report. However, the analysis result may not be affected significantly since the fault block is straight in the cavern area. The cavern area means the range through which the fault block passes between caverns.

There is no fault geometry and material property data obtained from the BH field. Individual faults may vary in thickness from a few millimeters to a kilometer or more as shown Figure 11 [Hull, 1988; Shipton et al., 2006]. In this study, the width of the fault block is assumed to be a uniform 20 ft in the range across the cavern area.

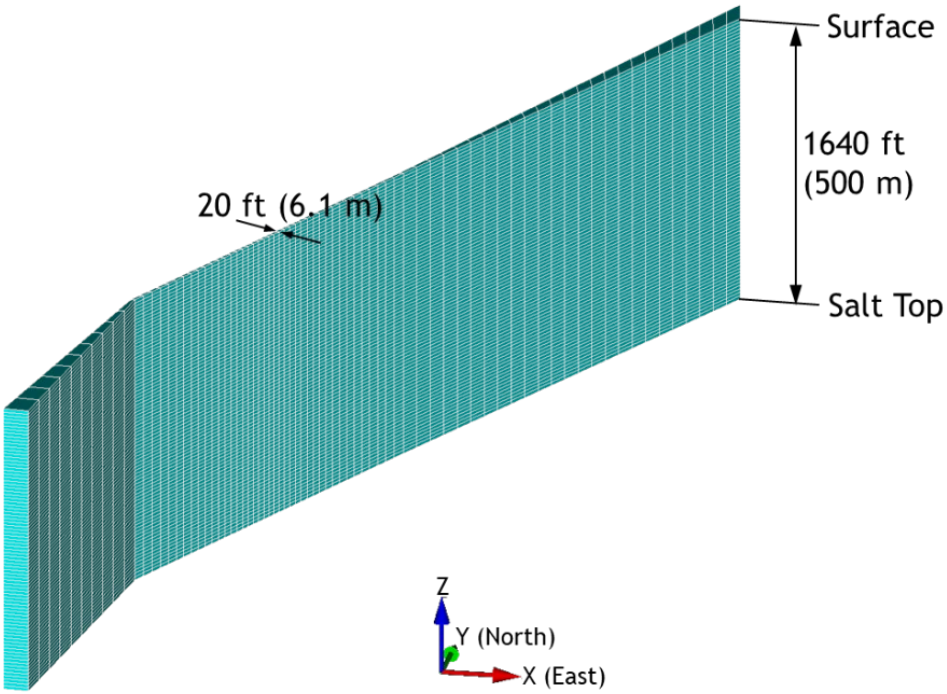

Figure 10. Finite element mesh of shear zone from surface through salt top

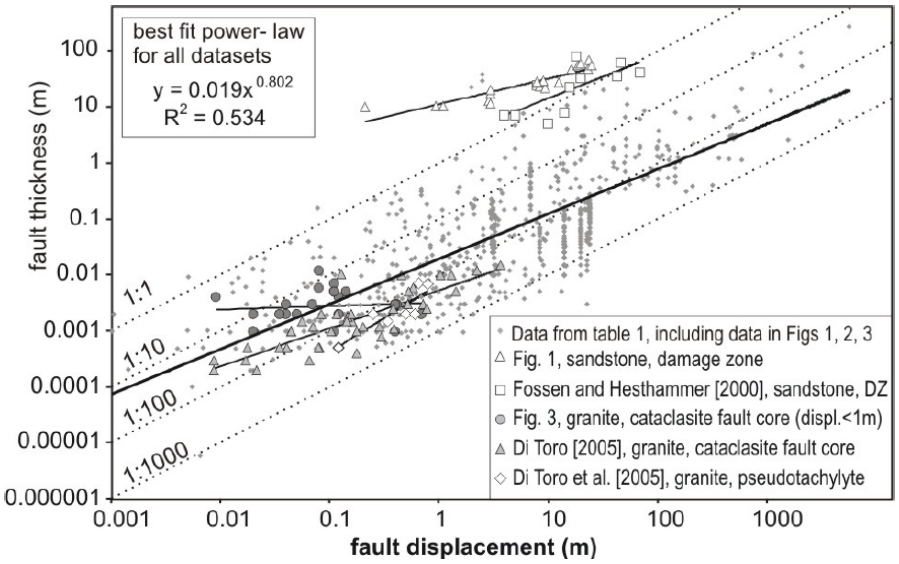

Figure 11. Log-log plot of a compilation of 16 fault thickness datasets reported in the literature including the data used by Hull [1988], and the three datasets in Shipton, et al. [2006].

3.3.5. Interface between dome and far-field

The salt dome is a piercement structure which has penetrated Mesozoic through Quaternary sediments. As in other types of intrusions, the salt dome must displace the overlying sediments as it pushes upward. Any sediment deposited above the dome must be either pushed aside and/or lifted up, increasing the chance of erosion occurring on the loosened material. The mechanical failure of the sediments surrounding the dome has caused faults to develop both radially from and tangentially to the dome in a series of graben-horst structures [Hogan, 1980]. To consider the faults surrounding the dome, the interface block is inserted between the dome and sediments surrounding the dome which consists of the caprock, interbed, and salt dome blocks. As with the interbed block in Section3.3.3, a thin, soft layer of elements is used for the interface between lithologies, i.e. this model contains an interface block between the dome and surrounding sediments (hereafter 'surrounding' or 'far-field' rock) as shown Figure 12.

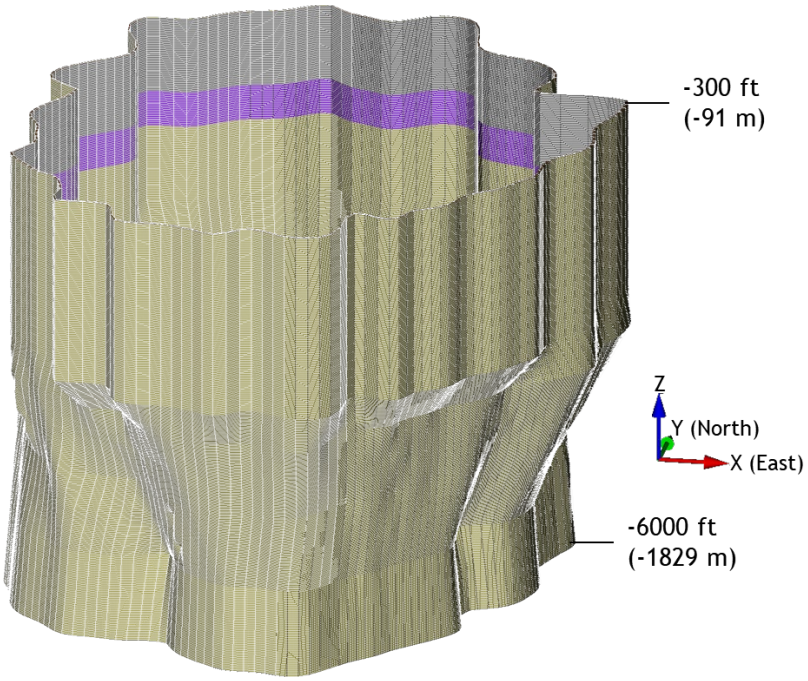

Figure 12 Finite element mesh of interface between dome and far-field

3.3.6. Far-field (Surrounding) rock

For simplification, the rock surrounding the salt dome is assumed to be made of an isotropic, homogeneous, linear elastic material in this model. The surrounding rock block encircles the interface, caprock, interbed, and salt dome blocks. The lengths of the confining boundaries are 14,600 ft (4450 m) in the N-S direction and 12,400 ft (3780 m) in the E-W direction as shown Figure 13. The sizes of the caverns are much smaller than the dome size,. So the model boundary distances (surrounding rock dimensions) can be regarded as being an infinite distance away from the caverns (i.e. fixed boundaries can be applied).

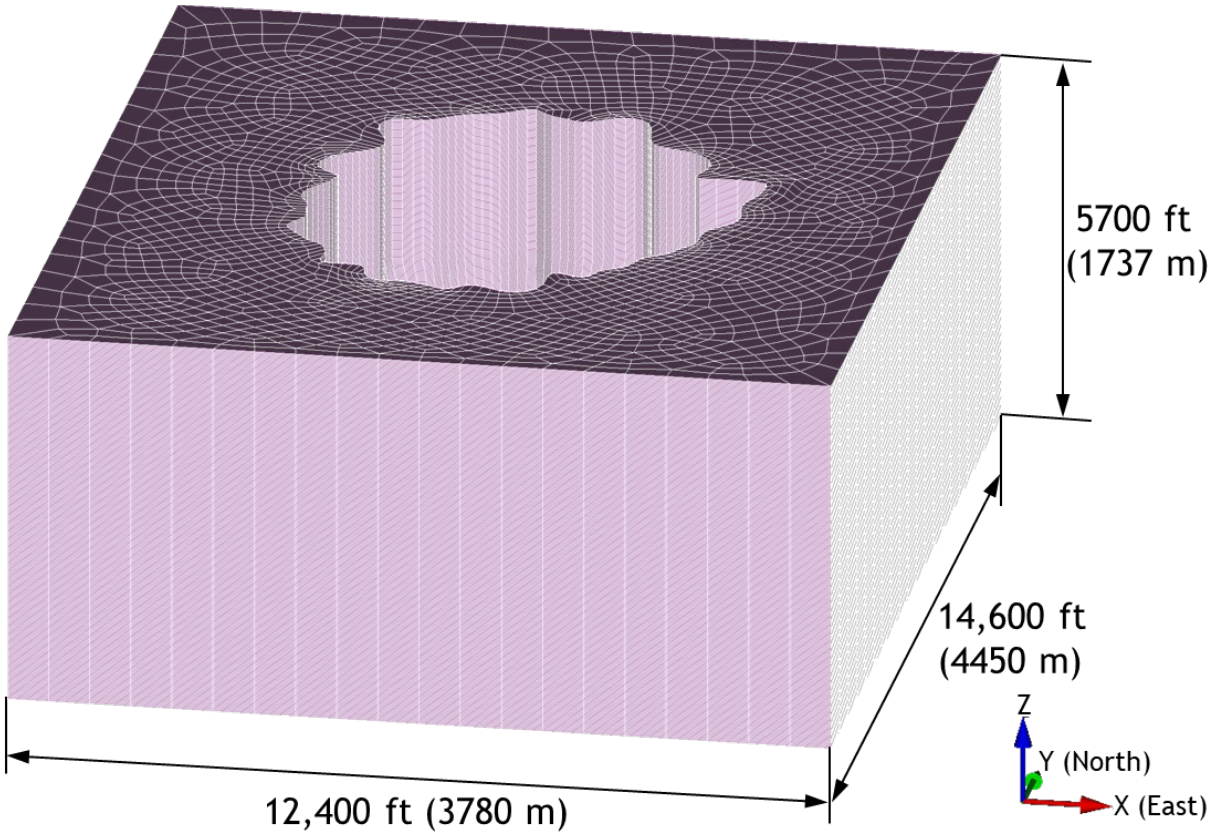

Figure 13. Finite element mesh of surrounding (far-field) rock

3.4. Caverns

Representations of the BH caverns based on sonar data were incorporated into the geomechanical model to provide a more realistic depiction of the caverns. To facilitate this, the cavern sonar data were resampled to a nodal spacing more appropriate for the geomechanical model. The actual sonar data is delivered from the sonar contactors. An additional processing code SONAR7[3] was used to turn these contractor files into a format compatible with the EVS[4] geologic modeling software suite. This is a mature process which has been used for many years at Sandia. This step is necessary to provide a full three-dimensional surface model of the sonar data. The assigned vertices in the FE mesh created in CUBIT need to be at specific depth intervals which may not correspond to the actual sonar sampling locations. Continuous three-dimensional surface models of the survey data are created, which allows sampling at any depth needed. This resampling step is performed through an algorithm coded using Python. Then, the resampled node coordinates data sets for the caverns are generated as the output in this step. The resampled nodal data are converted into CUBIT vertex data

[3] A data conversion program developed by Sandia. SONAR7 converts sonar data sets with various formats provided by different vendors into the extended file format (EFF) and other EVS compatible formats.
[4] EVS (Earth Volumetric Studio) is C Tech's flagship product for state-of-the art analysis and visualization. EVS was designed from the ground up to meet the demanding requirements of underground and surface mining analysis. Its tools are also used by civil engineers and advanced environmental modelers.

through another algorithm coded using Python. The mesh is constructed using cavern slice blocks of 20-ft thick layers generated using the coordinates of vertices.

Table 1 lists the elevations of cavern top and bottom, cavern volumes, and the dates when the sonar data were obtained. The cavern volumes calculated from SONAR7 and CUBIT are different. The SONAR7 volumes are calculated from the full three-dimensional surface model of the sonar data, while the CUBIT volumes are calculated from the FE discretized mesh. Typically, the CUBIT-generated volumes are slightly less than those from SONAR7 because the curved surfaces are converted into flat facets with four nodes, and the CUBIT volumes exclude the chimney on the top of caverns. The volume differences are usually less than 2%, so and their volume discrepancies are not expected to significantly affect the global salt behavior. The 3D hexahedral element meshes for 14 caverns constructed using various functions in CUBIT are shown in Figure 14.

Table 1 Elevations of cavern tops and bottoms, cavern volumes, and sonar survey dates.

Cavern ID	Sonar Survey Date	Top Elevation (ft)	Bottom Elevation (ft)	Volume (bbl)		Difference (B-A)/A
				Sonar7 (A)	Cubit (B)	
BH-101	09/11/2012	-2280	-4140	14,243,844	14,150,204	-0.66%
BH-102	08/29/2013	-2300	-4040	12,529,701	12,397,910	-1.05%
BH-103	04/23/2009	-2300	-3860	12,416,235	12,203,051	-1.72%
BH-104	05/02/2012	-2300	-4200	13,409,156	13,277,022	-0.99%
BH-105	07/16/2013	-2300	-4020	13,102,685	12,939,930	-1.24%
BH-106	02/23/2005	-2300	-4080	12,551,777	12,387,141	-1.31%
BH-107	08/19/2010	-2260	-4080	11,970,657	11,836,301	-1.12%
BH-108	03/09/2005	-2340	-4140	11,159,611	10,999,514	-1.43%
BH-109	03/08/2005	-2280	-4240	12,040,477	11,899,885	-1.17%
BH-110	03/01/2005	-2300	-4200	12,282,692	12,254,118	-0.23%
BH-111	03/02/2005	-2260	-4240	13,701,942	13,499,414	-1.48%
BH-112	04/04/2005	-2300	-4200	13,178,525	12,950,207	-1.73%
BH-113	02/22/2005	-2300	-4140	12,432,217	12,474,159	0.34%
BH-114	10/24/2013	-2340	-4100	12,574,022	12,330,903	-1.93%

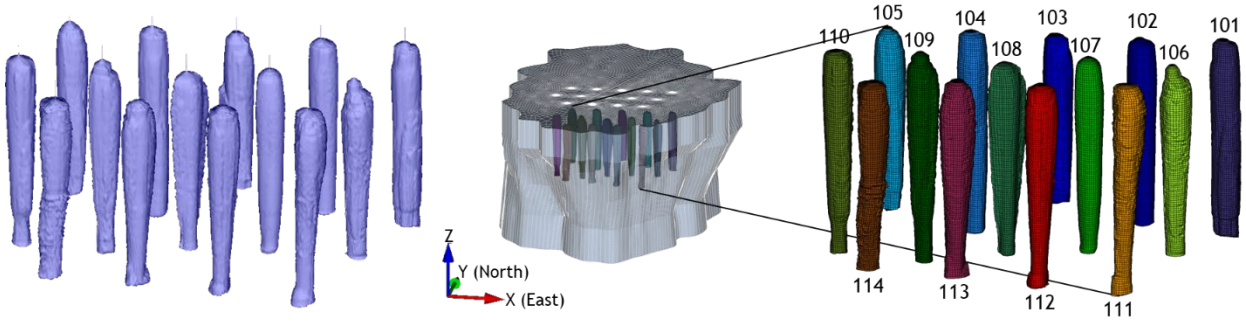

Figure 14 Sonar Images and hexahedral finite element meshed blocks of 14 caverns in the Big Hill salt dome. The cavern ID numbers are also shown.

As mentioned in Section 3.1, modeling of the leaching process of the caverns is performed by deleting a pre-meshed layer of elements along the walls of the cavern so that the cavern volume is increased by 16 percent per drawdown. Figure 15 shows the cavern cavities of BH101 through BH114 as developed from sonar data, along with drawdown layers (leaching onion skins) and extra layers. In this simulation, each SPR cavern is modeled as having five drawdown layers to be removed to account for the future oil drawdown activities.

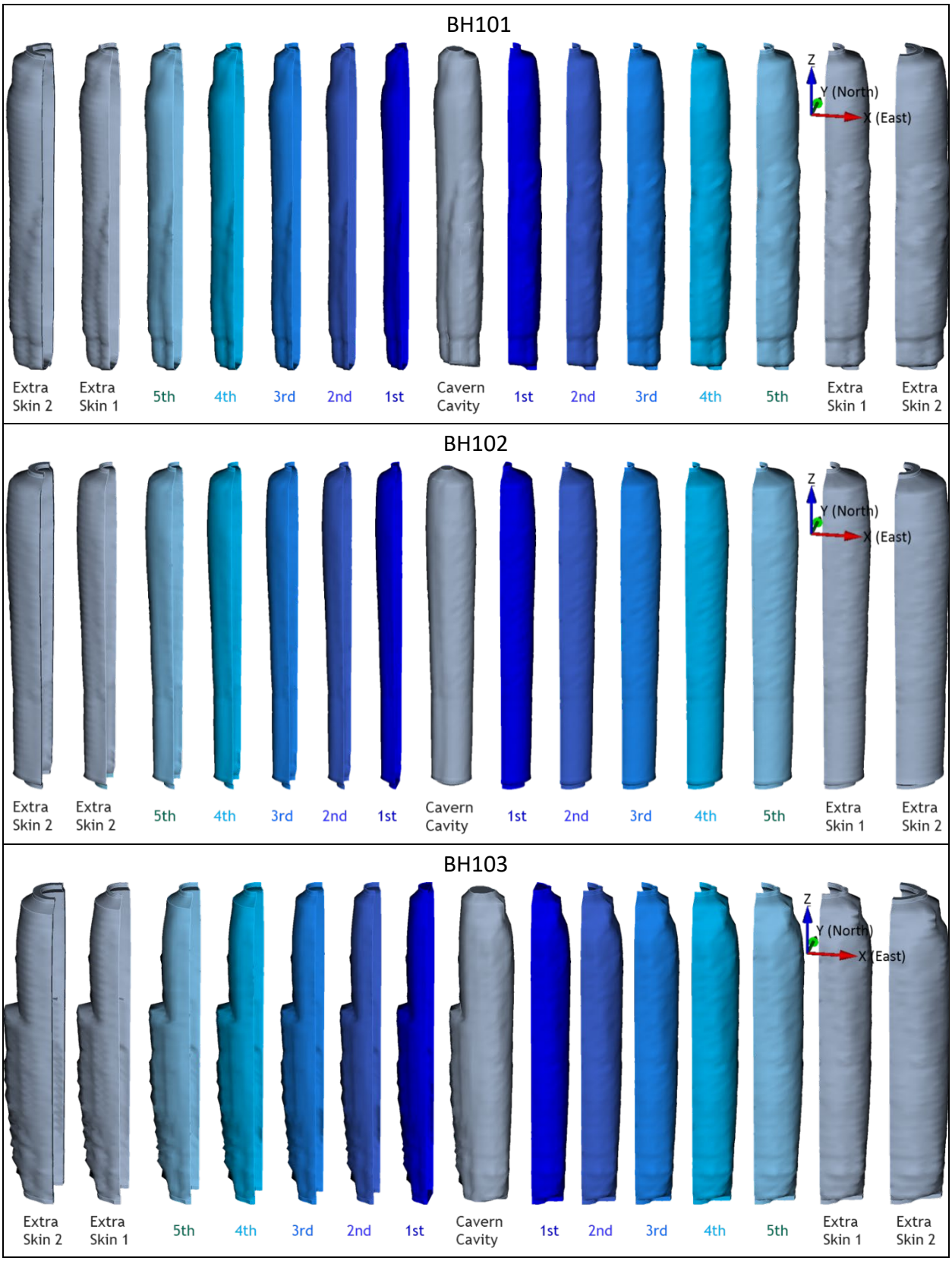
BH101
Z
Y (North)
X (East)
Extra Skin 2
Extra Skin 1
5th
4th
3rd
2nd
1st
Cavern Cavity
1st
2nd
3rd
4th
5th
Extra Skin 1
Extra Skin 2
BH102
Z
Y (North)
X (East)
Extra Skin 2
Extra Skin 2
5th
4th
3rd
2nd
1st
Cavern Cavity
1st
2nd
3rd
4th
5th
Extra Skin 1
Extra Skin 2
BH103
Z
Y (North)
X (East)
Extra Skin 2
Extra Skin 1
5th
4th
3rd
2nd
1st
Cavern Cavity
1st
2nd
3rd
4th
5th
Extra Skin 1
Extra Skin 2

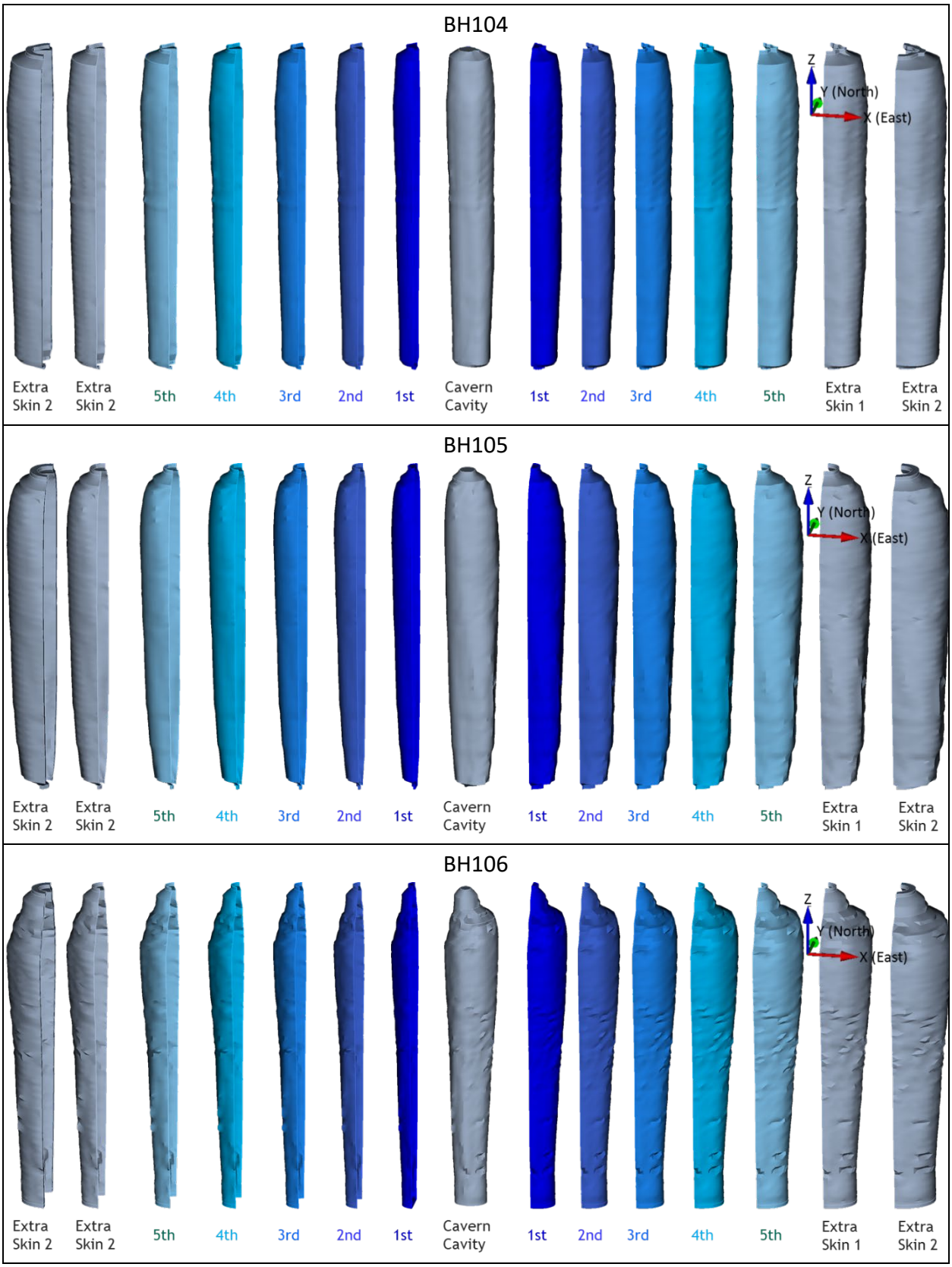
BH104
Z
Y (North)
X (East)
Extra Skin 2
Extra Skin 2
5th
4th
3rd
2nd
1st
Cavern Cavity
1st
2nd
3rd
4th
5th
Extra Skin 1
Extra Skin 2
BH105
Z
Y (North)
X (East)
Extra Skin 2
Extra Skin 2
5th
4th
3rd
2nd
1st
Cavern Cavity
1st
2nd
3rd
4th
5th
Extra Skin 1
Extra Skin 2
BH106
Z
Y (North)
X (East)
Extra Skin 2
Extra Skin 2
5th
4th
3rd
2nd
1st
Cavern Cavity
1st
2nd
3rd
4th
5th
Extra Skin 1
Extra Skin 2

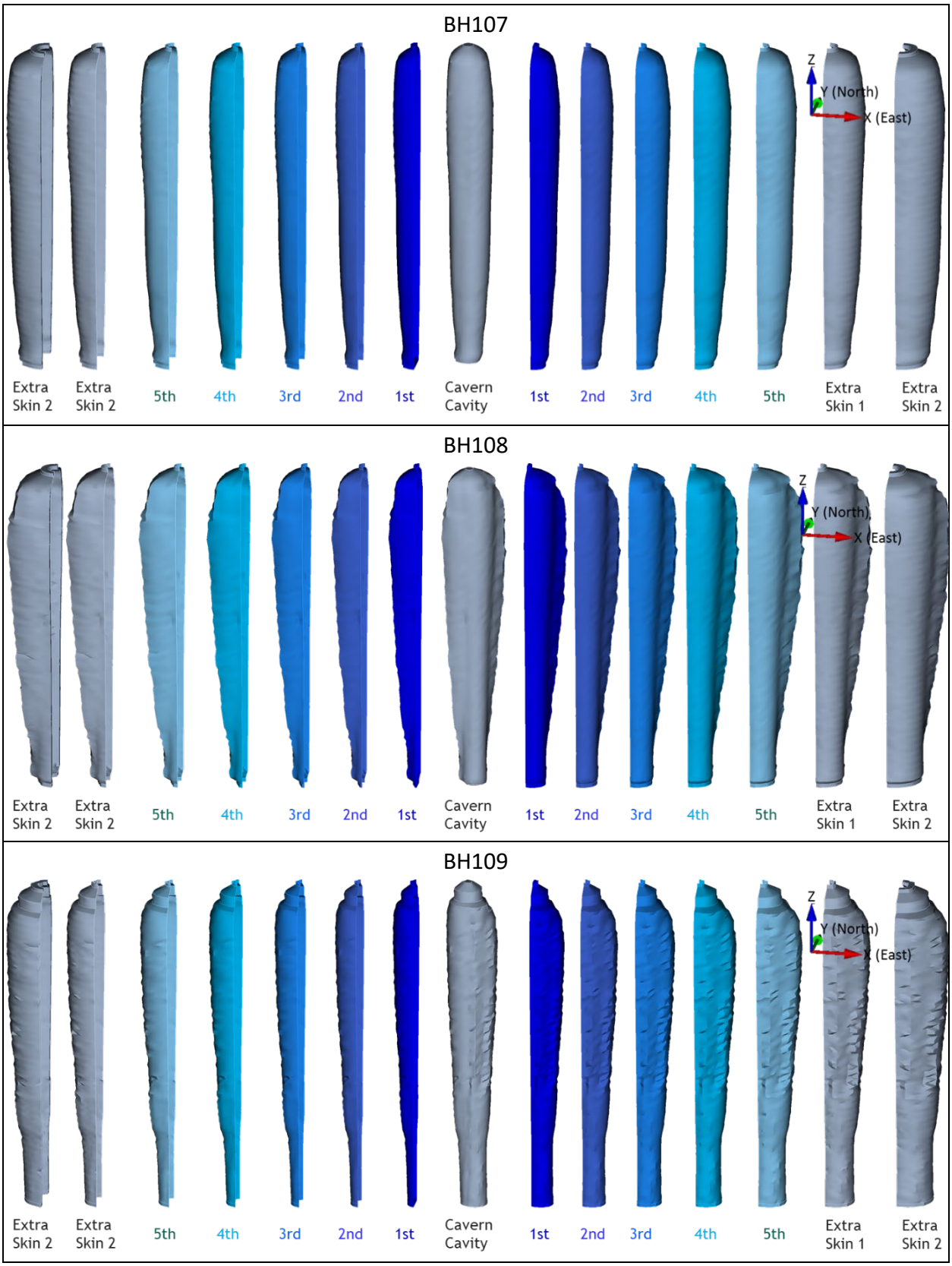
BH107
Z
Y (North)
X (East)
Extra Skin 2
Extra Skin 2
5th
4th
3rd
2nd
1st
Cavern Cavity
1st
2nd
3rd
4th
5th
Extra Skin 1
Extra Skin 2
BH108
Z
Y (North)
X (East)
Extra Skin 2
Extra Skin 2
5th
4th
3rd
2nd
1st
Cavern Cavity
1st
2nd
3rd
4th
5th
Extra Skin 1
Extra Skin 2
BH109
Z
Y (North)
X (East)
Extra Skin 2
Extra Skin 2
5th
4th
3rd
2nd
1st
Cavern Cavity
1st
2nd
3rd
4th
5th
Extra Skin 1
Extra Skin 2

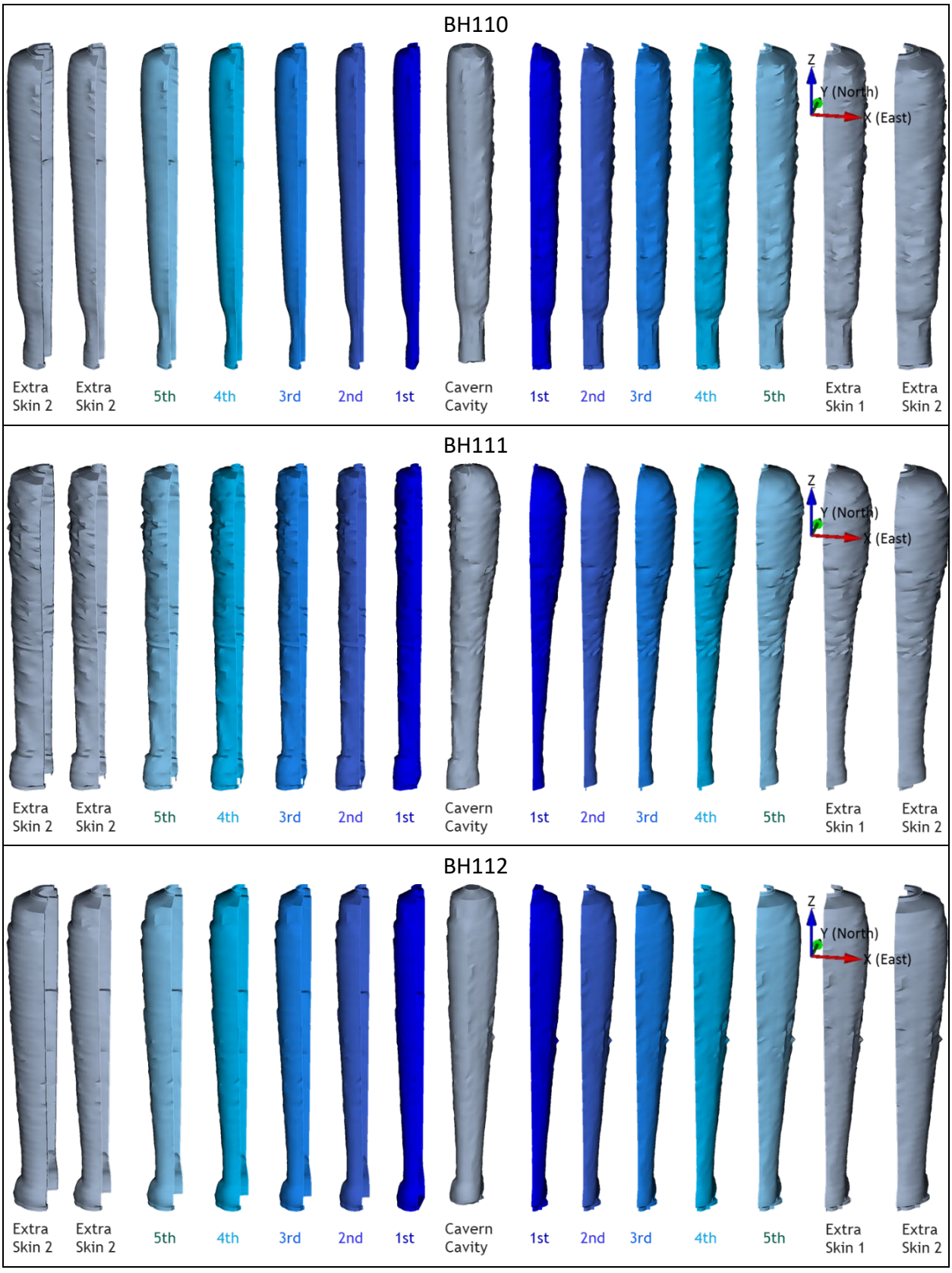
BH110
Z
Y (North)
X (East)
Extra Skin 2
Extra Skin 2
5th
4th
3rd
2nd
1st
Cavern Cavity
1st
2nd
3rd
4th
5th
Extra Skin 1
Extra Skin 2
BH111
Z
Y (North)
X (East)
Extra Skin 2
Extra Skin 2
5th
4th
3rd
2nd
1st
Cavern Cavity
1st
2nd
3rd
4th
5th
Extra Skin 1
Extra Skin 2
BH112
Z
Y (North)
X (East)
Extra Skin 2
Extra Skin 2
5th
4th
3rd
2nd
1st
Cavern Cavity
1st
2nd
3rd
4th
5th
Extra Skin 1
Extra Skin 2

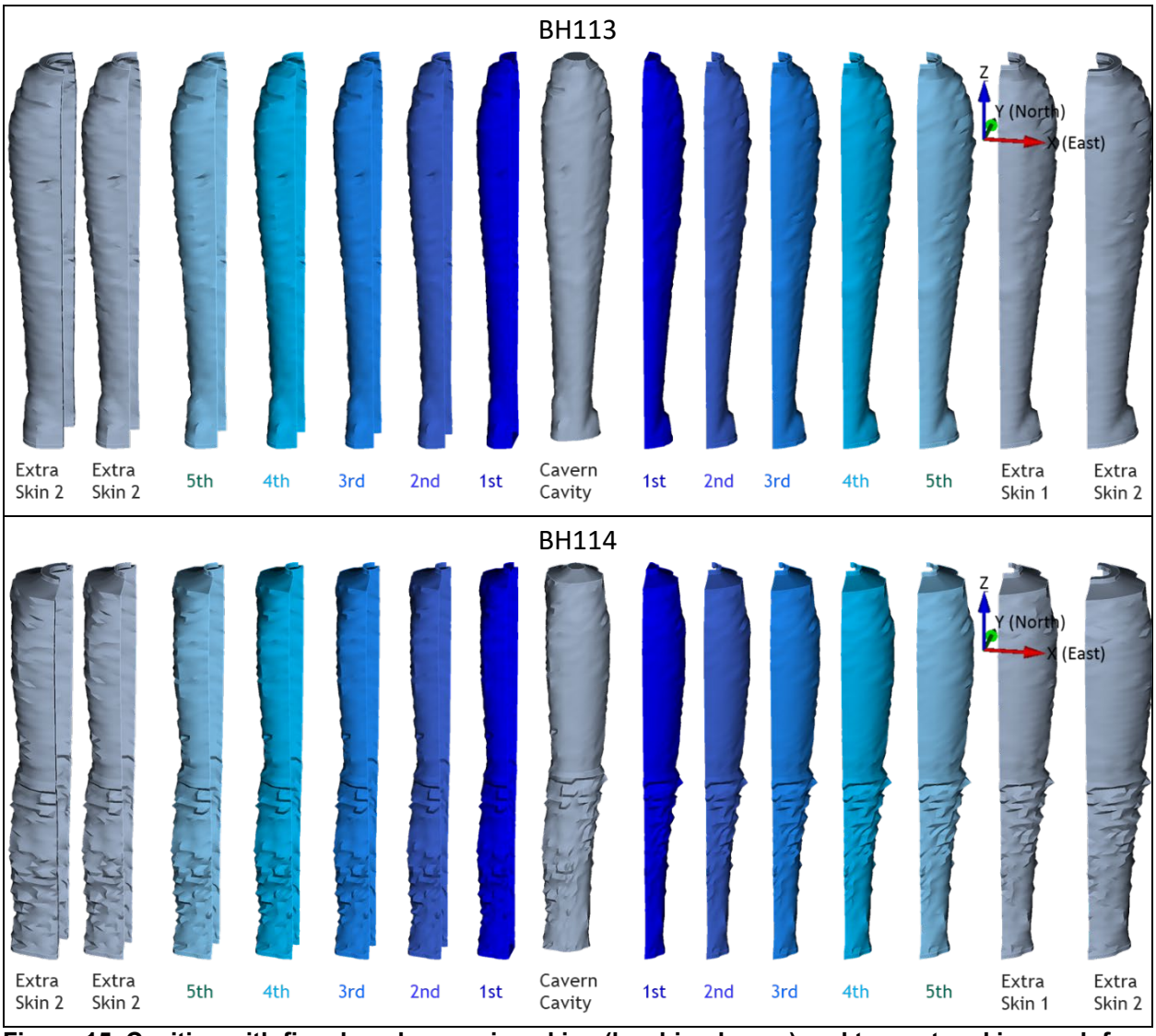

Figure 15 Cavities with five drawdown onion skins (leaching layers) and two extra skins each for Big Hill 14 SPR caverns

3.5. Entire Mesh

The BH-dome, caverns, caprock, interbed, interface, shear zone, and surrounding rock blocks are combined into the entire BH-model as shown Figure 16, which also shows an overview of the hexahedral finite element mesh of the stratigraphy and cavern field at the site. The mesh consists of 4,594,464 nodes and 4,566,900 elements with 344 element blocks, 3 node sets (on the boundaries of the entire mesh, to enforce zero normal displacement boundary conditions), and 84 side sets (on the interior surfaces of the caverns and skin layers, to enforce cavern pressure boundary conditions).

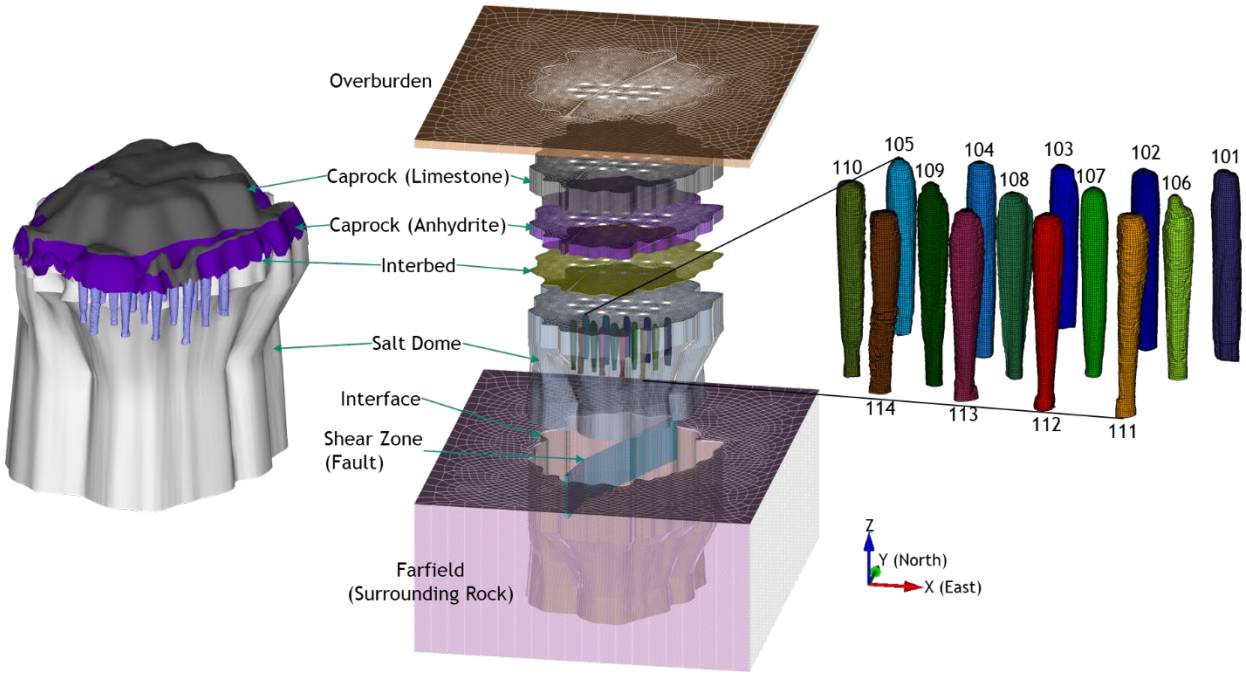

Figure 16 Images of Big Hill salt dome and caprock obtained from the seismic, sonar and borehole survey (left), an overview of the meshes of the stratigraphy (middle), and caverns (right). The cavern ID numbers are also shown.

This page left blank

4. MECHANICAL CONDITIONS

4.1. Assumptions

In any numerical simulation of physical processes it is frequently necessary to invoke a number of assumptions which render the analysis tractable. Analyses involving geologic materials are well known to be very challenging due to the extreme variability of rock quality (e.g. degree of fracturing) and the inability to fully characterize the in-situ response of the rock when subjected to events such as leaching and mining. While laboratory tests can be performed under controlled conditions to give insight into the stress-strain behavior, there are always questions about the degree of sample disturbance caused during the retrieval of the sample from the ground or even the relevance of the tests since the lab samples do not usually incorporate features such as discontinuities.

The finite element mesh developed for these analyses represents a region 12,400 ft by 14,600 ft in lateral dimensions and extending vertically from the ground surface down to the depth of 6000 ft. There are various assumptions for the computer simulations documented in this section:

- Use the simplified geometry of the planar layer for each interface between the lithologies,
- All materials are assumed to be isotropic and homogeneous,
- Use the material properties of anhydrite obtained from WIPP because the data of BH anhydrite are not known,
- Use the material properties of overburden for the interbed between the caprock and salt,
- Use the material properties of overburden for the fault from the surface to the salt top,
- A thin soft layer of elements is used for the interface block between the dome and surrounding rock,
- Use a thickness of 20 ft for the interbed between the caprock and salt, and
- Every lithology is bonded to each other.

4.2. Wellhead Pressure

The modeling simulates the cavern responses forward in time from the cavern's initial creation. The real wellhead histories of 14 caverns have been recorded from the dates as listed in Table 2. For the purposes of the present simulation, it is assumed that the initial leaches of the caverns started on the dates one year before the wellhead pressure recording started, i.e. they were leached to full size over a one-year period.

The peak wellhead pressures over 1000 psi in Figure 17 were created during mechanical integrity tests (MIT). To investigate well casing integrity for oil leakage, nitrogen gas is injected into the well. Nitrogen gas pressure at the wellhead causes pressure peaks because the nitrogen density is much less than oil density. The nitrogen gas pushes the oil-nitrogen interface (ONI) down towards the casing shoe, so the nitrogen replaces the oil between the wellhead and ONI. The density difference between oil and nitrogen can be offset by increased wellhead pressure, and then the resulting cavern pressure is only slightly different than normal oil wellhead pressure. The cavern volumetric closure rate due to salt creep depends on the difference between cavern internal and lithostatic pressures. The peak pressures due to MIT do not affect the cavern internal pressure much, so the peak

pressures can be ignored. The wellhead histories in Figure 17 were modified for use in the analysis as shown Figure 18. The real wellhead pressure plus oil/brine pressure gradient were applied on the inside boundary of each SPR cavern. Figure 15 shows the individual wellhead pressure histories used for 14 SPR caverns in this simulation.

Before initial leaching of a cavern starts, the model is given a stabilization period (1/1/1900 – 4/20/1989). To avoid the numerical shock, gravity is applied gradually into the mesh for ten seconds. After that, the model is allowed to consolidate with gravity for 89 years so that every element is stabilized numerically. The analysis simulates caverns that were leached to full size over a one-year period by means of gradually switching from salt to fresh water in the caverns. It is assumed that the SPR caverns were filled with petroleum and brine after the initial leaching. Creep is then permitted to occur over the entire simulation period (1/1/1900 – 09/18/2017).

Table 2. Dates of initial leach completion, wellhead pressure recording started, and assumed initial leach started

Cavern ID	Date of Initial Leach Completion	Date of Wellhead Pressure Recording Started	Assumed Date Initial Leach Started
BH101	09/17/1990	09/19/1990	09/19/1989
BH102	10/19/1990	10/20/1990	10/20/1989
BH103	11/27/1990	11/29/1990	11/29/1989
BH104	10/21/1990	10/21/1990	10/21/1989
BH105	05/13/1990	05/14/1990	05/14/1989
BH106	10/15/1990	10/17/1990	10/17/1989
BH107	04/23/1990	04/25/1990	04/25/1989
BH108	06/13/1990	06/14/1990	06/14/1989
BH109	07/23/1990	07/25/1990	07/25/1989
BH110	04/18/1990	04/20/1990	04/20/1989
BH111	07/14/1991	07/15/1991	07/15/1990
BH112	06/17/1991	06/19/1991	06/19/1990
BH113	04/30/1991	05/02/1991	05/02/1990
BH114	08/26/1991	08/29/1991	08/29/1990

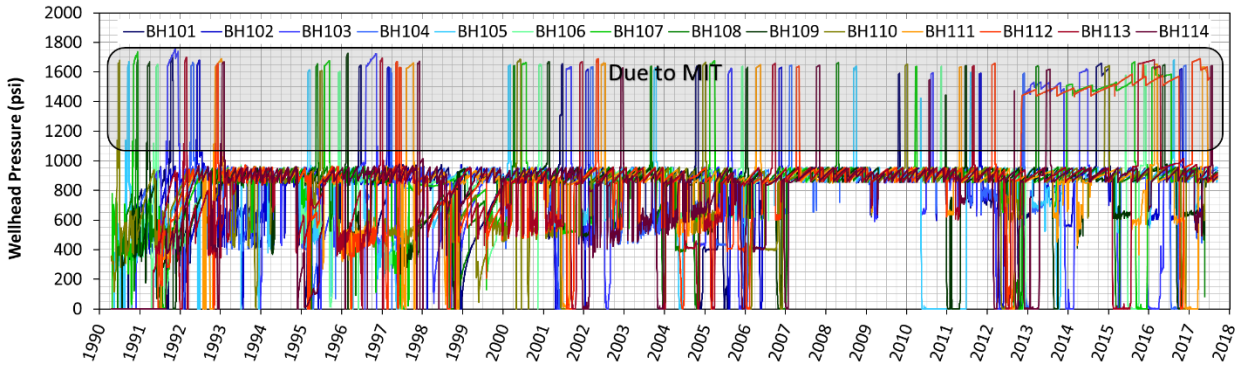

Figure 17 Wellhead pressure histories recorded from 14 Big Hill SPR caverns provided by the field office.

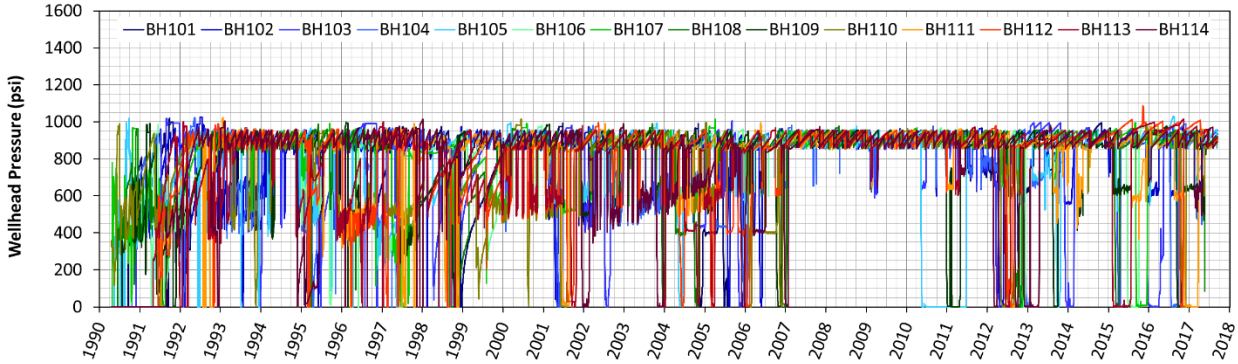

Figure 18 Modified wellhead pressure histories for the 14 Big Hill SPR caverns

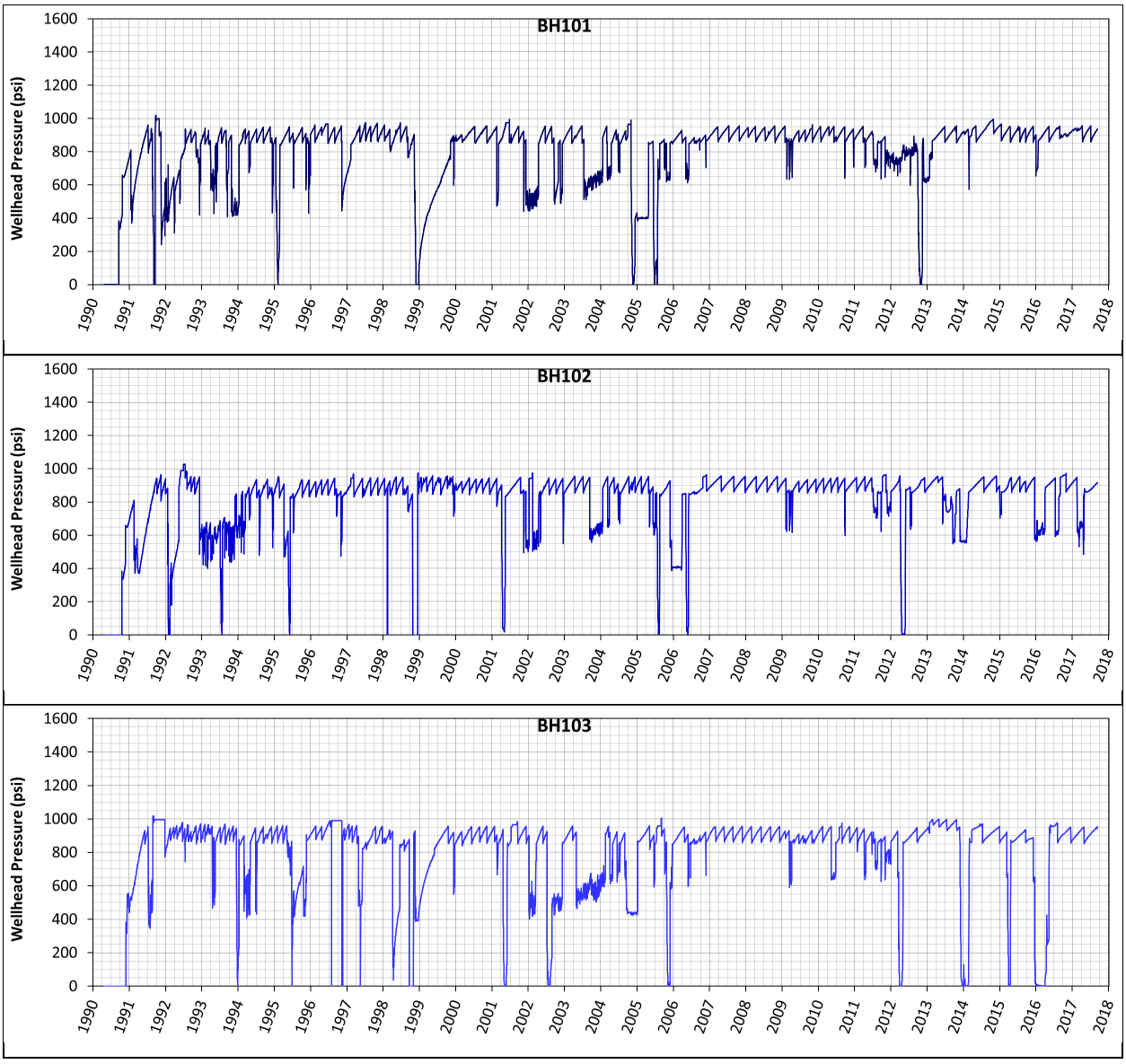

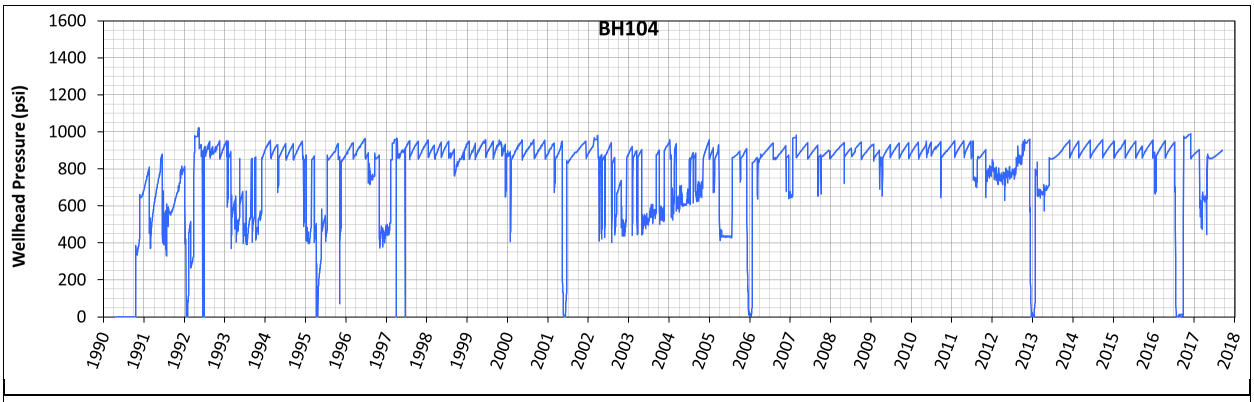
BH104
Wellhead Pressure (psi)
0
200
400
600
800
1000
1200
1400
1600
1990
1991
1992
1993
1994
1995
1996
1997
1998
1999
2000
2001
2002
2003
2004
2005
2006
2007
2008
2009
2010
2011
2012
2013
2014
2015
2016
2017
2018

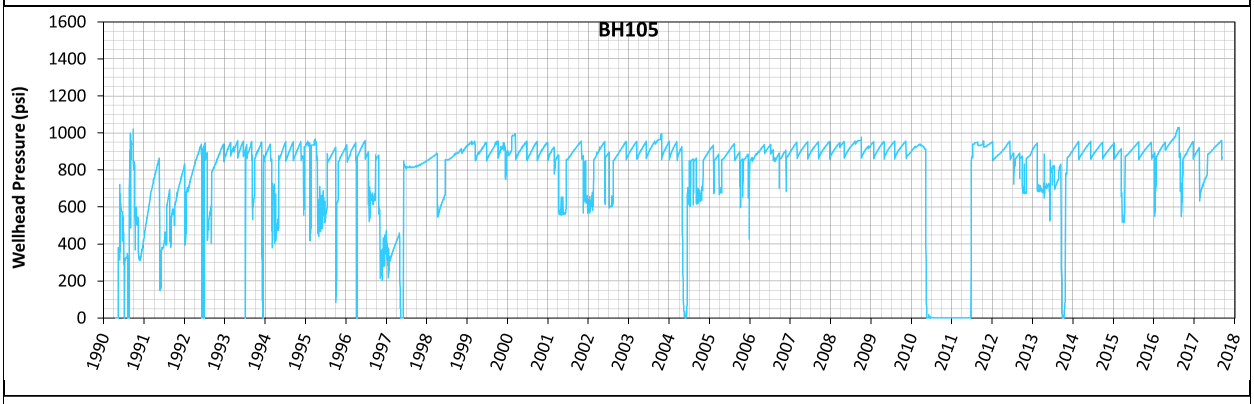
BH105
Wellhead Pressure (psi)
0
200
400
600
800
1000
1200
1400
1600
1990
1991
1992
1993
1994
1995
1996
1997
1998
1999
2000
2001
2002
2003
2004
2005
2006
2007
2008
2009
2010
2011
2012
2013
2014
2015
2016
2017
2018

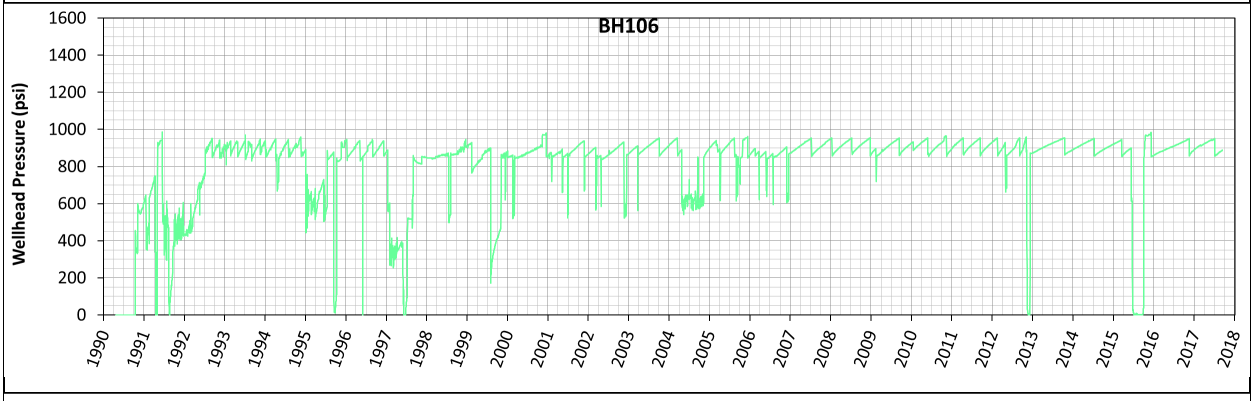
BH106
Wellhead Pressure (psi)
0
200
400
600
800
1000
1200
1400
1600
1990
1991
1992
1993
1994
1995
1996
1997
1998
1999
2000
2001
2002
2003
2004
2005
2006
2007
2008
2009
2010
2011
2012
2013
2014
2015
2016
2017
2018

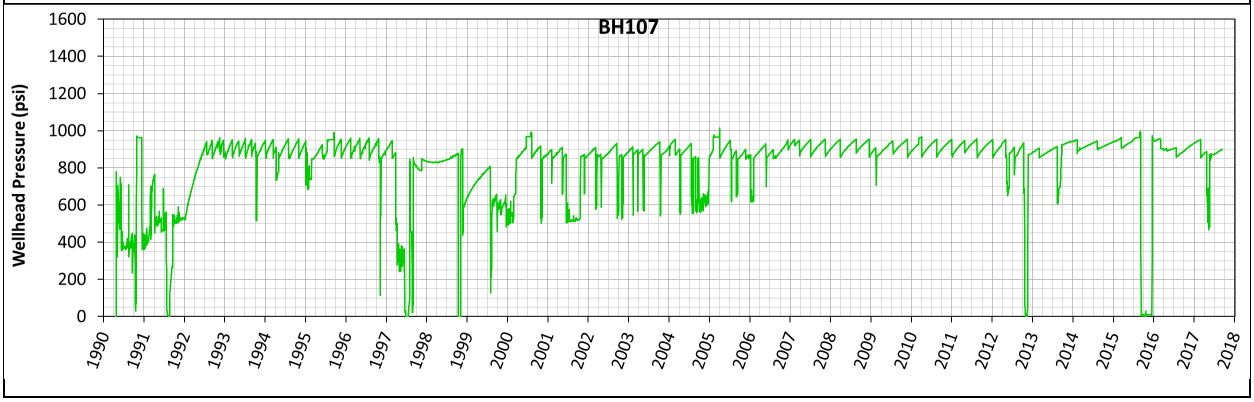
BH107
Wellhead Pressure (psi)
0
200
400
600
800
1000
1200
1400
1600
1990
1991
1992
1993
1994
1995
1996
1997
1998
1999
2000
2001
2002
2003
2004
2005
2006
2007
2008
2009
2010
2011
2012
2013
2014
2015
2016
2017
2018

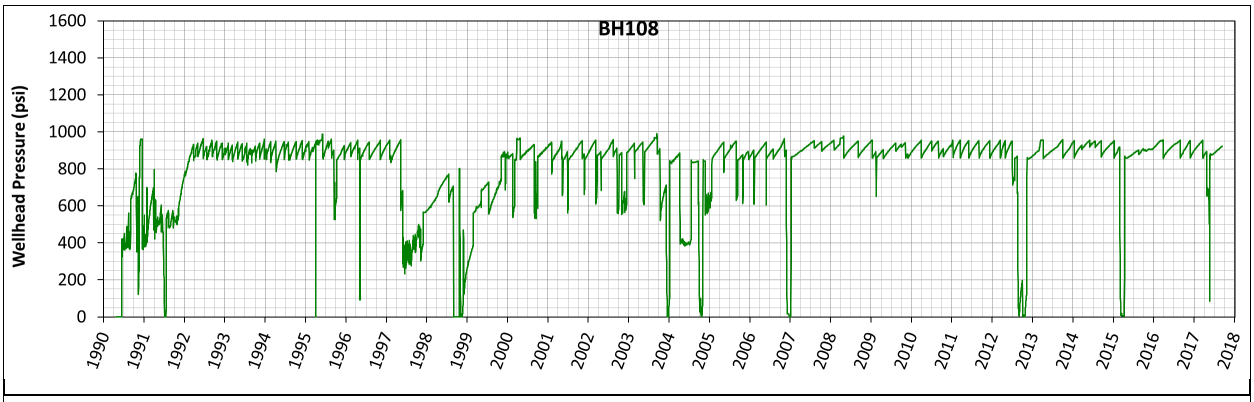
BH108
Wellhead Pressure (psi)
0
200
400
600
800
1000
1200
1400
1600
1990
1991
1992
1993
1994
1995
1996
1997
1998
1999
2000
2001
2002
2003
2004
2005
2006
2007
2008
2009
2010
2011
2012
2013
2014
2015
2016
2017
2018

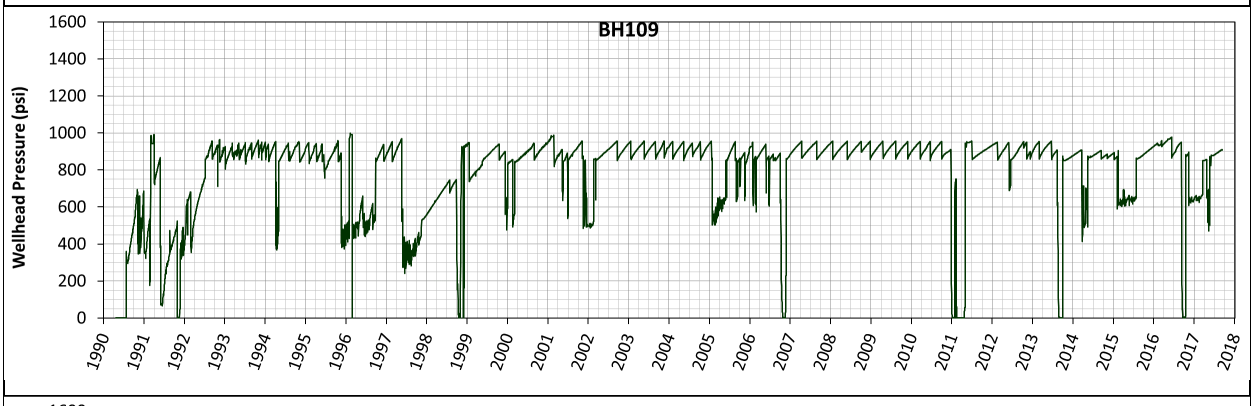
BH109
Wellhead Pressure (psi)
0
200
400
600
800
1000
1200
1400
1600
1990
1991
1992
1993
1994
1995
1996
1997
1998
1999
2000
2001
2002
2003
2004
2005
2006
2007
2008
2009
2010
2011
2012
2013
2014
2015
2016
2017
2018

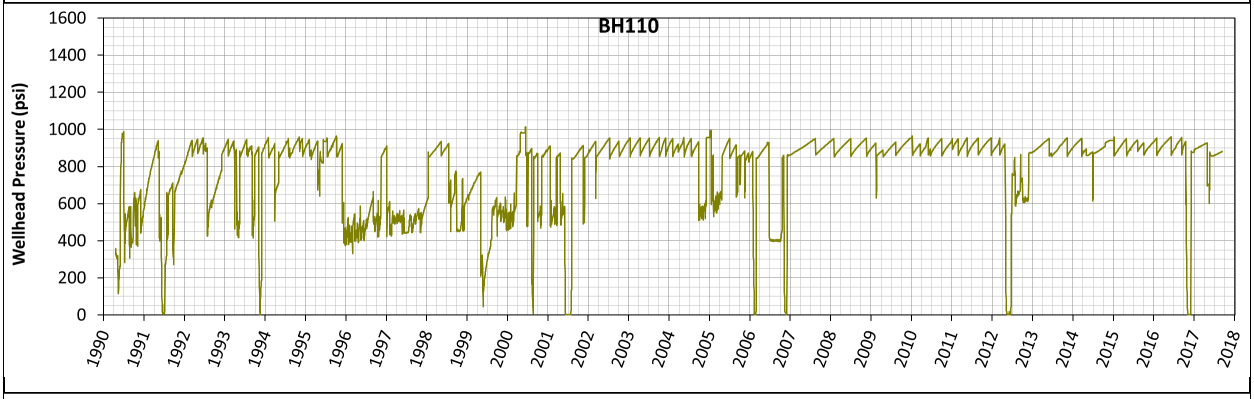
BH110
Wellhead Pressure (psi)
0
200
400
600
800
1000
1200
1400
1600
1990
1991
1992
1993
1994
1995
1996
1997
1998
1999
2000
2001
2002
2003
2004
2005
2006
2007
2008
2009
2010
2011
2012
2013
2014
2015
2016
2017
2018

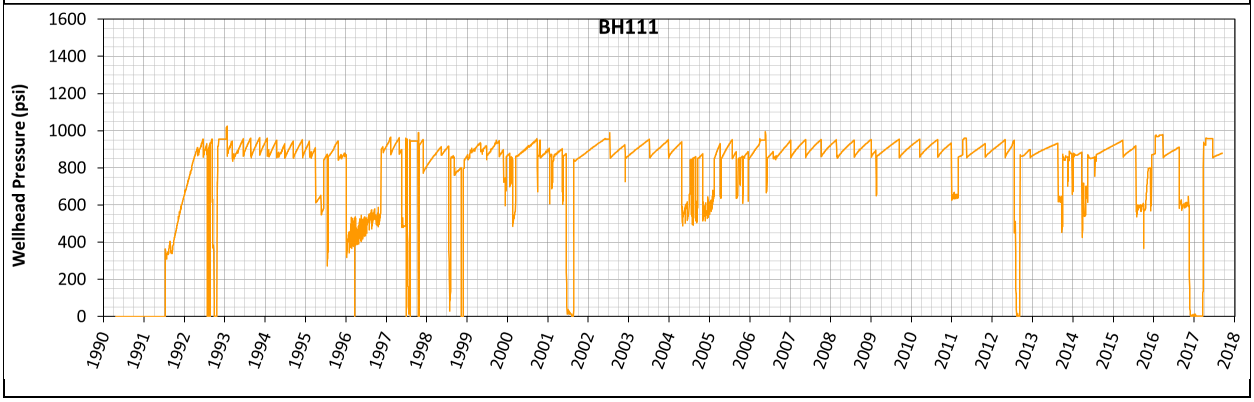
BH111
Wellhead Pressure (psi)
0
200
400
600
800
1000
1200
1400
1600
1990
1991
1992
1993
1994
1995
1996
1997
1998
1999
2000
2001
2002
2003
2004
2005
2006
2007
2008
2009
2010
2011
2012
2013
2014
2015
2016
2017
2018

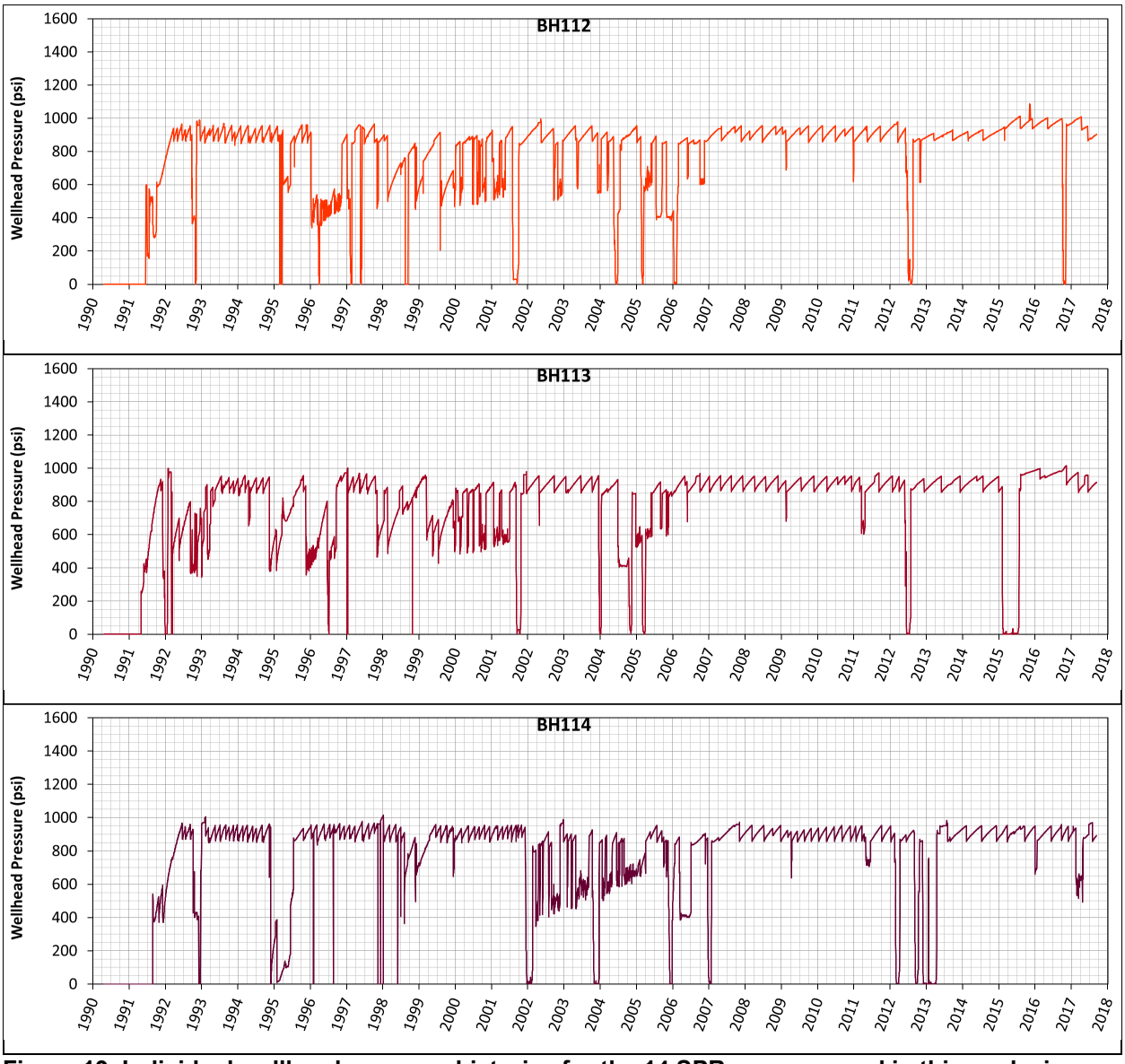

Figure 19 Individual wellhead pressure histories for the 14 SPR caverns used in this analysis

4.3. Oil-Brine Interface

Previous analyses [Park et al. 2005; Park and Ehgartner, 2012; Park 2014 a and b; Park et al. 2014] assumed that the SPR caverns were filled fully with oil. In actuality, however, the caverns were not always fully filled with oil. Brine fills the bottom of cavern and the portion changes with time depending on cavern operations. The difference between pressure gradients of oil (0.37 psi/ft of depth) and brine (0.52 psi/ft of depth) cannot be ignored. So, the amounts of oil and brine in a cavern over time needs to be considered. Park [2017] and Park et al. [2018] described the effect of the oil-brine interface (OBI) depth change. Figure 20 shows the OBI depth histories used in this analysis. The history data (4/20/1990 – 09/18/2017) were obtained from the field office.

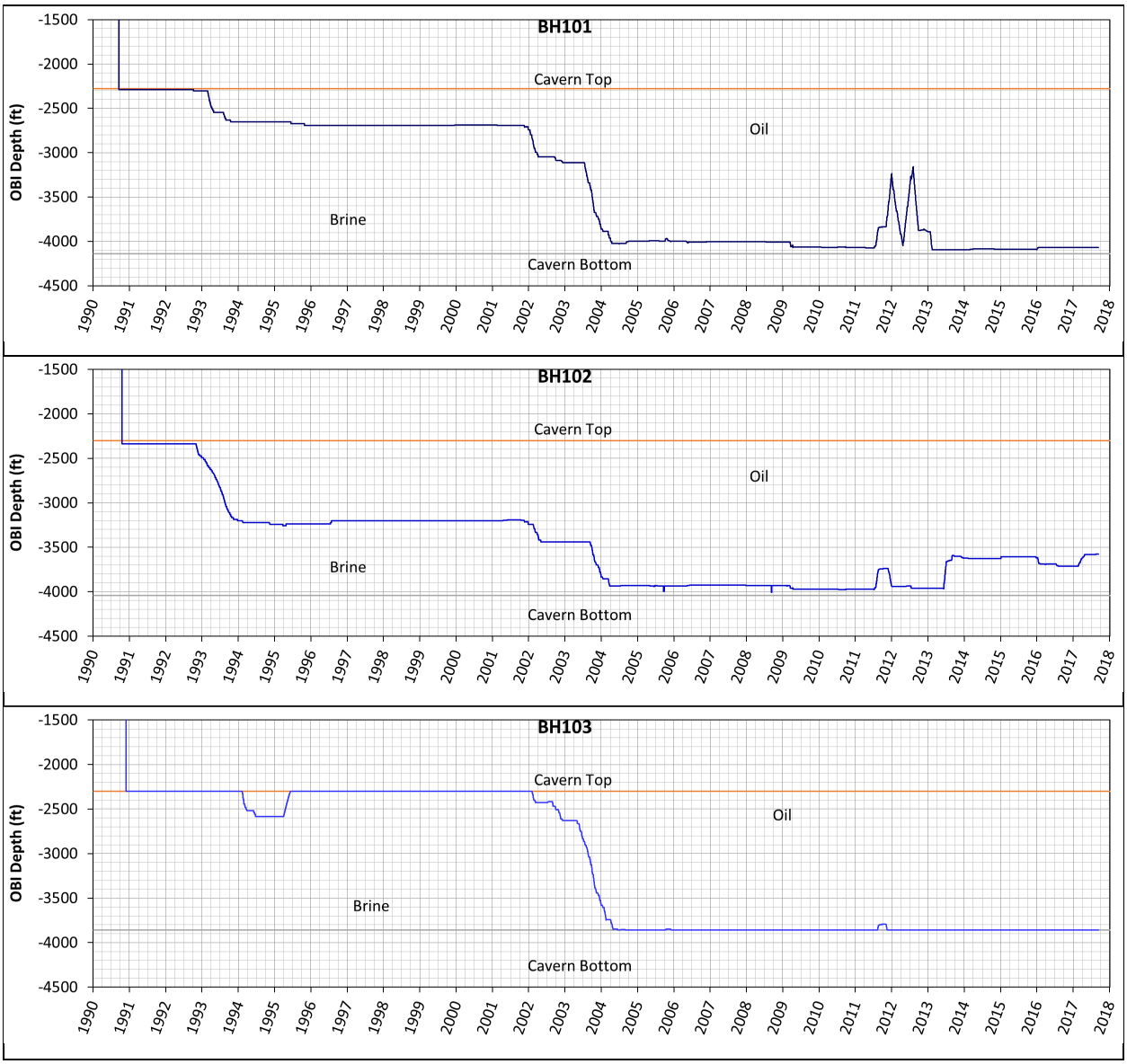

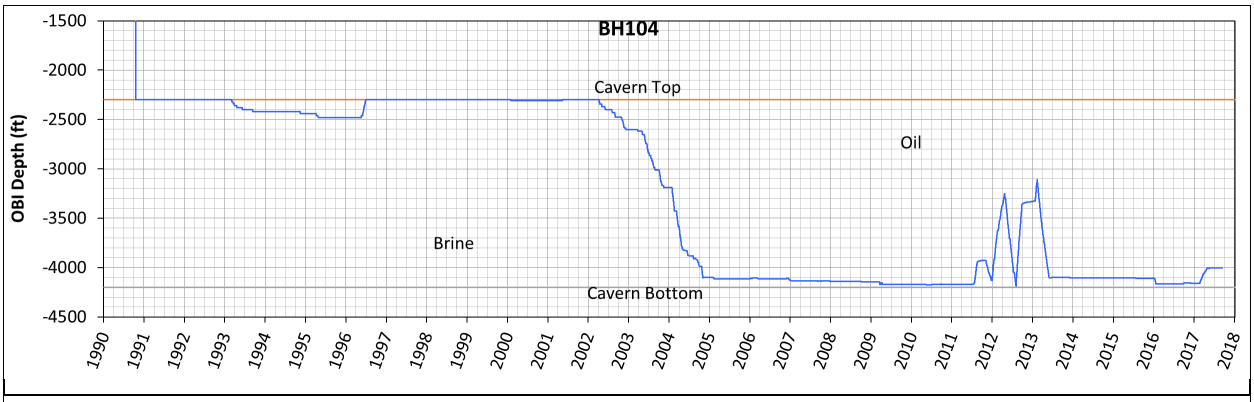
BH104
OBI Depth (ft)
-1500
-2000
-2500
-3000
-3500
-4000
-4500
Cavern Top
Oil
Brine
Cavern Bottom
1990
1991
1992
1993
1994
1995
1996
1997
1998
1999
2000
2001
2002
2003
2004
2005
2006
2007
2008
2009
2010
2011
2012
2013
2014
2015
2016
2017
2018

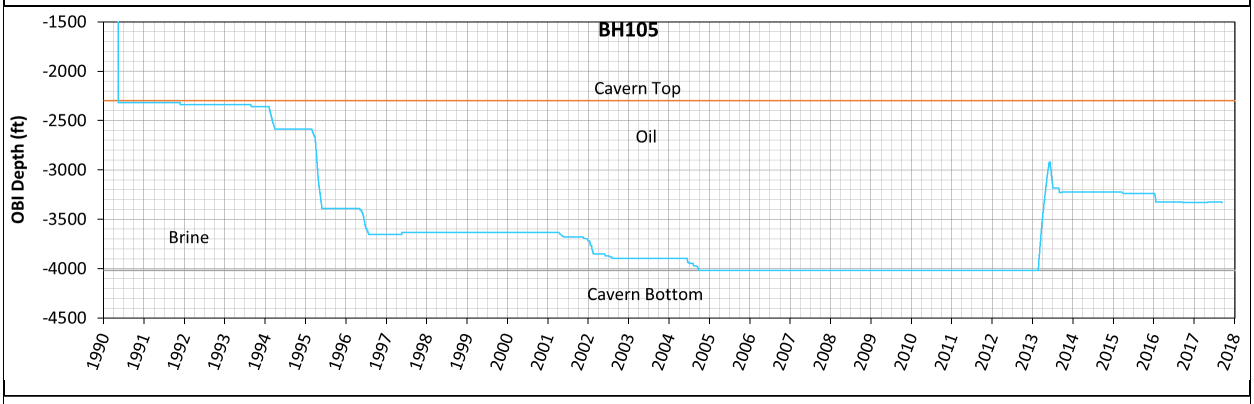
BH105
OBI Depth (ft)
-1500
-2000
-2500
-3000
-3500
-4000
-4500
Cavern Top
Oil
Brine
Cavern Bottom
1990
1991
1992
1993
1994
1995
1996
1997
1998
1999
2000
2001
2002
2003
2004
2005
2006
2007
2008
2009
2010
2011
2012
2013
2014
2015
2016
2017
2018

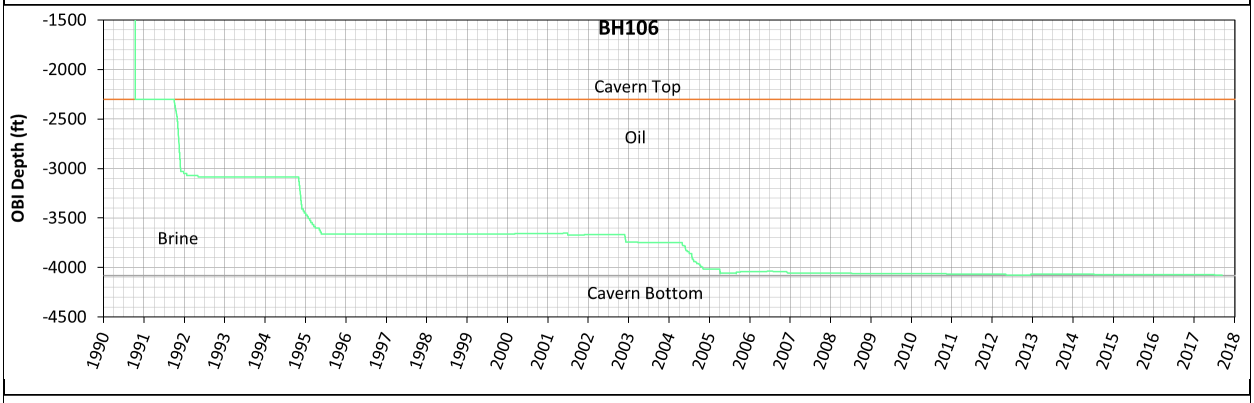
BH106
OBI Depth (ft)
-1500
-2000
-2500
-3000
-3500
-4000
-4500
Cavern Top
Oil
Brine
Cavern Bottom
1990
1991
1992
1993
1994
1995
1996
1997
1998
1999
2000
2001
2002
2003
2004
2005
2006
2007
2008
2009
2010
2011
2012
2013
2014
2015
2016
2017
2018

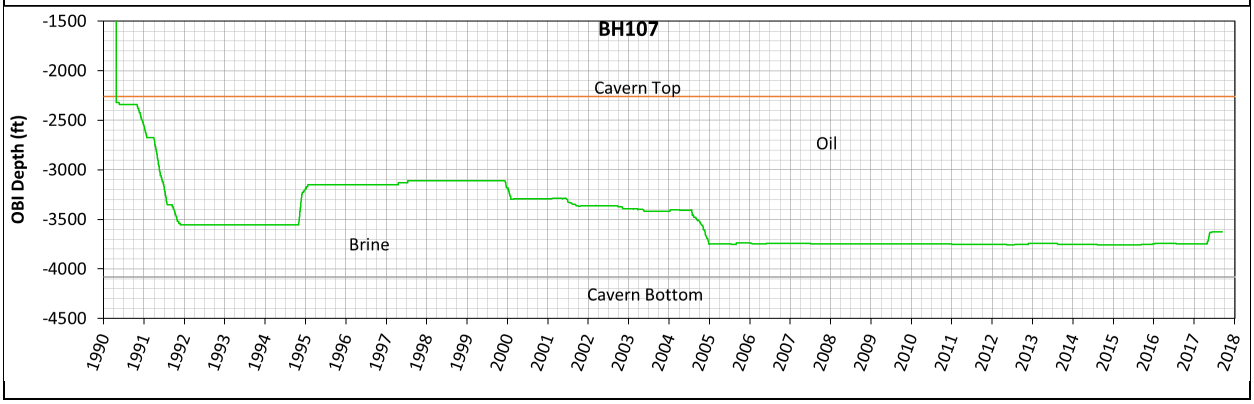
BH107
OBI Depth (ft)
-1500
-2000
-2500
-3000
-3500
-4000
-4500
Cavern Top
Oil
Brine
Cavern Bottom
1990
1991
1992
1993
1994
1995
1996
1997
1998
1999
2000
2001
2002
2003
2004
2005
2006
2007
2008
2009
2010
2011
2012
2013
2014
2015
2016
2017
2018

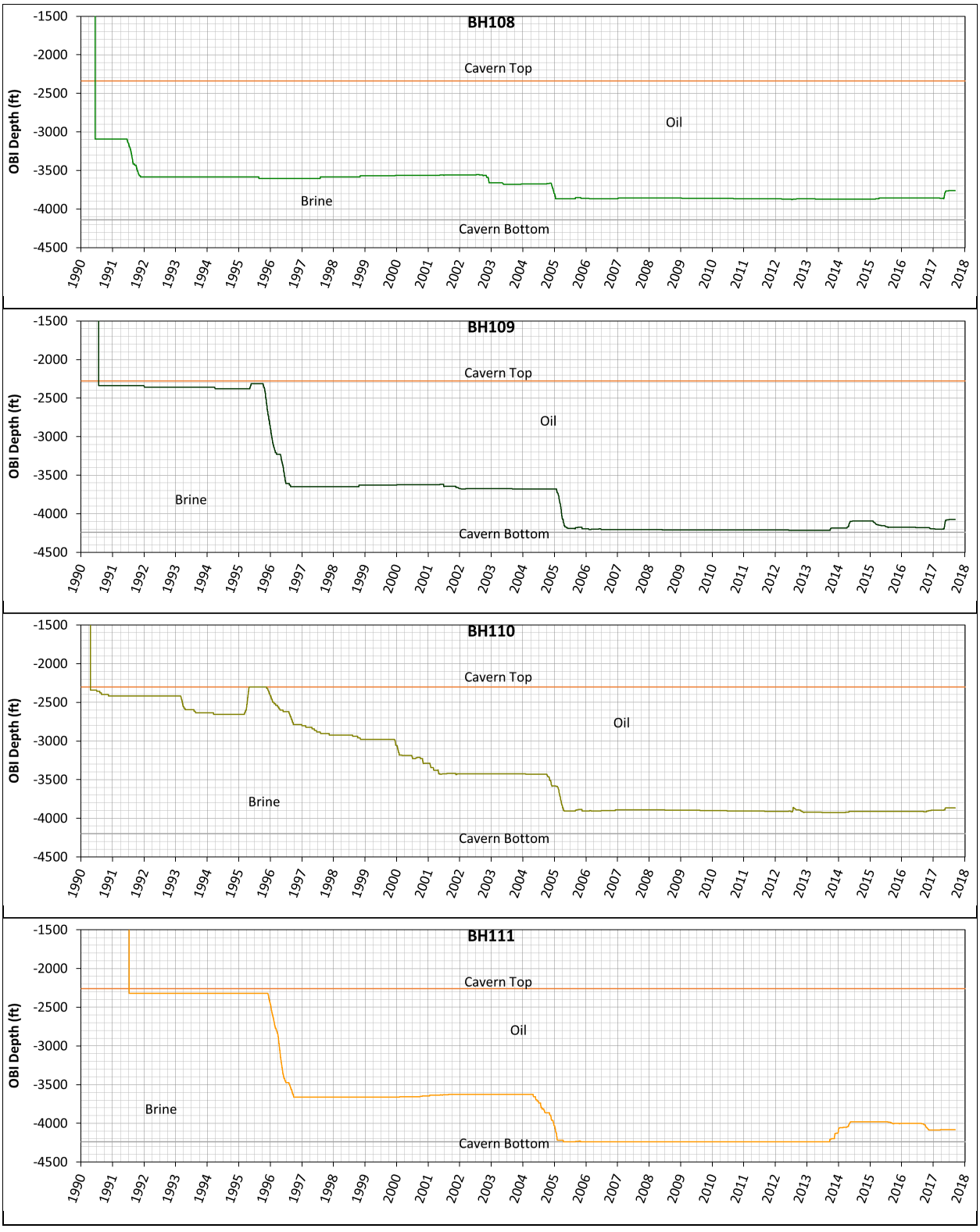
BH108
Cavern Top
Oil
Brine
Cavern Bottom
OBI Depth (ft)
-1500
-2000
-2500
-3000
-3500
-4000
-4500
1990
1991
1992
1993
1994
1995
1996
1997
1998
1999
2000
2001
2002
2003
2004
2005
2006
2007
2008
2009
2010
2011
2012
2013
2014
2015
2016
2017
2018
BH109
Cavern Top
Oil
Brine
Cavern Bottom
OBI Depth (ft)
BH110
Cavern Top
Oil
Brine
Cavern Bottom
OBI Depth (ft)
BH111
Cavern Top
Oil
Brine
Cavern Bottom
OBI Depth (ft)

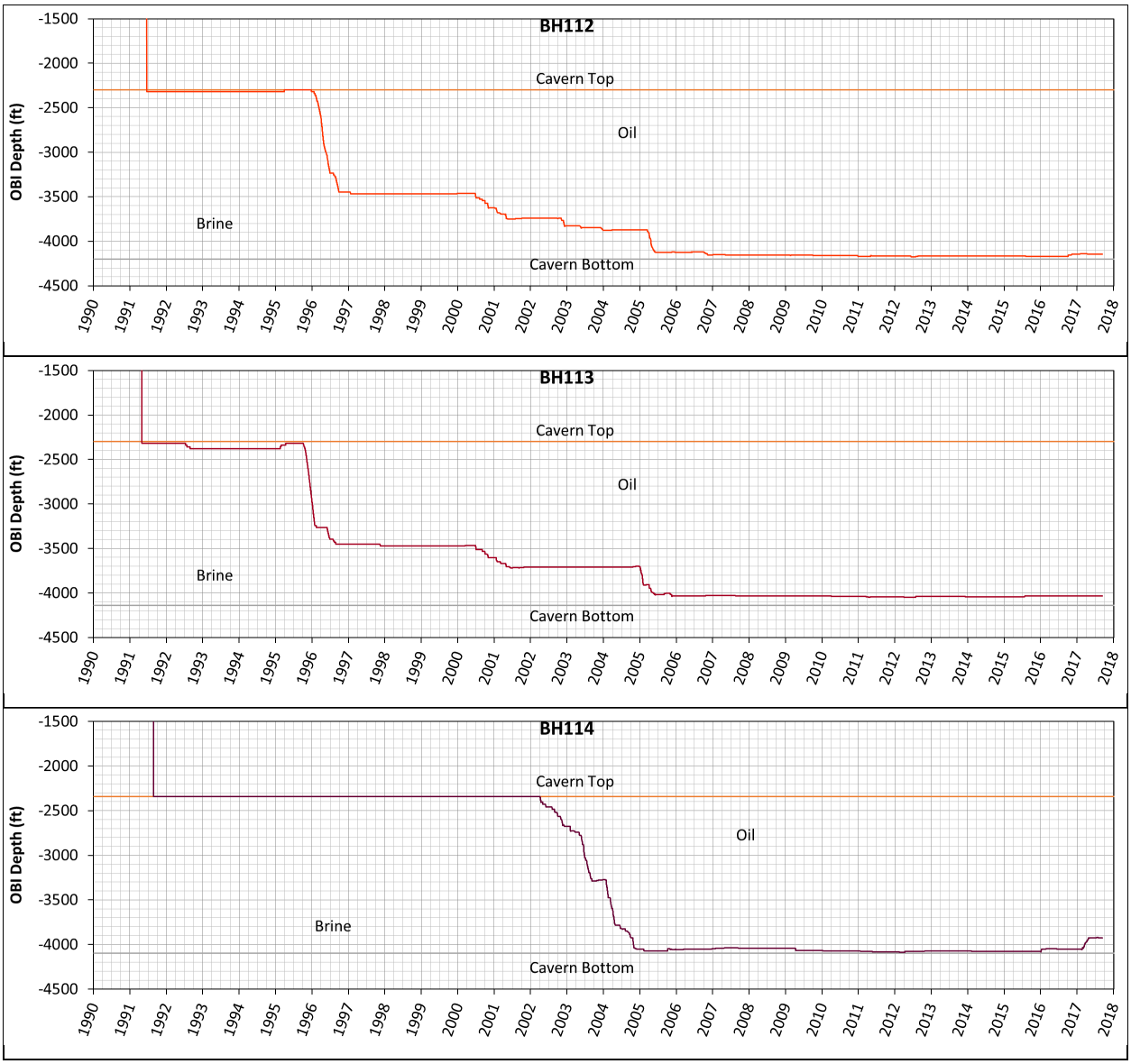

Figure 20 Individual oil-brine Interface depth histories to apply into the simulation for 14 Big Hill SPR caverns

4.4. Temperature

The finite element model includes a depth-dependent temperature gradient which starts at 76.7°F (24.8°C) at the surface and increases at the rate of 1.41°F/100 ft (2.57°C/100 m). The temperature profile is based on the average temperature data recorded in well logs from BH prior to leaching [Ballard and Ehgartner, 2000]. The temperature distribution is important because the creep response of salt is temperature dependent. Radial temperature gradients due to cavern cooling effects from the cavern contents are not considered in these calculations. Previous 2D cavern studies have shown the predicted cavern deformation to be insensitive to the developed radial thermal gradients [Hoffman, 1992].

4.5. Boundary Condition

Figure 21 shows the assembled mesh and the boundary conditions. The lengths of the confining boundaries are 14,600 ft in the N-S direction and 12,400 ft in the E-W direction. The boundary dimensions are determined by more than two times of the dome's range in each direction. The salt dome is modeled as being subject to a regional far-field stresses acting from an infinite distance away. The sizes of the caverns are horizontally much smaller than the dome. Therefore, the North and South sides of far-field boundary are fixed in Y-direction, and the East and West sides are fixed in X-direction. The bottom is fixed vertically. The top surface and four sides are vertically free. The acceleration of gravity used in the model is 9.81 m/s^2 (32.174 ft/s^2).

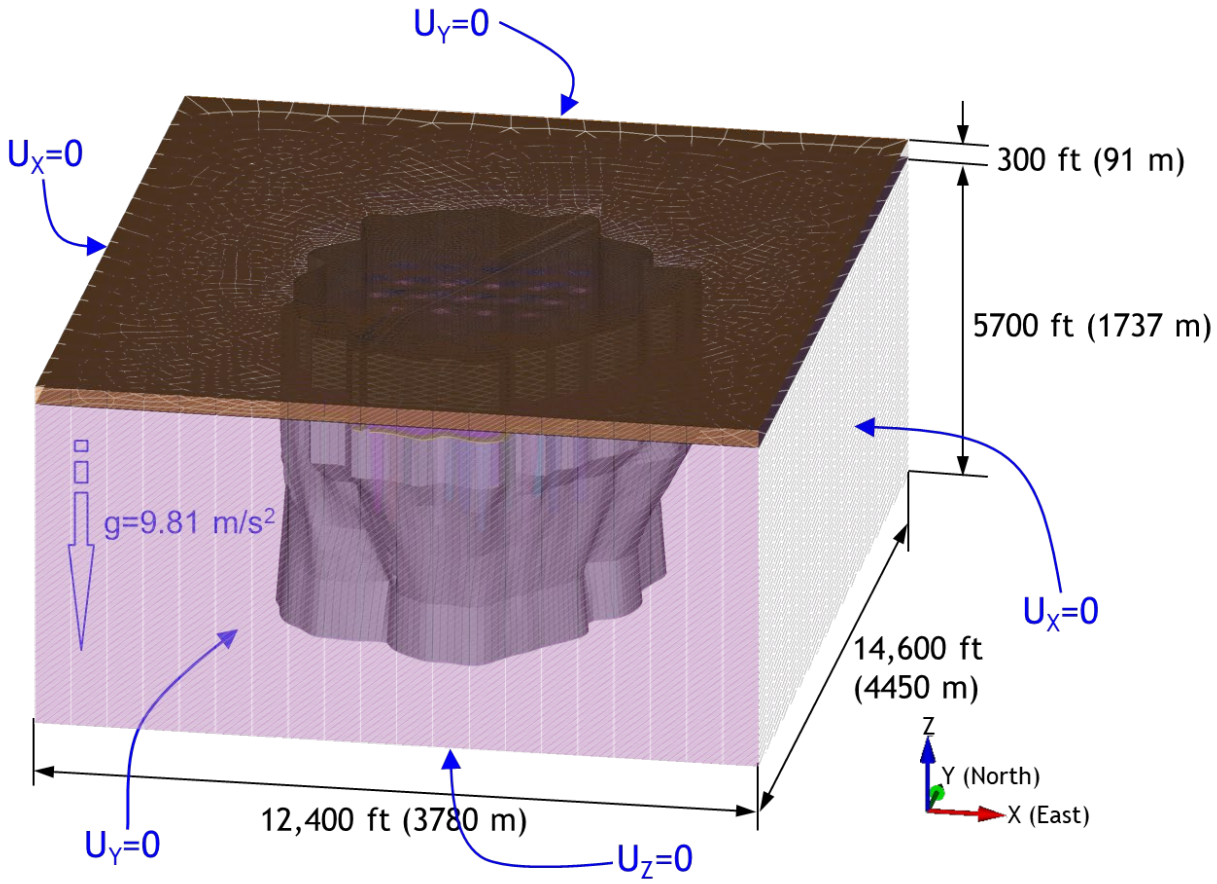

Figure 21 Boundary conditions of Big Hill Model

5. MATERIAL PROPERTIES

5.1. Salt

The previous BH analyses [Park et al. 2005; Park et al. 2006; Park and Ehgartner, 2012; Park 2014a,b; Park et al. 2014] were conducted using the power law creep (PLC) model, a simplified creep model that calculates the secondary steady-state creep mechanism, a subset of the more complete multi-mechanism deformation (M-D) model of salt creep. The PLC considers only the secondary creep rate (steady-state, long term); while M-D considers not only the secondary, but also the primary (initial stage, short term) and the tertiary (beyond steady-state) creep rates as shown Figure 22. The implementation of the power law creep model included the use of a reduced elastic modulus to simulate the transient response of the salt to pressure changes. The resulting simulations provided satisfactory predictions of long-term creep behavior, but not of transient response to pressure changes. The geological concerns issued in BH require more accurate numerical predictions. For a higher-resolution geomechanical simulation, the FE mesh capturing realistic geometries of the salt dome and caverns and M-D salt constitutive model are required. The M-D model proposed by Munson and Dawson [1979, 1982, 1984] and extended by Munson et al. [1989], has been implemented in ADAGIO to model the creep behavior of rock salt.

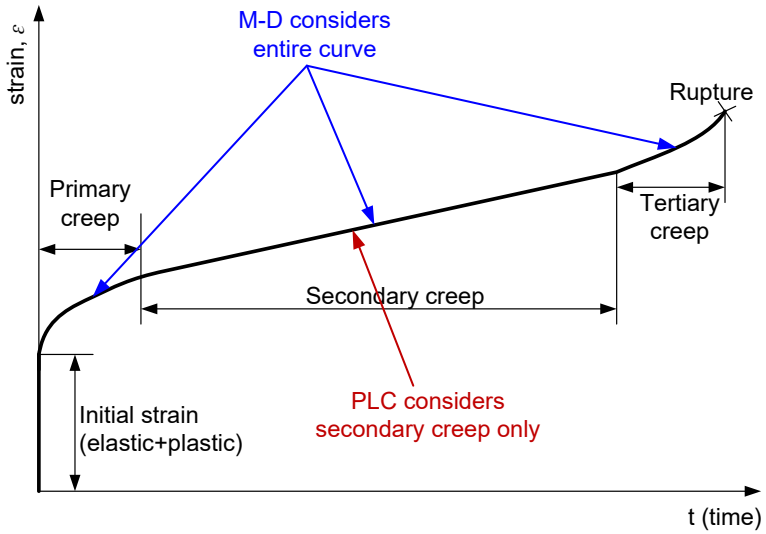

Figure 22 Comparison between M-D and Power Law Creep models

Creep is the time-dependent deformation of a material. Traditionally, a creep curve is thought to consist of three stages as shown in Figure 22. Experimental data obtained from a uniaxial stress laboratory creep tests, where the stress is held constant, typically have this form. In the first stage (primary), the creep rate decreases with time. In the second stage (secondary), the creep rate is constant (steady-state), and in the third stage (tertiary), the creep rate increases through progressive fracture formation and eventually terminates by failure of the specimen. Most uniaxial and triaxial compression tests do not reach the tertiary creep stage simply because of the amount of time required to get there. Empirically derived creep laws historically have described the shape of the creep curve through mathematical functions that consider the creep as the sum of transient and steady-state contributions. Transient creep is in general the response of the material to incremental

and decremental stress changes. This definition, thus, includes the transient of primary creep response to the initial loading in a standard creep test [Munson and Dawson, 1982].

Principles gained from our understanding of the constitutive behavior of WIPP salt will form the basis for the present analysis strategy. Not only do the constitutive equations of the M-D model define the necessary material parameters, but they also permit the formulation of rules of the analysis. In developing the constitutive description, we concern ourselves only with the temperature and stress range encountered in mining and storage cavern operations, typically low temperature and low to moderately high stresses. For these conditions, creep is envisioned as arising from the contributions of three appropriate micromechanical mechanisms as determined from salt deformation mechanism-map [Munson, 1979]. These mechanisms are (1) a dislocation climb controlled creep mechanism at high temperatures and low stresses, (2) an empirically specified, but undefined mechanism at low temperatures and low stresses, and (3) a dislocation slip controlled mechanism at high stresses [Munson, et al., 1989]. These mechanisms act in parallel, which means the individual steady-state creep rates can be summed over the three mechanisms to give the total steady-state creep rate, as follows [Munson, 1998]:

$$\dot{\varepsilon}_s = \sum_{i=1}^{3} \dot{\varepsilon}_{s_i} \tag{1}$$

The steady-state creep rates for the individual mechanisms, respectively, are given by:

$$\dot{\varepsilon}_{s_1} = A_1 e^{-\frac{Q_1}{RT}} \left[\frac{\sigma}{\mu(1-\omega)}\right]^{n_1} \tag{2}$$

$$\dot{\varepsilon}_{s_2} = A_2 e^{-\frac{Q_2}{RT}} \left[\frac{\sigma}{\mu(1-\omega)}\right]^{n_2} \tag{3}$$

$$\dot{\varepsilon}_{s_3} = |H(\sigma-\sigma_0)| \left(B_1 e^{-\frac{Q_1}{RT}} + B_2 e^{-\frac{Q_2}{RT}}\right) \sinh\left[\frac{q\left(\frac{\sigma}{1-\omega} - \sigma_0\right)}{\mu}\right] \tag{4}$$

where the numerical subscripts refer to the appropriate mechanism, the A's and B's are structure factors, Q's are activation energies, R is the universal gas constant, T is the absolute temperature, μ is the shear modulus, q is the stress constant, σ_0 is a stress limit, and H is the Heaviside step function with argument $(\sigma - \sigma_0)$. It has been shown [Munson, et al., 1989] through multiaxial experiments that the proper equivalent stress measure is $\sigma = |\sigma_1 - \sigma_3|$.

The equivalent total strain rate is treated through a multiplier on the steady-state rate, as

$$\dot{\varepsilon}_{eq} = F\dot{\varepsilon}_s \tag{5}$$

where the multiplier involves three branches of the transient creep curve: work-hardening, steady-state, and recovery, respectively, as follows:

$$F = \begin{cases} e^{\Delta\left(\left(1-\frac{\zeta}{\varepsilon_t^*}\right)^2\right)}; & \zeta < \varepsilon_t^* \\ 1 \qquad\qquad\quad ; & \zeta = \varepsilon_t^* \\ e^{-\delta\left(\left(1-\frac{\zeta}{\varepsilon_t^*}\right)^2\right)}; & \zeta > \varepsilon_t^* \end{cases} \tag{6}$$

Here, ⊿ is the work-hardening parameter, δ is the recovery parameter, ζ is the state parameter, and ε_t^* is the transient strain limit. The state parameter ζ rate of change is given by

$$\dot{\zeta} = (F-1)\dot{\varepsilon}_s \tag{7}$$

The transient strain limit is defined by

$$\varepsilon_t^* = K_0 e^{cT}\left(\frac{\sigma}{\mu(1-\omega)}\right)^m \tag{8}$$

where K_0 and c are constants and m is a material constant.

The work-hardening, ⊿, and recovery, δ, parameters are described through linear functions, as follows:

$$\Delta = \alpha_w + \beta_w \log\frac{\sigma}{\mu(1-\omega)} \tag{9}$$

$$\delta = \alpha_r + \beta_r \log\frac{\sigma}{\mu(1-\omega)} \tag{10}$$

where the α's and β's are constants. Throughout these equations, although it is taken as zero for our purposes here, ω is the damage parameter.

Fundamentally, salt creep behavior has common micromechanical constitutive features regardless of the origin of the salt, all that differs is the exact value of the parameters. In particular, those critical parameters that primarily distinguish one salt material from another salt material are the steady-state responses as represented by the structure factors (A's and B's) and the transient strain rate limits (ε_t^*) as represented by K_0. By using the analysis criteria given above and the known behavior from the well-documented tests of clean WIPP salt as a baseline response, it may be possible on the one hand to construct reasonable steady-state responses for the domal salts. On the other hand, determination of the transient strain limit depends critically upon having the complete transient strain curves, i.e., complete conventional raw creep curves. In the absence of these curves, only uncertain estimates can be made for values for this parameter. Often, the only recourse in this case is to estimate the transient strain limit values based on the particle impurity level and the measured values from the clean and argillaceous WIPP salts. Remaining parameters are either unaffected by or insensitive to the specific salt material [Munson, 1998].

The database for Big Hill salt is developed using stress and temperature change tests from three specimens [Wawersik, 1985]. The specimens were prepared from recovered core from two deep boreholes at the site. These boreholes were to become solutioning wells, specifically Well 106B and Well 108B. Grain sizes were from medium to quite large, ranging from 3.7 mm (0.12 inch) to 51 mm (2.0 inch) with some cores having grains in excess of 100 mm (4.0 inch) in diameter. Although the salt purity was probably high, visual examination suggested finely distributed anhydrite crystals in the specimens from Well 106B. Magorian and Neal [1988] described the geology of the site in detail and reported insoluble contents based on density logs and x-ray analysis. The calculated median of insolubles from all logged holes is 1.7%, probably anhydrite. Anhydrite content was greatest in Wells 110A and 110B. Core samples indicated the occurrence of anhydrite bands parallel to the dome edges. It was believed that insoluble quantities decrease toward the edges of the dome [Munson, 1998]. Figure 23 shows the steady state creep rates for Big Hill domal salt.

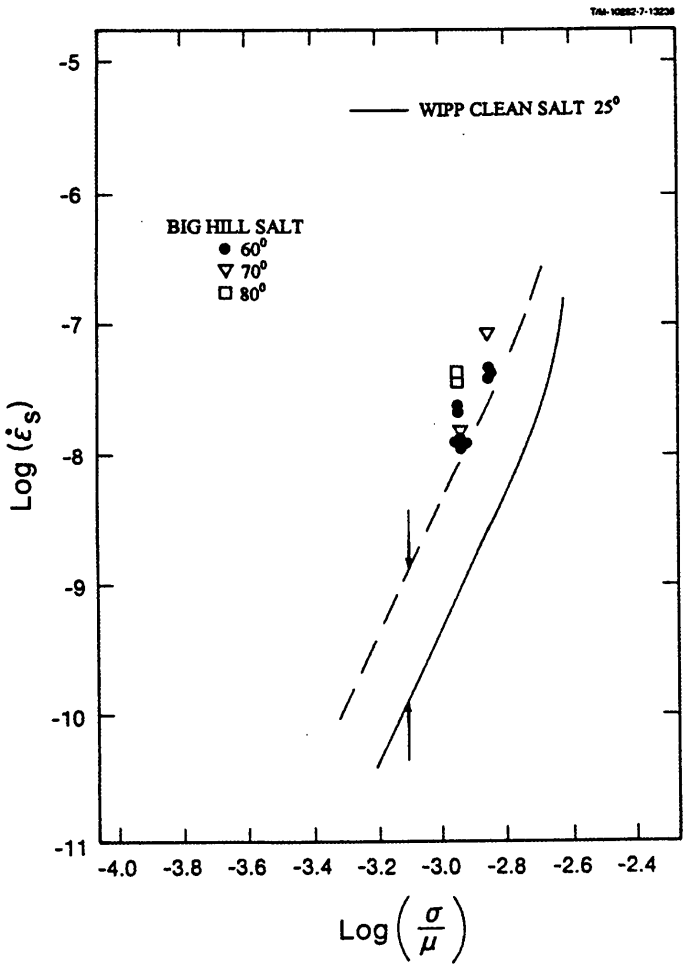

Figure 23 Steady state creep rates for Big Hill domal salt [Data from Wawersik, 1985]

Indirect substantiation of the effect of differences in the creep response of domal salt is found in the work of Ehgartner et al. [1995] on loss of volume of petroleum storage caverns of the SPR. These results are produced from a CAVEMAN simulation methodology based on the M-D creep equations. The methodology generates a set of "effective" fitting parameters for material, geometry, pressurization, and stress in the cavern setting as determined from cavern fluid loss histories and can be used to predict "effective" SPR cavern creep rates. These rates have been reported [Linn, 1997] from an ullage study. The effective creep rates in volume loss percentage per year (the same as a linear rate) are shown in Figure 24. Of the four facilities studied, Big Hill and West Hackberry show the highest creep volume loss rates; whereas, Bryan Mound and Bayou Choctaw show the lowest [Munson, 1998].

Because all of the creep tests were conducted at relatively low stress and low temperature, we can characterize the creep in terms of the structure factor of just one of the three mechanisms involved in salt creep. This is the undefined or empirical mechanism with the structure factor A_2. Values of the structure factor can be used to evaluate the relative creep "resistance" of the various domal salts compared to the WIPP clean salt creep baseline. Structure factor multiplication factor (*SMF*) from WIPP 25°C pure salt baseline is defined as $SMF = A_{2\ \text{Domal Salt}} / A_{2\ \text{WIPP Salt}}$. A_1, B_1, and B_2 of domal salt are multiplied those of WIPP salt by *SMF*. By applying ratios determined from the creep results,

we can establish some suggested M-D creep parameters. However, the limited database permits only structure factors to be determined; all other parameters are established on the basis of the clean WIPP salt database and the logical extension of the WIPP parameters, considering how material variation can affect the parameter. These results are given in Table 3 for clean WIPP salt and the Big Hill salt [Munson, 1998].

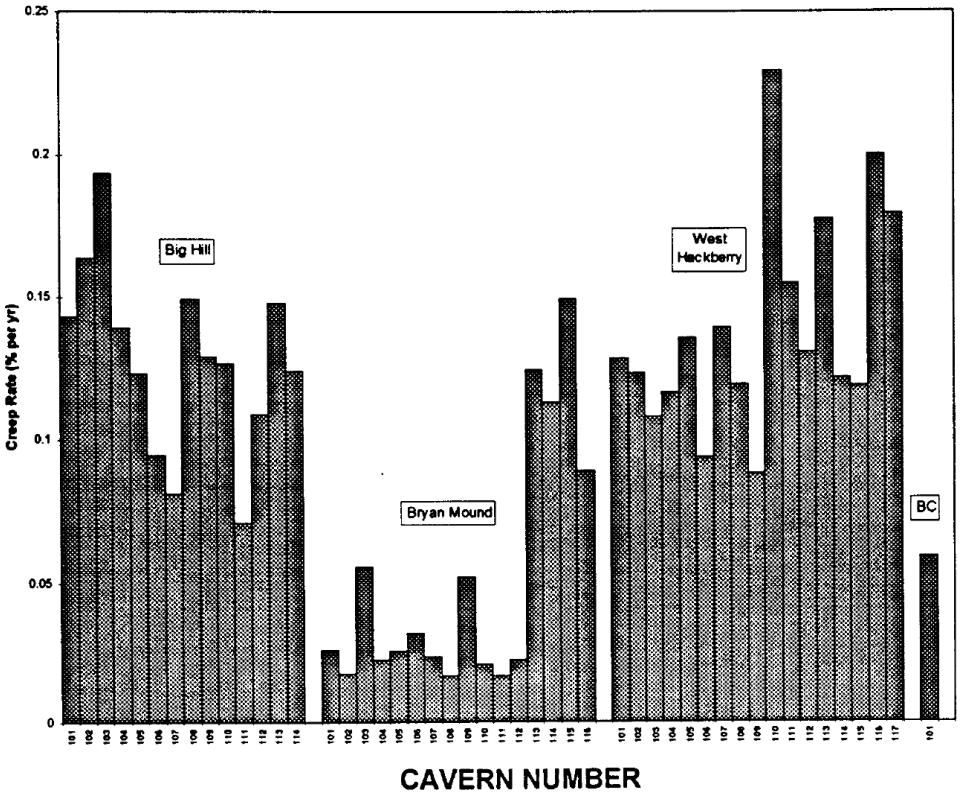

Figure 24 CAVEMAN calculated volume creep rates for SPR caverns [Linn, 1997]

Table 3 Suggested parameter values for the use of the M-D model for Big Hill salt [Munson, 1998]

Mechanism	Parameter	Symbol	Unit	WIPP Salt Baseline	BH Salt
Conventional	Density	ρ	lb/ft^3	**143.58 (2300 kg/m^3)**	143.58
Elasticity	Young's Modulus	E	psf	**647,447,400 (31.0 GPa)**	647,447,400
	Shear Modulus	μ	psf	**258,978,960 (12.4 GPa)**	258,978,960
	Poisson's Ratio	ν	-	**0.25**	0.25
Dislocation climb controlled creep mechanism at high temperatures and low stresses (Eq. 2)	Structure factor	A_1	1/s	**8.386×10^{22}**	9.815×10^{22}
	Activation energy	Q_1	cal/mol	**25,000**	25,000
	Stress exponent	n_1	-	**5.5**	5.5
Empirically specified but undefined mechanism at low temperatures and low stresses (Eq. 3)	Structure factor	A_2	1/s	**9.672×10^{12}**	**11.32×10^{12}**
	Activation energy	Q_2	cal/mol	**10000**	10000
	Stress exponent	n_2	-	**5.0**	**5.0**
Dislocation slip controlled mechanism at high stresses (Eq. 4)	Structure factor	B_1	1/s	**6,086,000**	7,122,986
	Structure factor	B_2	1/s	**0.03034**	0.03551
	Stress limit	σ_0	psf	**429,613 (20.57 MPa)**	429613
	Stress constant	q	-	**5335**	5335
Transient strain (Eq. 8)	Material constant	m	-	**3.0**	3.0
	Constant	K_0	-	**627500**	(627500)
	Constant	c	1/K	**0.009198**	0.009198
Work-hardening and recovery (Eq. 9&10)	Constant	α	-	**-17.37**	-17.37
	Constant	β	-	**-7.738**	-7.738
	Recovery	δ	-	**0.58**	0.58
	Damage	ω	-	**0.0**	0.0
Structure factor multiplication factor from WIPP 25°C salt		*SMF*	-	-	1.170*

Note:
Bold numbers are determined from creep data for that specific salt material.
Underlined values are theoretical micro-mechanism constants and are the same as WIPP clean salt values.
The K_0 value in parentheses is assumed.
All other values are assumed to be the same as WIPP salt values or adjusted from WIPP salt values in proportion to the A_2 value obtained experimentally for Big Hill salt.
Because the Multi-mechanism Deformation (M-D) model is used, the equations given in this report require a zero value for ω
* $SMF = A_{2\,\text{BH Salt}} / A_{2\,\text{WIPP Salt}}$, A_1, B_1, and B_2 of BH salt are multiplied those of WIPP salt by *SMF*

5.2. Lithologies Encompassing Salt

The surface overburden layer, which is mostly comprised of sandy soil, is modeled as exhibiting linear elastic material behavior. The layer is considered isotropic and homogeneous, and has no assumed failure criteria. The upper caprock layer, consisting of gypsum and limestone, is also assumed to be linear elastic, homogeneous, and isotropic. The rock surrounding the salt dome is assumed to be isotropic, homogeneous, linear elastic sandstone as well.

The anhydrite in the lower caprock layer is expected to experience inelastic material behavior. The anhydrite layer is considered isotropic and elastic until yield occurs [Butcher, 1997]. Once the yield stress is reached, plastic strain begins to accumulate. Yield is assumed to be governed by the Drucker-Prager (D-P) criterion:

$$\sqrt{J_2} = C - aI_1 \tag{11}$$

where $I_1 = \sigma_1 + \sigma_2 + \sigma_3 = 3\sigma_m$ is the first invariant of the stress tensor and

$\sqrt{J_2} = \sqrt{\frac{(\sigma_1 - \sigma_2)^2 + (\sigma_2 - \sigma_3)^2 + (\sigma_3 - \sigma_1)^2}{6}}$ is the square root of the second invariant of the deviatoric stress tensor; σ_1, σ_2, and σ_3 are the maximum, intermediate, and minimum principal stresses, respectively; σ_m is the mean stress; and C and a are D-P constants.

The material properties of the BH anhydrite are not known. Therefore, the behavior of the BH anhydrite is assumed to be the same as the Waste Isolation Pilot Plant (WIPP) anhydrite. A non-associative flow rule is used to determine the plastic strain components. A soils and foams model is used for the lower caprock. The input parameters, A_0 and A_1, are derived from the elastic properties and the D-P constants, C and a [Park et al., 2005].

The material properties for the lithologies overlying and surrounding the BH salt dome used as input data for the SNL-developed 3D solid mechanics codes used in the present analyses, ADAGIO, are listed in Table 4.

Table 4. Material properties of lithologies around salt dome used in the analyses.

		Unit	Overburden (Sandy soil)	Caprock 1 (Limestone and gypsum)	Caprock 2 (Anhydrite)	Surrounding Rock (Sandstone)
Young's modulus (E)		psf	2,088,543 (0.1 GPa)	438,594,119 (21 GPa)	1,568,496,111 (75.1 GPa)	1,461,980,396 (70 GPa)
Density (ρ)		lb/ft³	116.99 (1874 kg/m³)	156.07 (2500 kg/m³)	143.58 (2300 kg/m³)	156.07 (2500 kg/m³)
Poisson's ratio (ν)		-	0.33	0.29	0.35	0.33
Drucker-Prager constants	C	psf	N/A	N/A	28,195 (1.35 MPa)	N/A
	α	-	N/A	N/A	0.45	N/A
Bulk modulus (K)		psf	N/A	N/A	1,742,773,456 (83.44 GPa)	N/A
Shear modulus (μ)		psf	N/A	N/A	580,924,485 (27.82 GPa)	N/A
Soil and forms model constants	A_0	psf	N/A	N/A	48,836 (2.338 MPa)	N/A
	A_1	-	N/A	N/A	2.338	N/A
	A_2	-	N/A	N/A	0	N/A
References		-	Hoffman and Ehgartner, 1992	Hoffman and Ehgartner, 1992	Butcher, 1997	Lama and Vutukuri, 1978

5.3. Interbed, Fault, and Interface

The interbed, fault, and interface are pseudo materials which represent contact surfaces. ADAGIO has a contact surface algorithm for modeling contact and sliding behavior between two solid surfaces. However, this algorithm has a limitation on the number of elements in the model. The current model is over that limit. In place of a contact surface, a thin, soft layer of elements is used for the interbed between the caprock and salt top, and the fault between two the blocks lying on

both sides. The thin, soft element layer uses the overburden material properties and is assumed to behave mechanically like a contact surface with friction coefficient of 0.2 determined from the relative displacement between two lithologies. Thus, the overburden material properties (Table 5) are used for the interbed and fault blocks.

The interface between the dome and surrounding rock is a vertical layer, while the interbed is a horizontal layer. In this analysis, it is assumed that the interface behaves like a thin, soft element layer in a manner similar to the interbed, but the horizontal pressure applied on the dome surface has to be the same as it arises from the surrounding rock. Therefore, the density and Poisson's ratio of the surrounding rock are used for the pseudo material of the interface. To implement a soft element, 1% of the surrounding rock's elastic modulus is used for the interface. The mechanical properties used in the analysis are listed in Table 5.

Table 5 Material properties of the interbed, fault, and interface used in the analysis

	Unit	Interbed and fault	Interface
Young's modulus	psf	2,088,543 (0.1 GPa)	14,619,804 (0.7 GPa)
Density	lb/ft^3	116.99 (1874 kg/m^3)	156.07 (2500 kg/m^3)
Poisson's ratio	-	0.33	0.33

6. PARAMETER EFFECT

The structure factor, A_2, and transient strain limit factor, K_0, in the M-D constitutive model are used for the calibration. The A_2 value obtained experimentally from the BH salt as shown Figure 23 and K_0 value of WIPP salt are used for the baseline values. The volumetric closure rates calculated using the baseline values listed in Table 3 are shown in Figure 25 [Park, 2018]. The solid and dotted lines indicate the results from ADAGIO and CAVEMAN calculations, respectively. For all simulations, the calculated volumetric closures are much smaller than the CAVEMAN results. The magnitude of the sudden increases (called "jumps" hereafter) in cavern volumetric closure during workovers is a function of both A_1 and A_2, but also of the transient creep phenomenon which is governed by the factor K_0 in Eq. (8) [Sobolik, 2015]. To adjust the magnitude of A_2 and K_0, multiplication factors *A2F* and *K0F* are defined, respectively. The *A2F* and *K0F* values of the salt dome and salt drawdown skins surrounding each SPR cavern (see Figure 15) have been determined through a number of back fitting analyses.

The input parameter values in the ADAGIO input deck lists in Table 6. The values for BH salt in Table 3 are converted into the ADAGIO input format. To examine the effect of changing A_2 on cavern volumetric closure, the cavern volume decrease rates are calculated with several A_2 values while the other parameter values are not changed. The multiplier *A2Fs* with *K0F*=1 is applied to all the salt blocks such as the salt dome and drawdown skins. Figure 26 show the relationship between the slope and *A2F* when *K0F*=1.0. The values of slopes of the linear trendlines are calculated for *A2F*=1, 10, 20, 40, 60, 80, 100, 200, 500, and 1000. The cavern volumetric closure rates (slope) increase as the *A2Fs* increase until approximately *A2F*=80, and then continue to increase for BH103 and BH114 or decrease for the other 12 caverns as shown Figure 26 [Park, 2018]. This relationship between the slope and *A2F* is used a reference to calibrate the value of A_2 in this study.

In similar manner, the cavern volumetric closure rates are calculated with several K_0 values while other parameter values are not changed to examine the effect of K_0. Figure 27 show the relationship between the slope and *K0F* when *A2F*=100. The values of the linear trendline slopes are calculated for *K0F* = 1, 2, 4, 8, and 16. The slope (cavern volumetric closure rate) slightly increases/decreases when *K0F* increases. Changing the K_0 value does not affect the cavern volumetric closure rate much [Park, 2018].

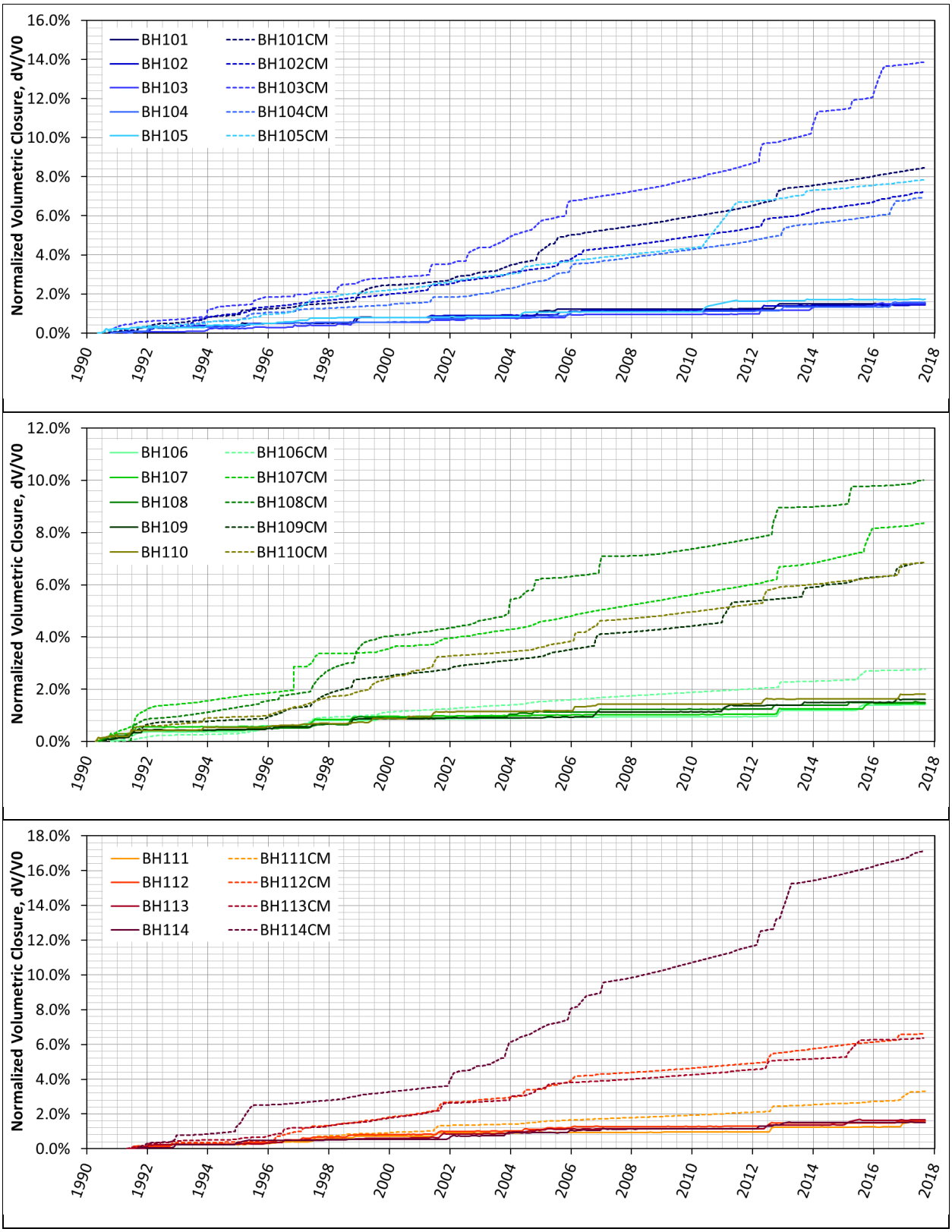

Figure 25 Volumetric closure normalized to initial volume calculated using the baseline parameter values and CAVEMAN predictions for BH101 through BH114 [Park, 2018]

Table 6 Parameter values used in ADAGIO input deck

Mechanism	Parameter	Symbol	Unit	Values in Input Deck
Conventional	Gravity	gr	ft/s^2	32.174
	Universal gas constant	R	cal/(mol·K)	1.986
	Temperature	T	K	Varies with depth*
	Density	ρ/gr	$lb \cdot s^2/ft^4$	4.4626** (2300 kg/m^3)
Elasticity	Young's modulus	E	psf	647,447,400 (31.0 GPa)
	Shear modulus	μ	psf	258,978,960 (12.4 GPa)
	Bulk modulus	K	psf	431,631,600 (20.7 GPa)
	Poisson's ratio	v	-	0.25
Dislocation climb controlled creep mechanism at high temperatures and low stresses (Eq. 2)	Structure factor	A_1	1/s	9.815×10^{22}
	Activation energy	Q_1/R	K	12,588.89‡
	Stress exponent	n_1	-	5.5
Empirically specified but undefined mechanism at low temperatures and low stresses (Eq. 3)	Structure factor	A_2	1/s	***A2F***†×11.32×10^{12}
	Activation energy	Q_2/R	K	5035.55‡
	Stress exponent	n_2	-	5.0
Dislocation slip controlled mechanism at high stresses (Eq. 4)	Structure factor	B_1	1/s	7,122,985
	Structure factor	B_2	1/s	0.03551
	Stress limit	σ_0	psf	429,613 (20.57 MPa)
	Stress constant	q	-	5335
Transient strain (Eq. 8)	Material constant	m	-	3.0
	Constant	K_0	-	***K0F***††×627,500
	Constant	c	1/K	0.009198
Work-hardening and recovery (Eq. 9&10)	Constant	α	-	-17.37
	Constant	β	-	-7.738
	Recovery	δ	-	0.58
	Damage	ω	-	0.0
Structure factor multiplication factor from WIPP 25°C salt		*SMF*	-	1.170
Scalar multiplier of time step needed for stability		*AMULT*	-	0.95
System parameters for numerical convergence		*ANGLE*	-	0.1
		epstol	-	0.005
		grwfac	-	1.05
		shkfac	-	1.0
		ITHPE		0.0

Note:
* – Temperature value is assigned on every node in the mesh
** -The value (lb/ft^3/gr) will be multiplied by gravity (32.174 ft/s^2) in the system
‡ – ADAGIO requests the value be divided by universal gas constant
† – A_2 multiplication factor to examine the A_2 factor effect
†† - K_0 multiplication factor to examine the K_0 factor effect

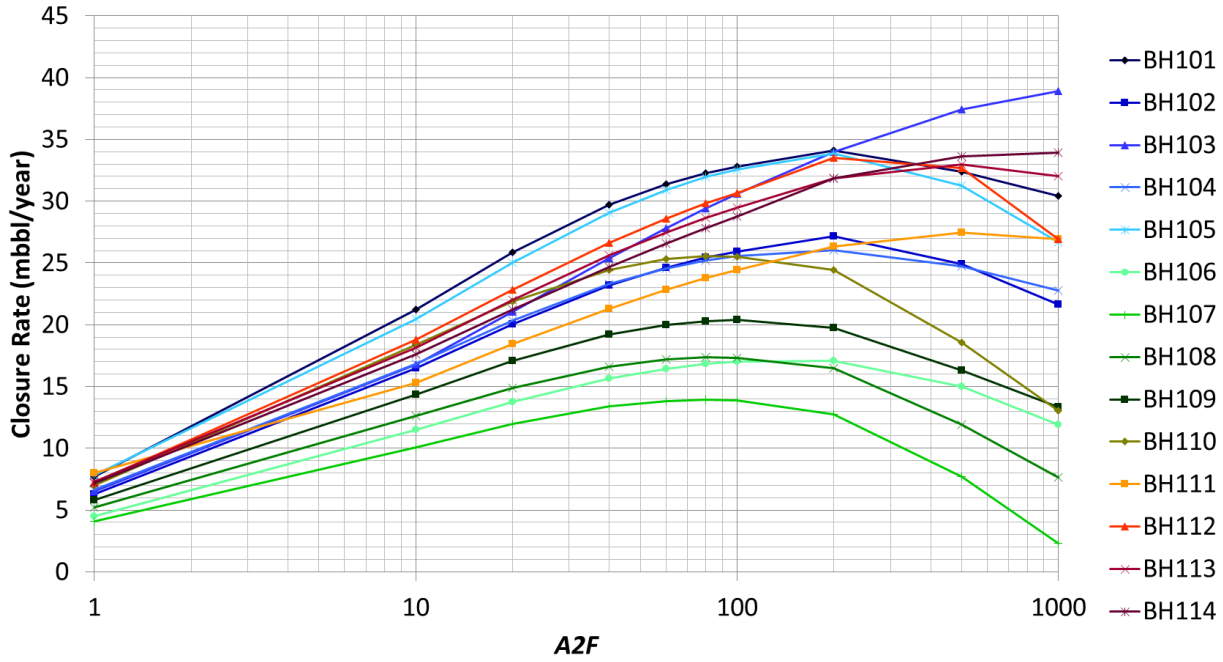

Figure 26 Relationship between *A2F* and slopes (cavern volume closure rate) when *K0F*=1 for 14 caverns [Park, 2018]

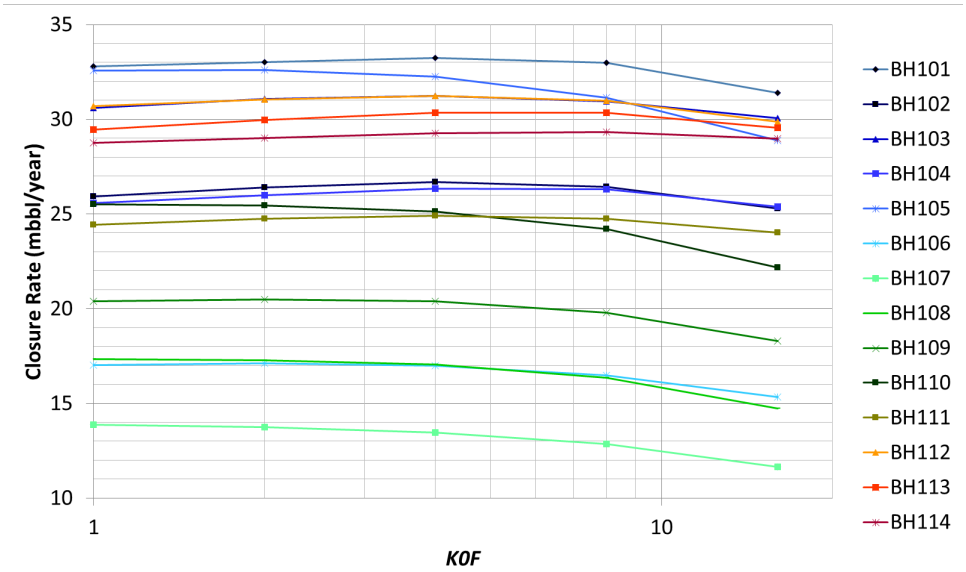

Figure 27 Relationship between *K0F* and slopes (cavern volume closure rate) of trendlines when *A2F*=100 for 14 caverns [Park, 2018]

7. MODEL CALIBRATION

7.1. Volumetric Closure

Based on the relationships between slopes, *A2F* and *K0F* in Figure 26 and Figure 27, the values of *A2F* and *K0F* have been calibrated through a number of back-fitting analyses and determined as listed Table 7. *A2F*=100 and *K0F*=1 are applied to the entire salt dome except for the cavern skins, then each *A2F* and *K0F* values are applied into the salt skins encompassing each cavern cavity as shown Figure 15. The cavern curves normalized to the initial volumes of SPR caverns calculated from CAVEMAN as shown Figure 25 are used as a back-fitting standard.

Table 7 Calibrated values of multiplication factors applied to the A_2 and K_0 in Table 6

Cavern ID	*A2F*	*K0F*
Salt except SPR cavern skins	100.	1.0
BH101 salt skins	150.	4.0
BH102 salt skins	180.	4.0
BH103 salt skins	70.	1.0
BH104 salt skins	20.	1.0
BH105 salt skins	180.	2.0
BH106 salt skins	10.	1.0
BH107 salt skins	80.	0.1
BH108 salt skins	80.	0.1
BH109 salt skins	100.	2.0
BH110 salt skins	80.	1.0
BH111 salt skins	0.5	1.0
BH112 salt skins	0.05	1.0
BH113 salt skins	180.	4.0
BH114 salt skins	180.	8.0

Figure 28 shows the volumetric closure normalized calculated using calibrated *A2F* and *K0F* values from Table 9 to initial cavern volumes based on CAVEMAN predictions for 14 SPR caverns. The solid and dashed curves indicate the normalized volumetric closure predicted from the analysis and CAVEMAN, respectively. The analyses results still do not match well to CAVEMAN's especially in the period of normal operating conditions (steady-state periods).

In the West Hackberry analysis, this significant difference was also shown. *The slopes of the steady-state periods between workovers are still significantly different between measurements and predictions* [Sobolik, 2015].

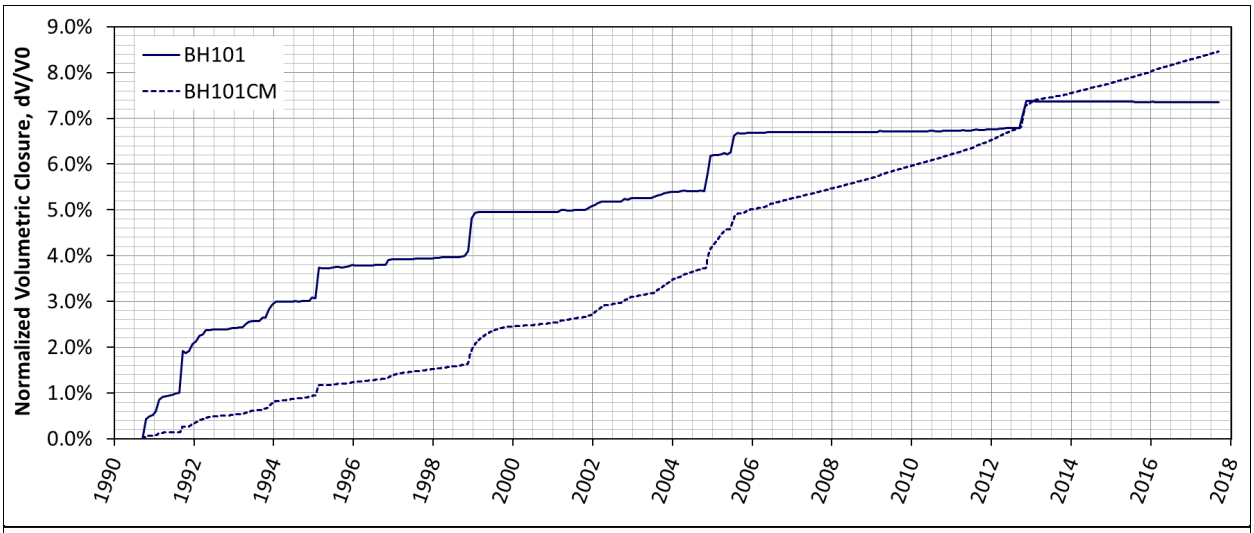
Normalized Volumetric Closure, dV/V0
9.0%
8.0%
7.0%
6.0%
5.0%
4.0%
3.0%
2.0%
1.0%
0.0%
BH101
BH101CM
1990
1992
1994
1996
1998
2000
2002
2004
2006
2008
2010
2012
2014
2016
2018

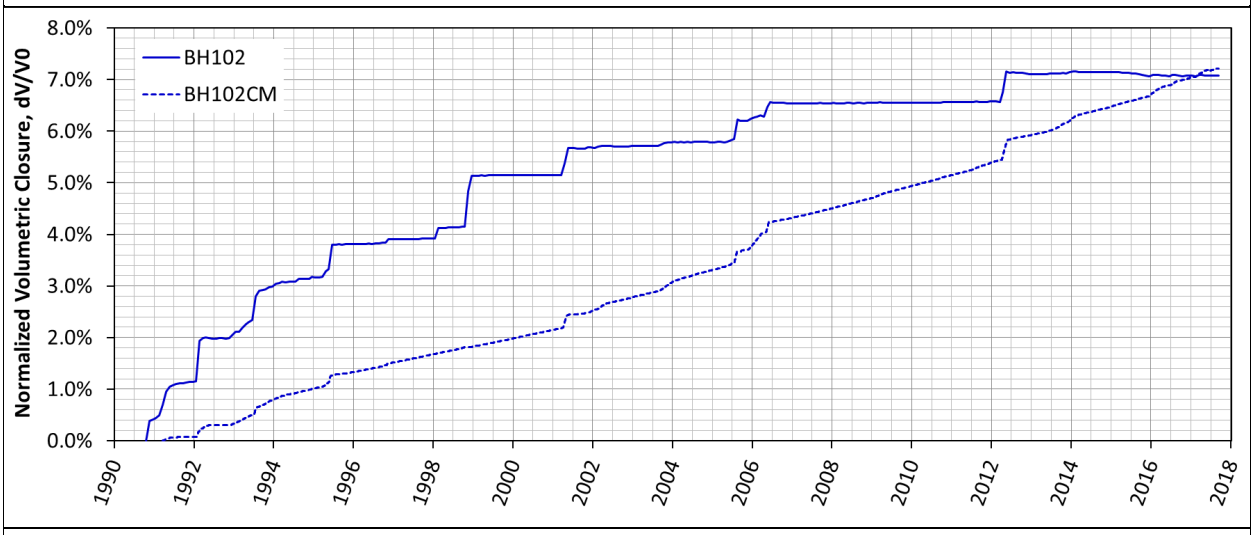
Normalized Volumetric Closure, dV/V0
8.0%
7.0%
6.0%
5.0%
4.0%
3.0%
2.0%
1.0%
0.0%
BH102
BH102CM
1990
1992
1994
1996
1998
2000
2002
2004
2006
2008
2010
2012
2014
2016
2018

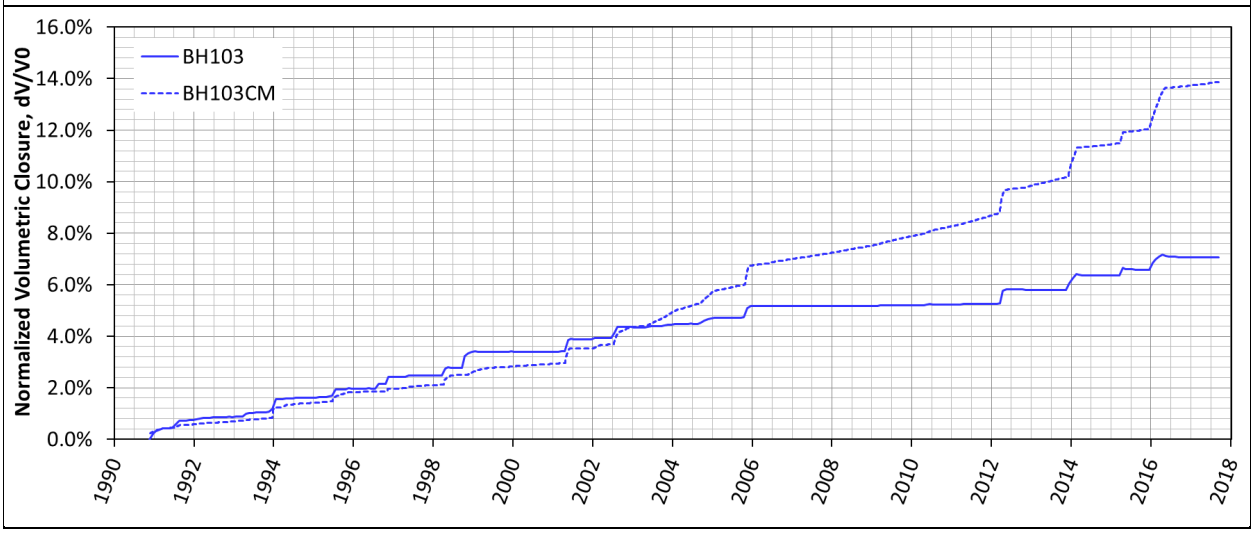
Normalized Volumetric Closure, dV/V0
16.0%
14.0%
12.0%
10.0%
8.0%
6.0%
4.0%
2.0%
0.0%
BH103
BH103CM
1990
1992
1994
1996
1998
2000
2002
2004
2006
2008
2010
2012
2014
2016
2018

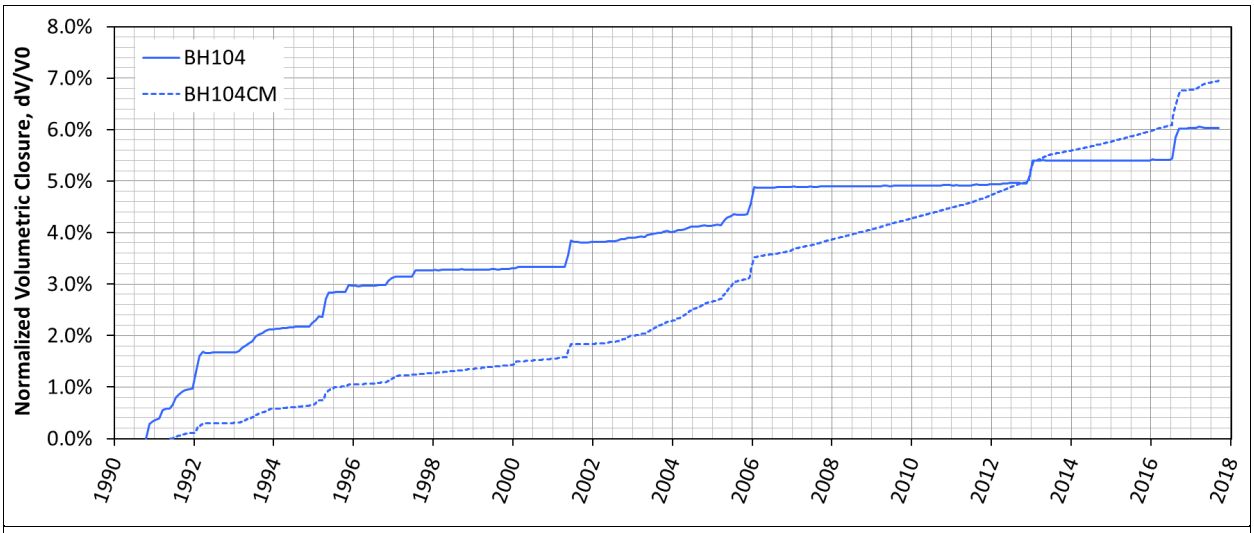
Normalized Volumetric Closure, dV/V0
8.0%
7.0%
6.0%
5.0%
4.0%
3.0%
2.0%
1.0%
0.0%
BH104
BH104CM
1990
1992
1994
1996
1998
2000
2002
2004
2006
2008
2010
2012
2014
2016
2018

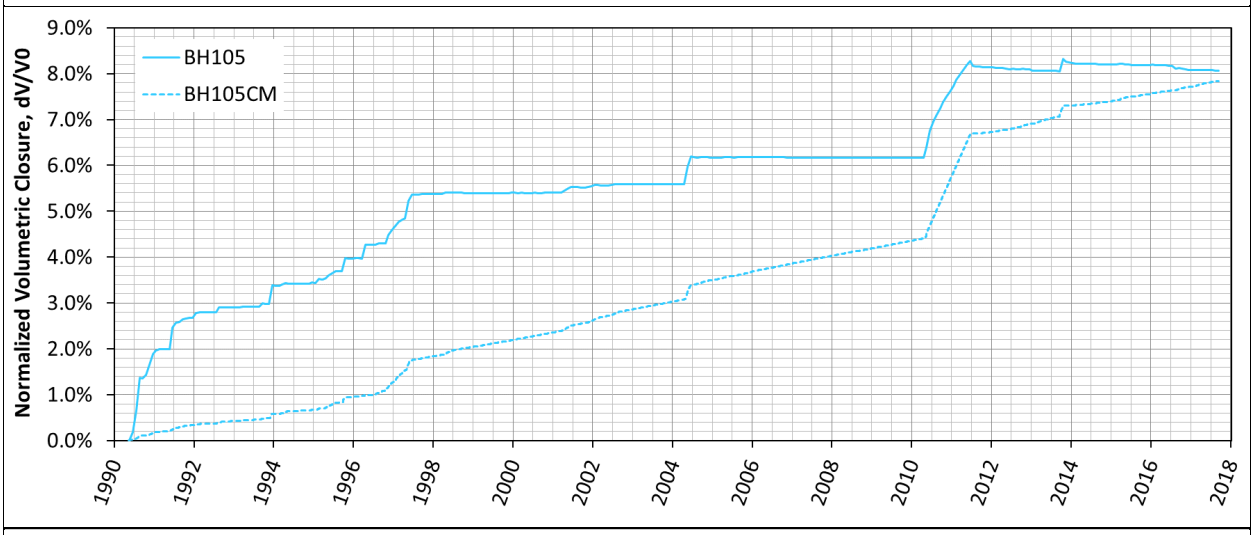
Normalized Volumetric Closure, dV/V0
9.0%
8.0%
7.0%
6.0%
5.0%
4.0%
3.0%
2.0%
1.0%
0.0%
BH105
BH105CM
1990
1992
1994
1996
1998
2000
2002
2004
2006
2008
2010
2012
2014
2016
2018

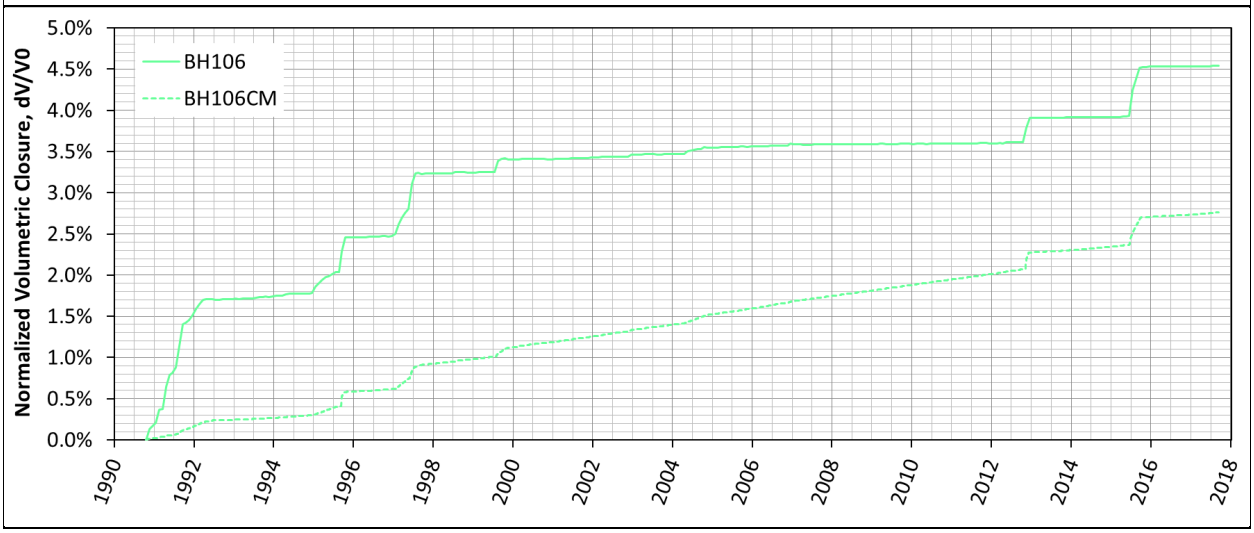
Normalized Volumetric Closure, dV/V0
5.0%
4.5%
4.0%
3.5%
3.0%
2.5%
2.0%
1.5%
1.0%
0.5%
0.0%
BH106
BH106CM
1990
1992
1994
1996
1998
2000
2002
2004
2006
2008
2010
2012
2014
2016
2018

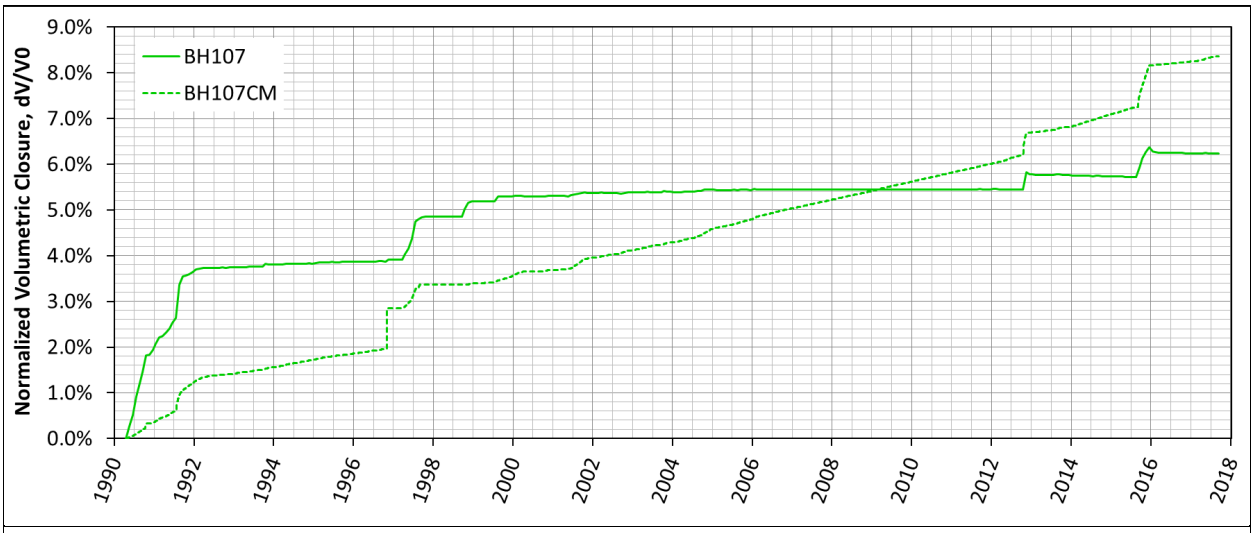
Normalized Volumetric Closure, dV/V0
9.0%
8.0%
7.0%
6.0%
5.0%
4.0%
3.0%
2.0%
1.0%
0.0%
BH107
BH107CM
1990
1992
1994
1996
1998
2000
2002
2004
2006
2008
2010
2012
2014
2016
2018

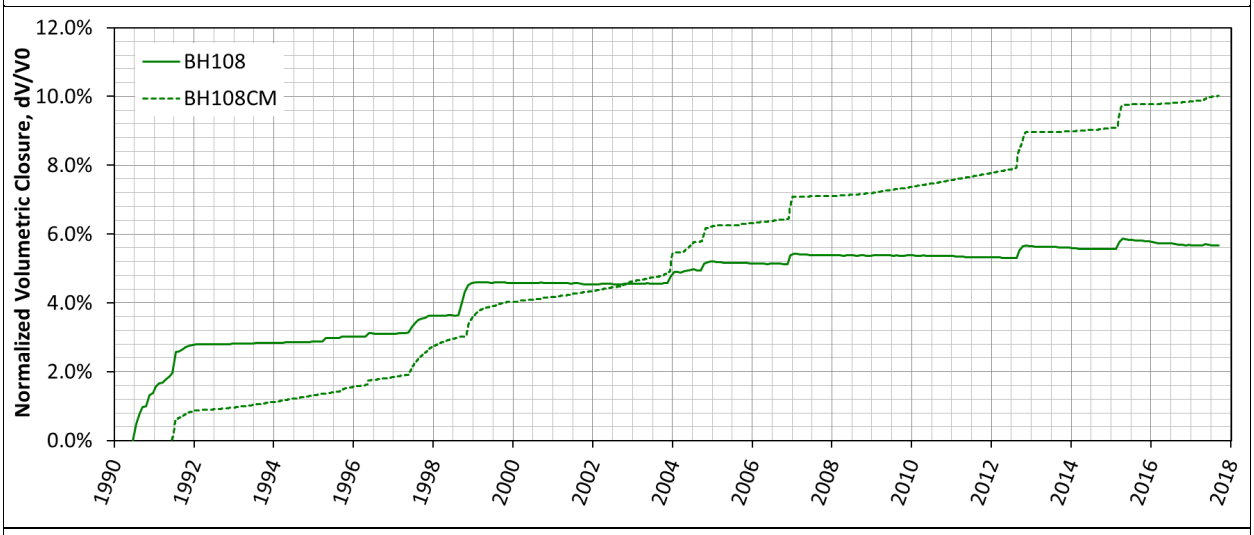
Normalized Volumetric Closure, dV/V0
12.0%
10.0%
8.0%
6.0%
4.0%
2.0%
0.0%
BH108
BH108CM
1990
1992
1994
1996
1998
2000
2002
2004
2006
2008
2010
2012
2014
2016
2018

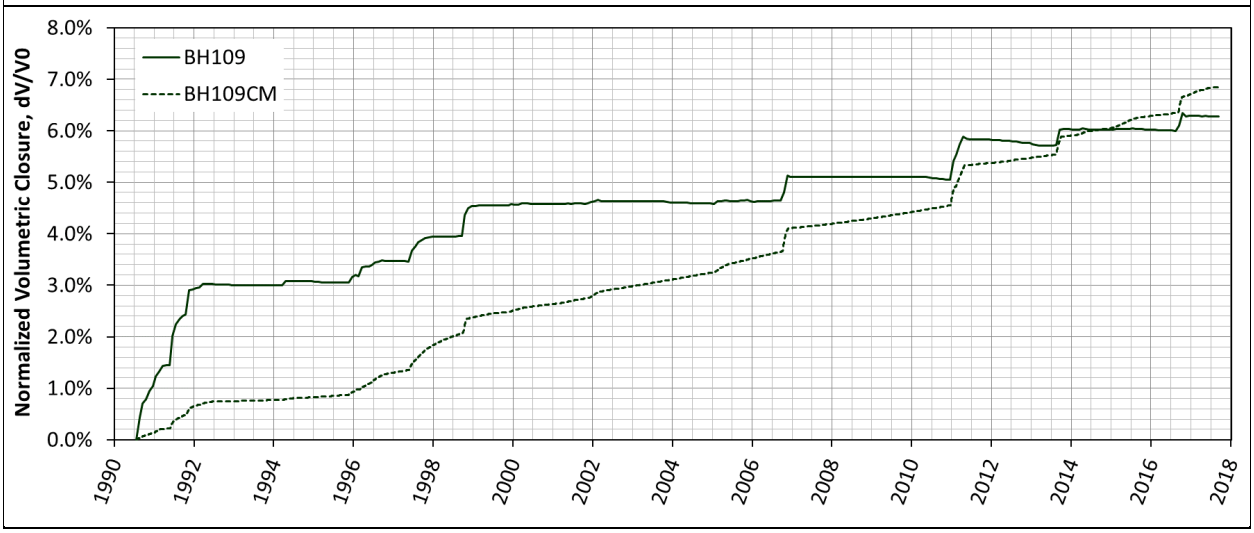
Normalized Volumetric Closure, dV/V0
8.0%
7.0%
6.0%
5.0%
4.0%
3.0%
2.0%
1.0%
0.0%
BH109
BH109CM
1990
1992
1994
1996
1998
2000
2002
2004
2006
2008
2010
2012
2014
2016
2018

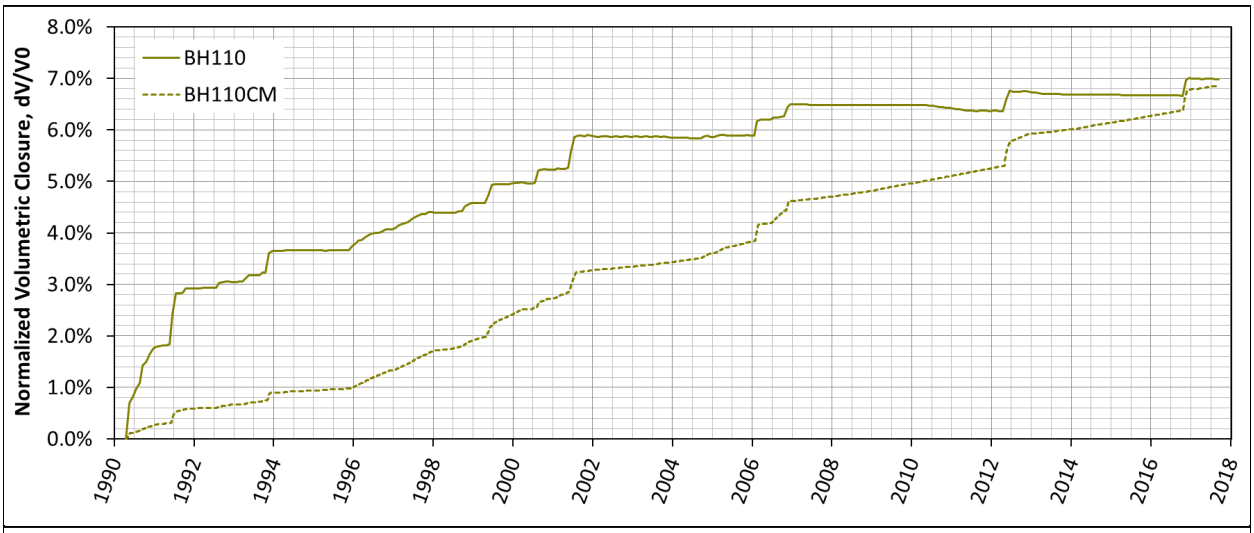
Normalized Volumetric Closure, dV/V0
8.0%
7.0%
6.0%
5.0%
4.0%
3.0%
2.0%
1.0%
0.0%
BH110
BH110CM
1990
1992
1994
1996
1998
2000
2002
2004
2006
2008
2010
2012
2014
2016
2018

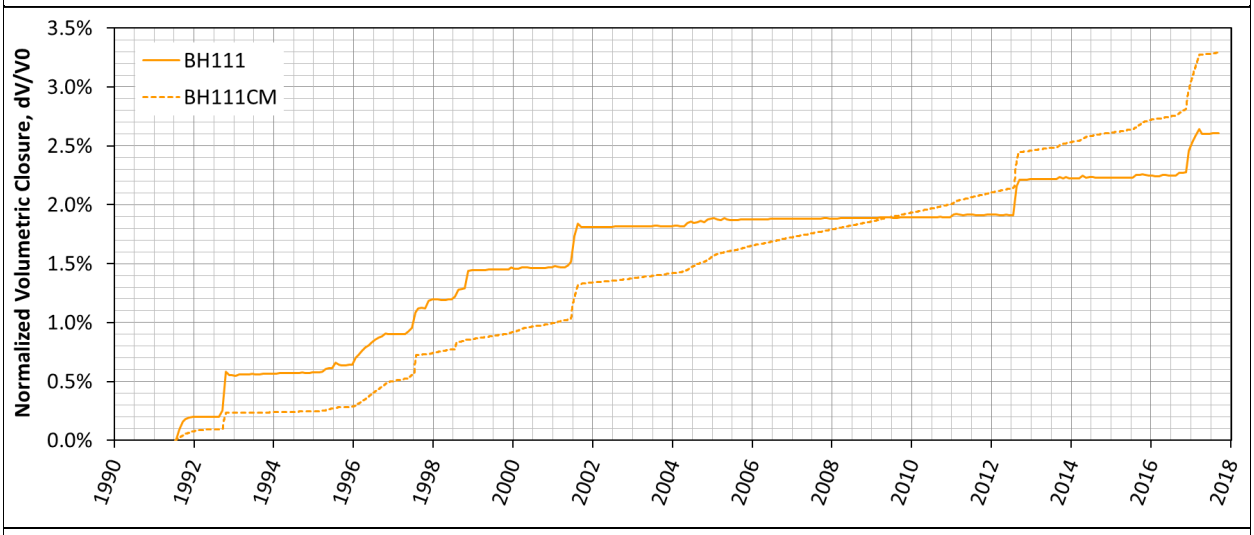
Normalized Volumetric Closure, dV/V0
3.5%
3.0%
2.5%
2.0%
1.5%
1.0%
0.5%
0.0%
BH111
BH111CM
1990
1992
1994
1996
1998
2000
2002
2004
2006
2008
2010
2012
2014
2016
2018

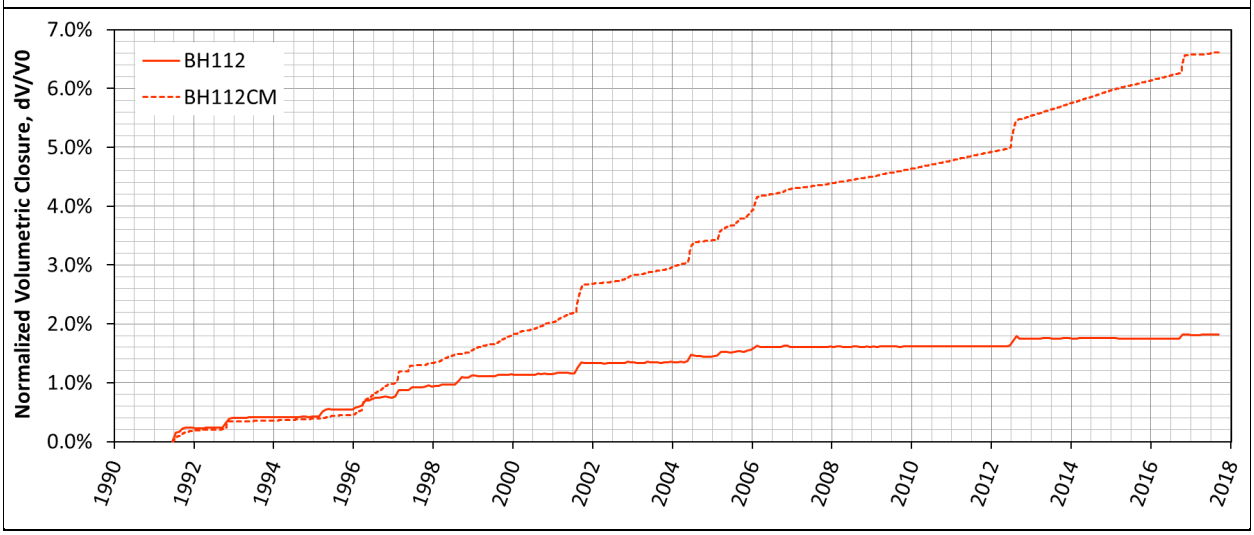
Normalized Volumetric Closure, dV/V0
7.0%
6.0%
5.0%
4.0%
3.0%
2.0%
1.0%
0.0%
BH112
BH112CM
1990
1992
1994
1996
1998
2000
2002
2004
2006
2008
2010
2012
2014
2016
2018

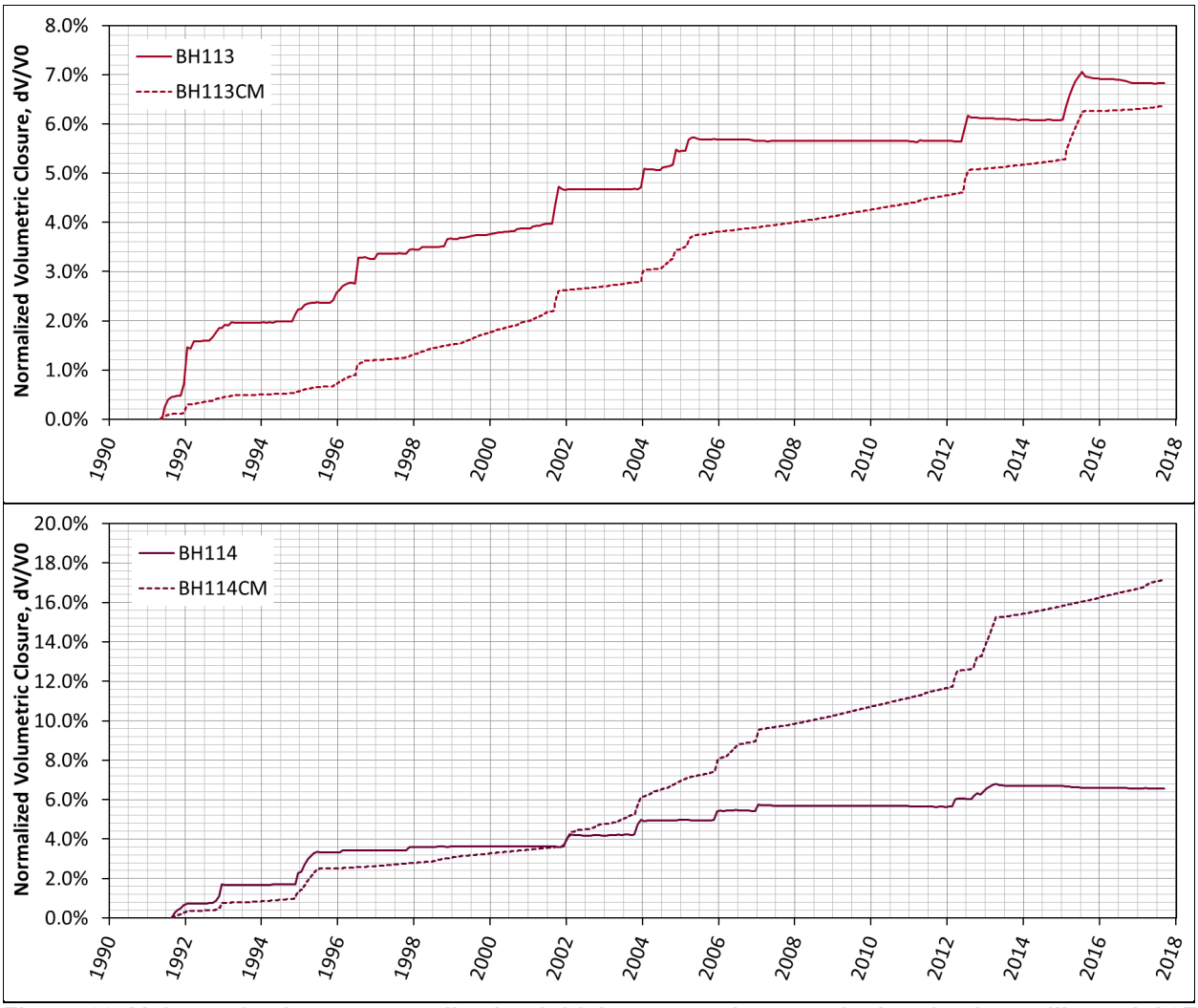

Figure 28 Volumetric closure normalized to initial cavern volumes calculated using calibrated *A2F* and *K0F* in Table 9 with CAVEMAN predictions for 14 SPR caverns

7.2. Sonar Surveyed Volumes

The cavern volume change estimated by CAVEMAN may be unreliable, because CAVEMAN was developed for monitoring cavern pressure. The pressure is used to indirectly estimate the daily cavern volume closure [Park, 2018]. The sonar measurement data, on the other hand, should be a more direct measurement than the CAVEMAN estimates and, for that reason, is used to calibrate the finite element model.

Table 8 lists the BH103 cavern volumes measured by sonar survey with the survey date as an example. The cavern volume decreases with time due to salt creep. However, the volume increases on 10/4/2011 because it does not consider the additional leached volume before that.

Table 9 lists the injected raw water volume and the leached volume due to the raw water as provided by Hart [2018]. Figure 29 shows the amount of raw water injected into each cavern with time. The circles in blue and orange indicate the injected raw water and leached salt volumes, respectively. The leached salt volume is assumed to be 16% of the injected water amount as mentioned in Section 3.1.

The FE computational model in this study cannot consider the cavern volumetric change due to the small amount of injected raw water. Therefore, the true cavern volume in the model on a day of sonar survey is calculated to be the sonar volume measured on the day subtracted by the leached volumes in the cavern life time as follows:

$$V_{on\ day2} = V_{sonar\ on\ day1} - V_{creep\ for\ (day2-day1)} \quad (12)$$

$$V_{sonar\ on\ day2} = V_{sonar\ on\ \ day1} - V_{creep\ for\ (day2-day1)} + V_{leached\ total} \quad (13)$$

Thus, $V_{on\ day2} = V_{sonar\ on\ day2} - V_{leached\ total}$ (14)

Table 10 lists the BH103 cavern volume measured by sonar survey subtracting the leached volume. Then, the cavern volume (indicated by black diamonds) decreases with time as shown Figure 30.

Figure 30 shows the predicted BH103 volume change over time with linear trendline when *A2F*=1 and *K0F*=1. The predicted cavern closure rate is calculated to be 17.87 bbl/day (6.53 mbbl/yr), while the closure rate measured by sonar is 81.99 bbl/day (29.95 mbbl/yr). To match the closure rate, *A2F* and *K0F* are calibrated through a number of back-fitting analyses. Figure 31 shows the predicted BH103 volume change over time with linear trendline when *A2F*=70 and *K0F*=1 listed in Table 7. The trendlines for the sonar measurement and prediction match well. The predicted cavern volume (blue curve) is close to the sonar data (diamonds).

Table 8. BH103 – Cavern volumes measured by sonar survey

Sonar Date	Cavern Volume		Reference
	(bbl)	(m^3)	
12/06/1990	12,931,752	2,055,984	Boeing Petroleum Services, Inc. 103A Dec. 6, 1990
03/28/2002	12,659,238	2,012,658	DynMcDermott Petroleum Operations Co. 103A March 28, 2002
04/23/2009	12,416,235	1,974,024	DynMcDermott Petroleum Operations, Co. 103A - Apr. 23,2009
10/04/2011	12,582,718	2,000,492	BH103A-2011-10-04.pdf

Table 9. BH103 – Injected raw water volumes from 1997 to 2017 and leached volumes due to the raw water

Leaching Date	Raw Water Injected (A) (bbl)	Cavern Volume Increase due to Injected Water (16% of A)	
		(bbl)	(m^3)
7/15/2001	4,056	649	103
3/15/2002	13,170	2,107	335
7/15/2004	16,022	2,564	408
1/15/2005	1,914	306	49
6/15/2005	63,142	10,103	1,606
10/15/2005	148,373	23,740	3,774
11/15/2006	35,190	5,630	895
3/15/2009	3,760	602	96
4/15/2009	5,895	943	150
7/15/2011	7,049	1,128	179
8/15/2011	1,303,056	208,489	33,147
5/15/2012	13,247	2,120	337
4/15/2015	3,893	623	99
5/15/2016	42,634	6,821	1,085
6/15/2016	3,371	539	86

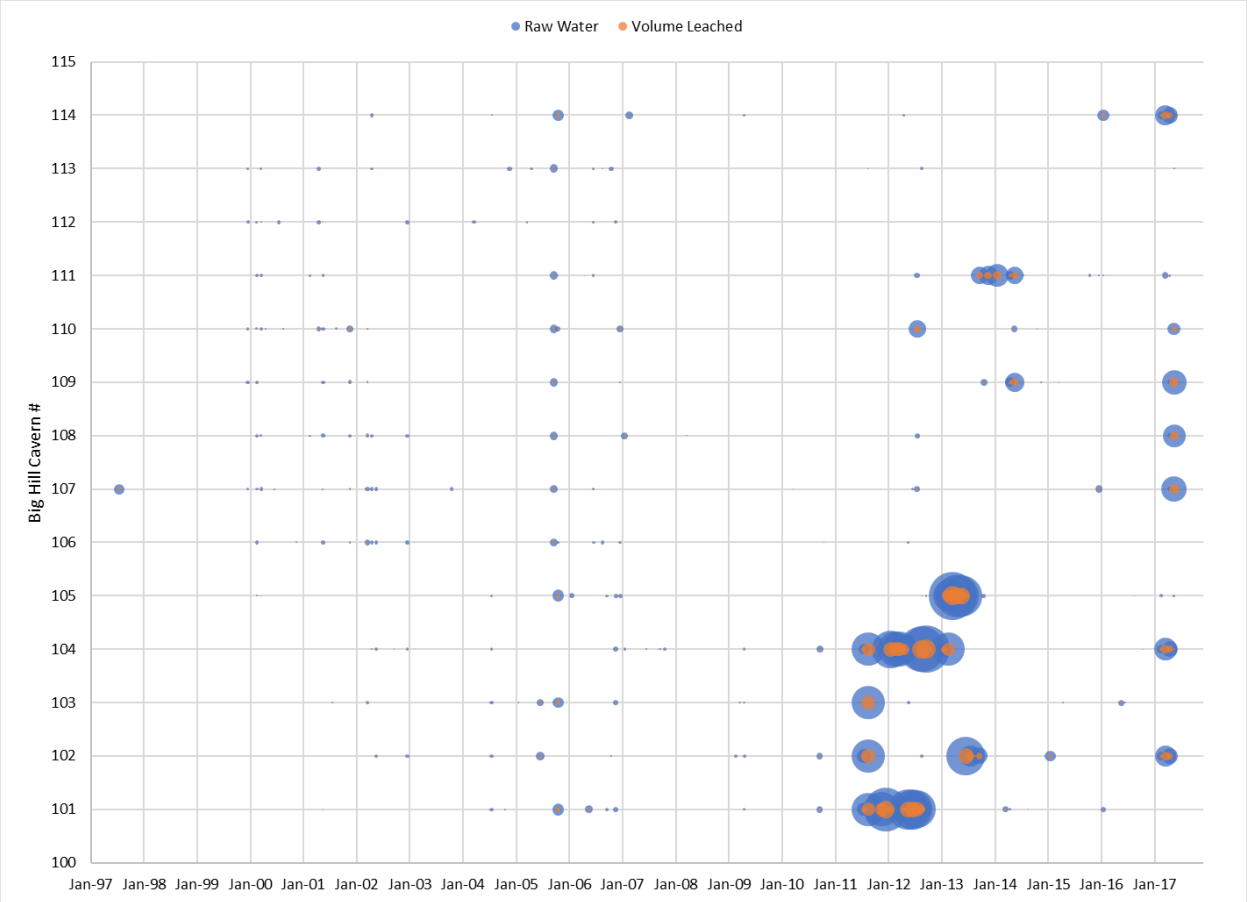

Figure 29. Month-by-month raw water movements in the Big Hill SPR caverns from 1997 to 9/29/2017 [Hart, 2018]

Table 10. BH103 – Cavern volume measured by sonar survey considering leached volume

Date	Sonar Volume (bbl) in Table 10 (B)	Cavern Volume Increase (bbl) in Table 11 (A)	Cavern Volume Considering Leaches (B-A)
12/06/1990	12,931,752		12,931,752
07/15/2001		649	
03/15/2002		2,107	
03/28/2002	12,659,238		12,656,482
07/15/2004		2,564	
01/15/2005		306	
06/15/2005		10,103	
10/15/2005		23,740	
11/15/2006		5,630	
03/15/2009		602	
04/15/2009		943	
04/23/2009	12,416,235		12,369,592
07/15/2011		1,128	
08/15/2011		208,489	
10/04/2011	12,582,718		12,326,458
05/15/2012		2,120	
04/15/2015		623	
05/15/2016		6,821	
06/15/2016		539	

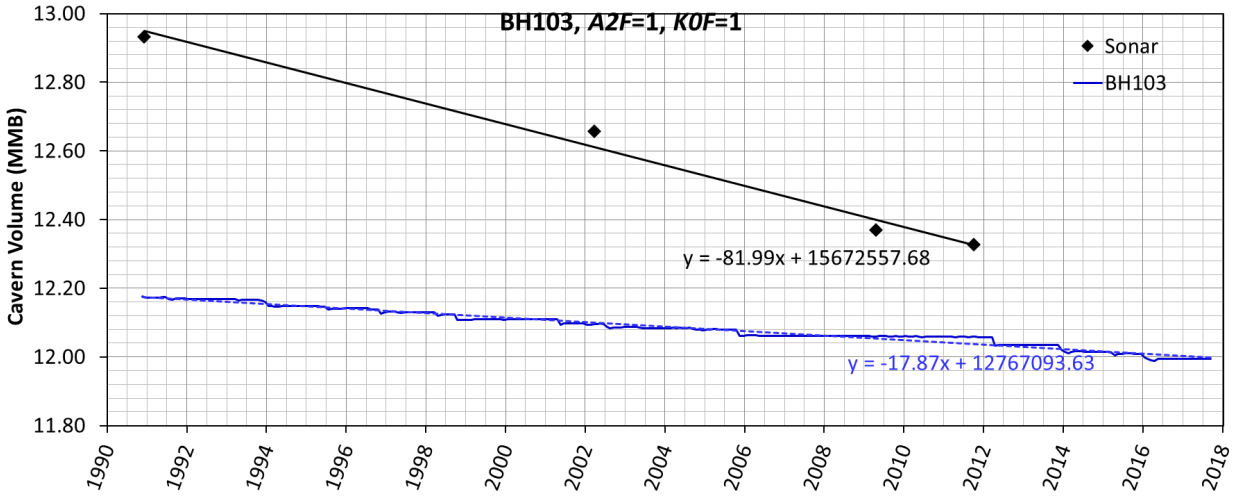

Figure 30. BH103 – Cavern volume change with time measured by sonar survey considering leached volume with linear trendline, and predicted volume change over time with linear trendline when *A2F*=1 and *K0F*=1

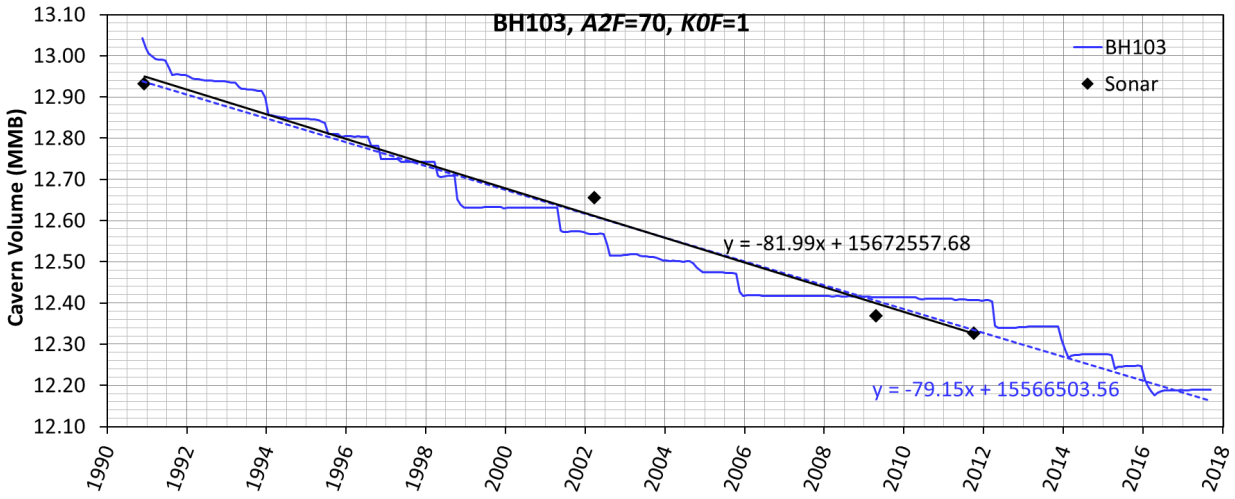

Figure 31. BH103 – Cavern volume change with time measured by sonar survey considering leached volume with linear trendline, and predicted volume change over time with linear trendline when *A2F*=70 and *K0F*=1

7.3. CAVEMAN vs. Sonar

Table 11 lists the cavern closure rates from the CAVEMAN estimates [Bettin et al., 2018] and sonar measurement with the leached volumes. The results are also shown in Figure 32. The values for BH101, 102, 106, and 113 are close to each other, but for the other caverns can be significantly different. A discussion is needed to decide which is better to use as the field reference data for the model calibration. Figure 33 shows the cavern closure rates by sonar survey for 14 SPR caverns.

Table 11. Big Hill cavern volume closure rates calculated using the data from CAVEMAN and sonar survey

Cavern ID	Cavern Closure Rate		Applied Period for Sonar Data		Duration (years)
	CAVEMAN (mbbl/year)	Sonar capturing leaches (mbbl/year)	Begin	End	
BH-101	40.48	32.69	01/29/1991	01/04/2012	20.95
BH-102	35.55	41.16	03/22/1991	08/29/2013	22.45
BH-103	67.46	29.95	12/06/1990	10/04/2011	20.84
BH-104	34.22	22.65	01/15/1991	04/17/2018	27.27
BH-105	37.08	53.91	07/12/1990	07/16/2013	23.03
BH-106	13.24	13.80	01/23/1991	03/31/2015	24.20
BH-107	39.70	25.27	12/15/1990	08/19/2010	19.69
BH-108	49.29	79.84	12/20/1990	04/24/2015	24.36
BH-109	32.60	52.12	01/03/1991	05/05/2015	24.35
BH-110	32.51	28.70	08/09/1990	04/08/2015	24.68
BH-111	16.25	8.01	08/02/1991	04/09/2015	23.70
BH-112	32.59	7.44	07/22/1991	05/07/2015	23.81
BH-113	31.33	36.81	06/25/1991	09/14/2015	24.24
BH-114	85.04	56.13	09/06/1991	10/24/2013	22.15

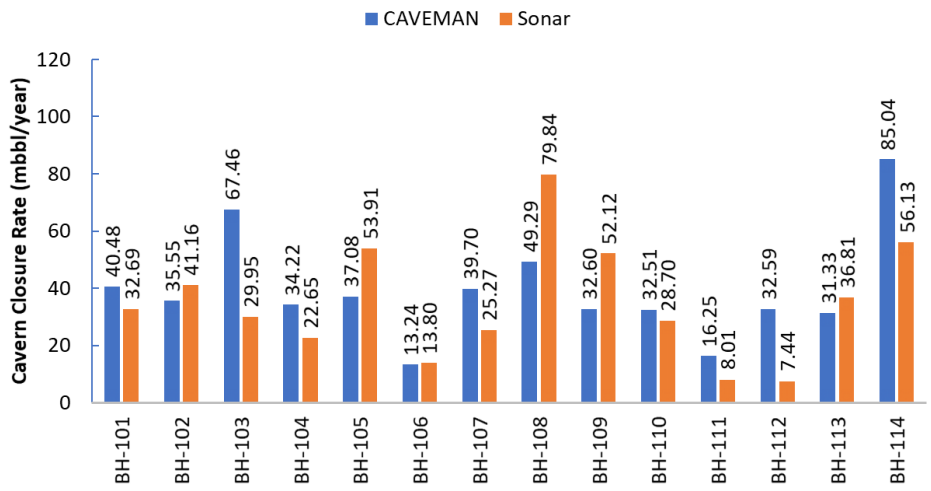

Figure 32. Cavern closure rates calculated by CAVEMAN and sonar measurements

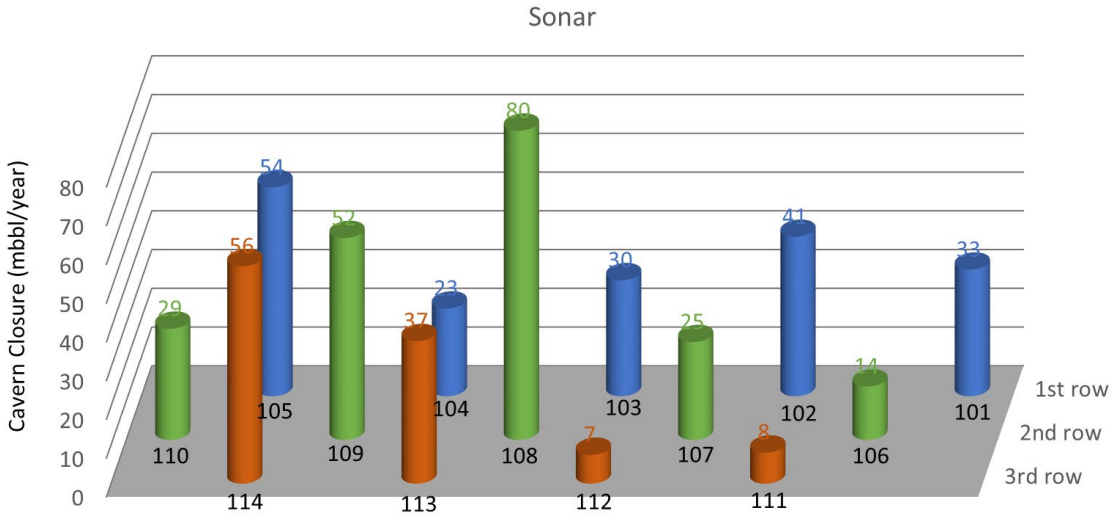

Figure 33.Cavern volume closure rate calculated using sonar measurements

7.4. Predicted Cavern Volume Change

In the same manner as described in Section 7.2, the A_2 and K_0 values are calibrated to produce the best match between the sonar measurement and model predictions. The multiplication factor values of *A2F* and *K0F* are determined as listed in Table 7 through the back-fitting analyses. The predicted cavern volume change over time when the values in Table 7 are used for each cavern is shown in Figure 34. The linear trendlines of each cavern volume change curve and sonar measurements are also shown.

The trendlines of the predictions and sonar data matchup well for BH 101, 103, 104, 106, 110, 111, 112, and 113. The sonar data (diamonds) are close to the prediction curves for BH 102 and 114. However, the prediction curves for BH 105, 107, 108, and 109 are far away from the sonar data.

Munson [2000] evaluated the various measures to obtain an indication of the uncertainties in the cavern volume measurement. Throughout the history of the SPR project, there have been three independent measures of cavern volume maintained. These are: (1) a calculated solution volume determined by raw water injections and brine extractions during construction and any subsequent fluid transfers or additions, (2) a calculated volume obtained from the geometric dimensions of the cavern as determined by sonar measurements, and (3) a partial cavern volume as determined from the metered quantity of oil occupying that volume. The intent of this study is to evaluate the various measures to obtain an indication of the uncertainties. ... Of the four sites, Big Hill not only had an extensive database, but provided the best conditions for comparison. ... The results for Big Hill suggested behavior that was confirmed by the data of the other sites. The comparisons showed that a bias, or systematic deviation from the perfect relationship, which depends upon the sonar survey operator, exists for the sonar surveys. This bias is quite different for different datasets, it can be either negative or positive, and varies in most cases from –9% to +9%, but may be even greater.

There is out of consistency in the sonar data i.e., the volume measured later is larger than that before in some time intervals, even if the leached volume is taken into account, for BH 101, 104, 106, 107, and 112. The causes might be the followings:

1. Uncertainty in the sonar measurements – The cavern volume measured by the sonar survey is known to have an error of about ±9%, and the sonar measurement techniques and methods used in the 1990s and 2000s have changed.
2. Leak of data - There is no row water injection data prior to 1997.

There is a limitation to calibrate the prediction using *A2F* and *K0F* because the closure rates increase until a certain value of them, but decrease after that as shown Figure 26 and Figure 27. The discussions are needed to solve the issues.

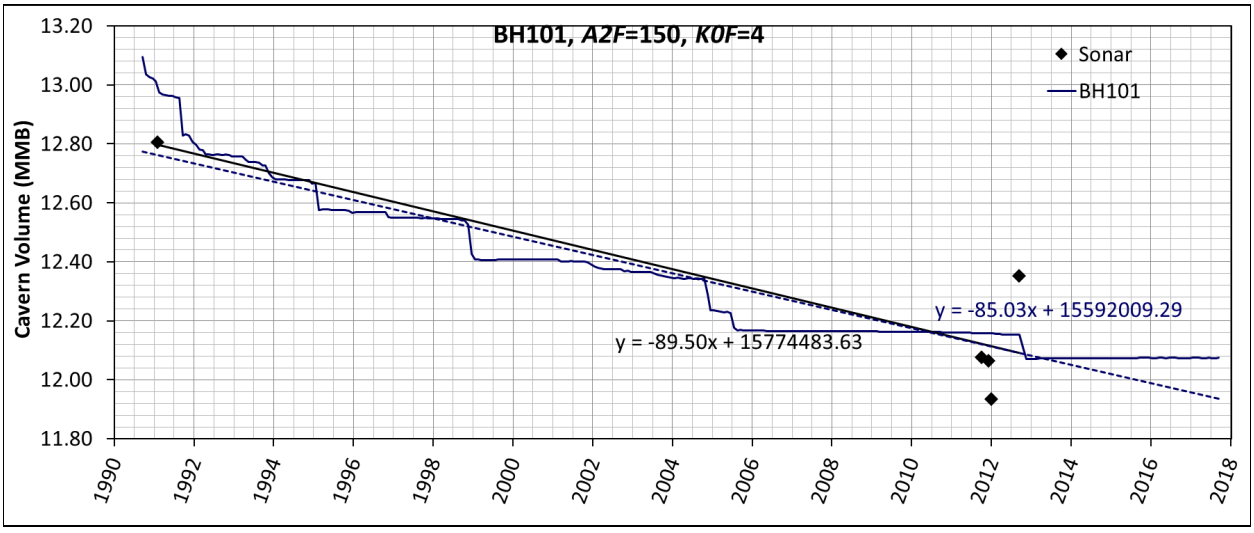

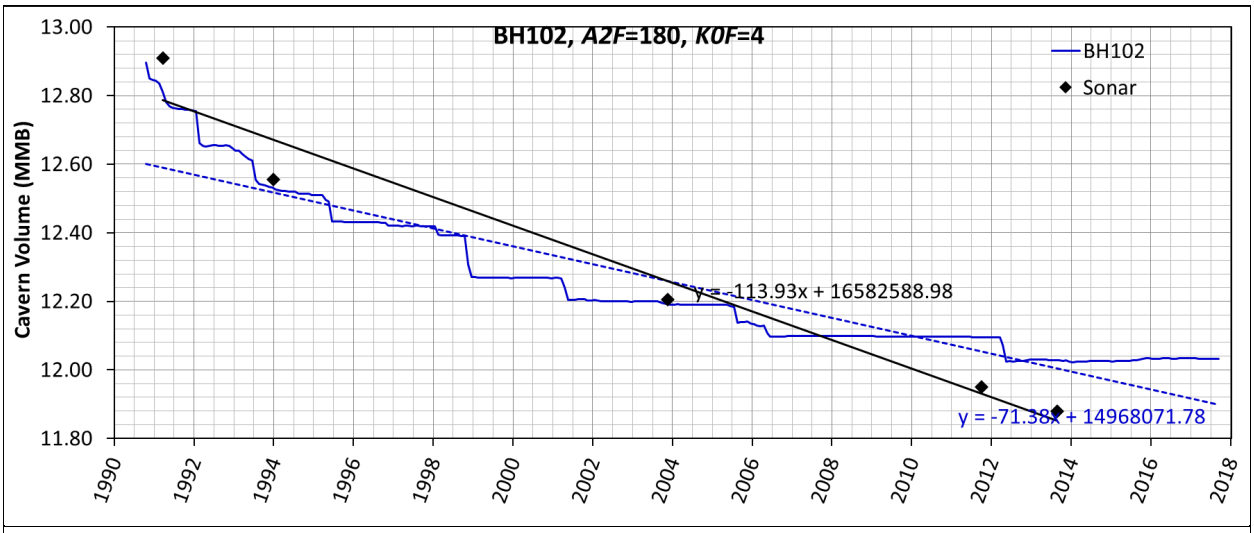
BH102, A2F=180, K0F=4
BH102
Sonar
Cavern Volume (MMB)
y = -113.93x + 16582588.98
y = -71.38x + 14968071.78

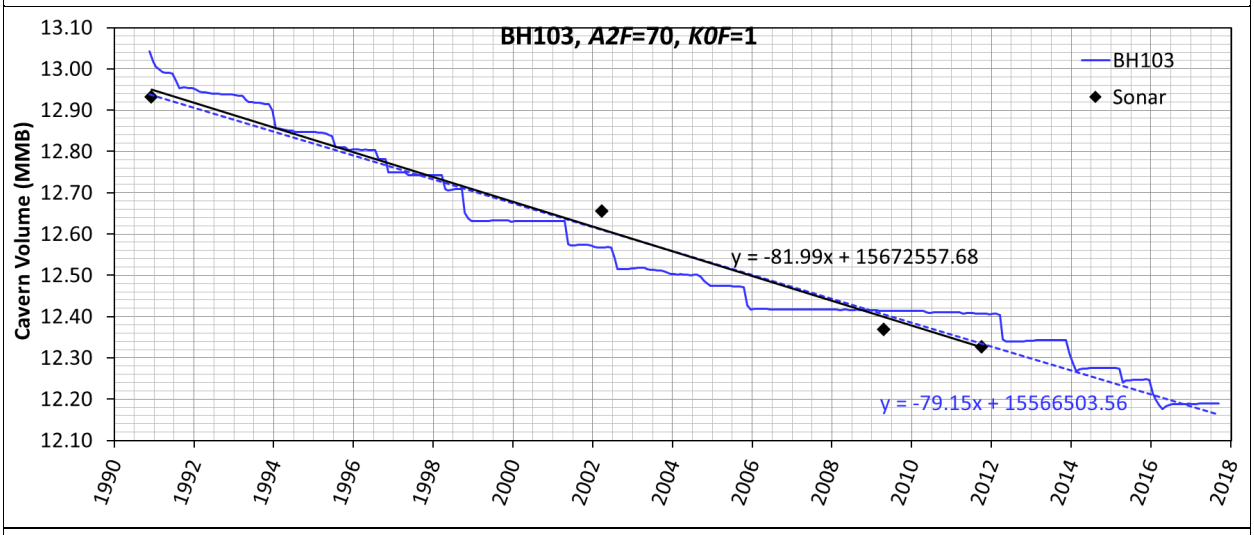
BH103, A2F=70, K0F=1
BH103
Sonar
Cavern Volume (MMB)
y = -81.99x + 15672557.68
y = -79.15x + 15566503.56

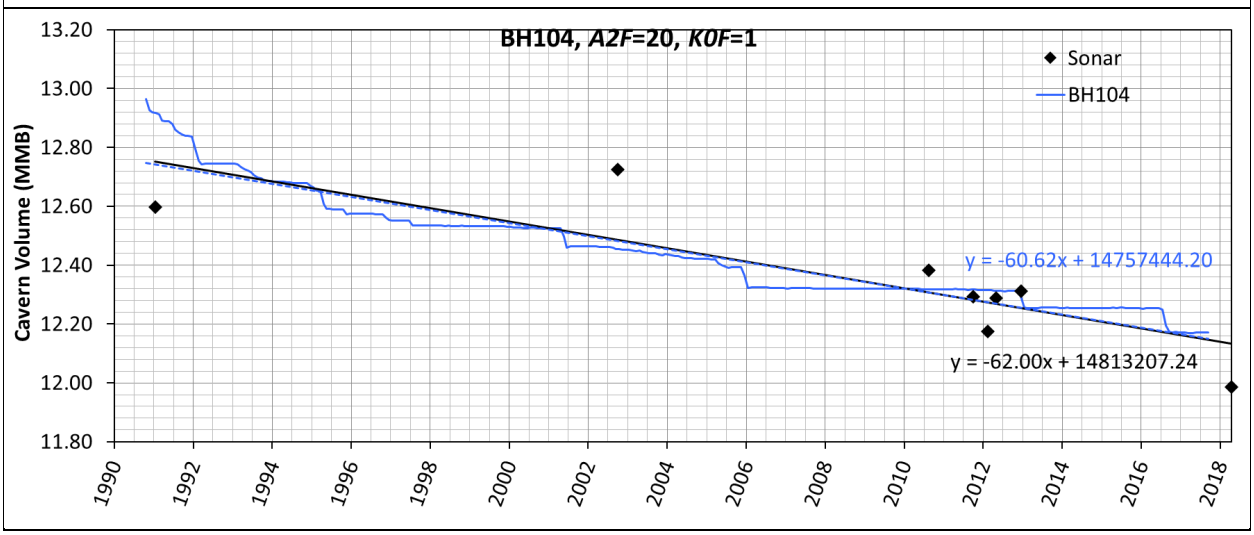
BH104, A2F=20, K0F=1
Sonar
BH104
Cavern Volume (MMB)
y = -60.62x + 14757444.20
y = -62.00x + 14813207.24

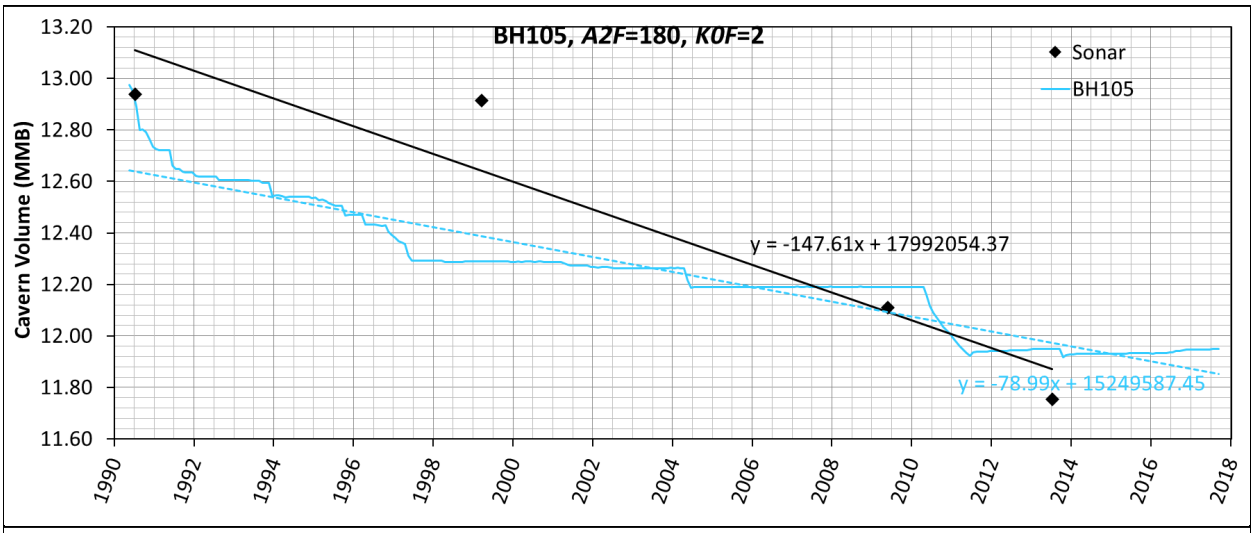
BH105, A2F=180, K0F=2
Sonar
BH105
Cavern Volume (MMB)
y = -147.61x + 17992054.37
y = -78.99x + 15249587.45
13.20
13.00
12.80
12.60
12.40
12.20
12.00
11.80
11.60
1990
1992
1994
1996
1998
2000
2002
2004
2006
2008
2010
2012
2014
2016
2018

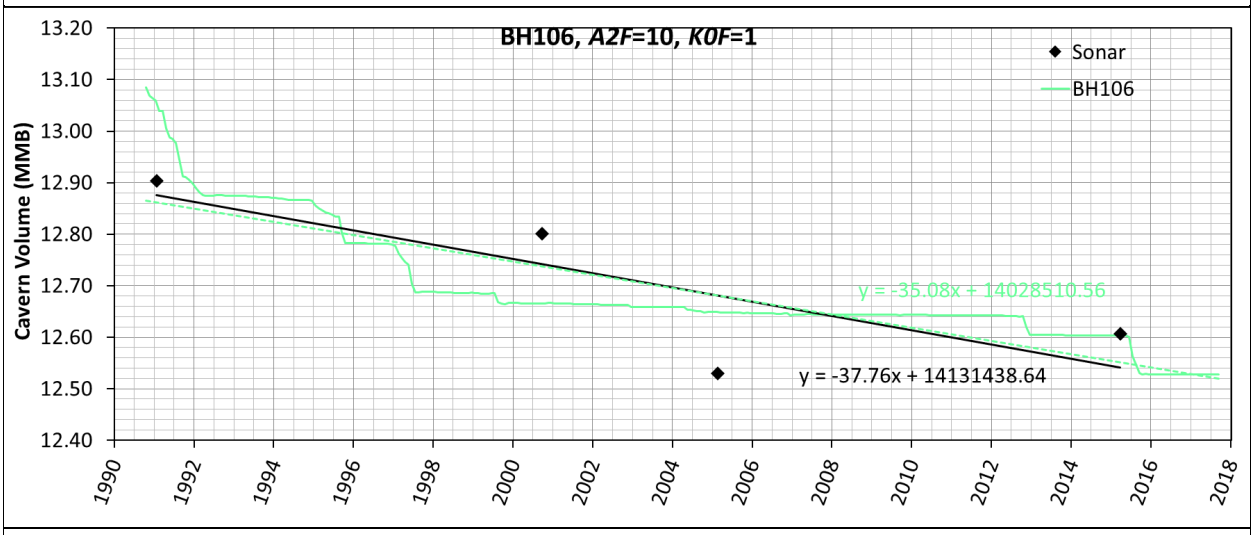
BH106, A2F=10, K0F=1
Sonar
BH106
Cavern Volume (MMB)
y = -35.08x + 14028510.56
y = -37.76x + 14131438.64
13.20
13.10
13.00
12.90
12.80
12.70
12.60
12.50
12.40
1990
1992
1994
1996
1998
2000
2002
2004
2006
2008
2010
2012
2014
2016
2018

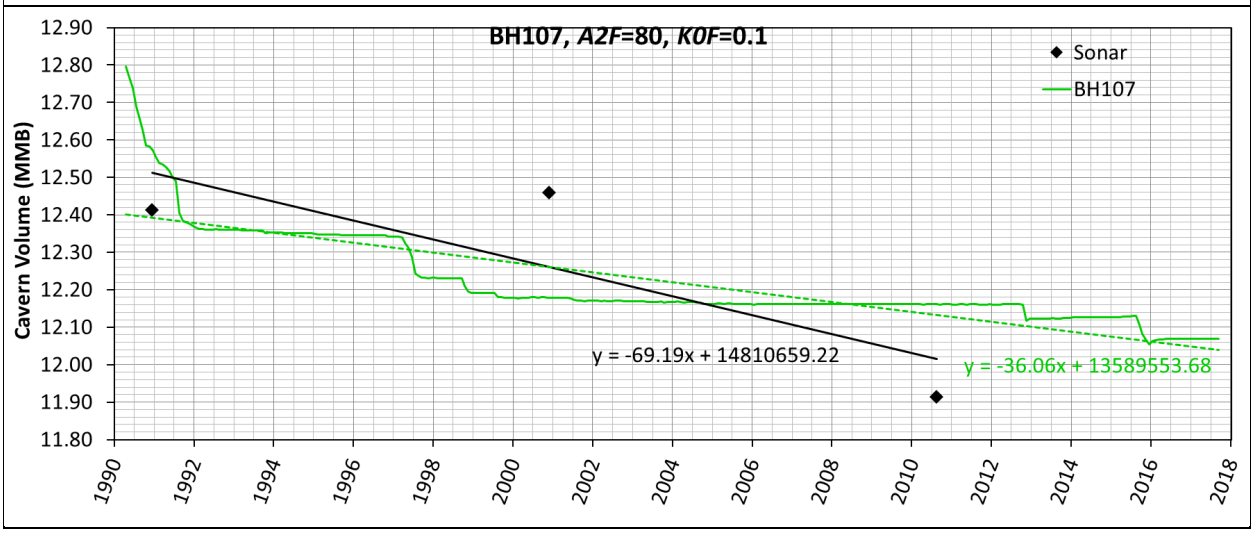
BH107, A2F=80, K0F=0.1
Sonar
BH107
Cavern Volume (MMB)
y = -69.19x + 14810659.22
y = -36.06x + 13589553.68
12.90
12.80
12.70
12.60
12.50
12.40
12.30
12.20
12.10
12.00
11.90
11.80
1990
1992
1994
1996
1998
2000
2002
2004
2006
2008
2010
2012
2014
2016
2018

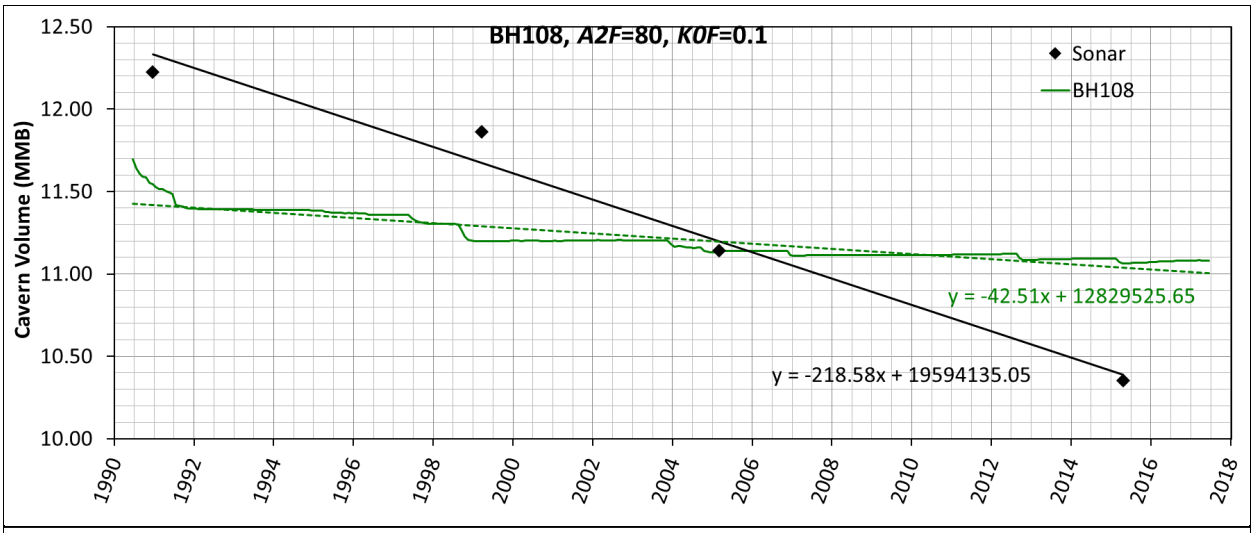
BH108, A2F=80, K0F=0.1
Sonar
BH108
Cavern Volume (MMB)
y = -42.51x + 12829525.65
y = -218.58x + 19594135.05
12.50
12.00
11.50
11.00
10.50
10.00
1990
1992
1994
1996
1998
2000
2002
2004
2006
2008
2010
2012
2014
2016
2018

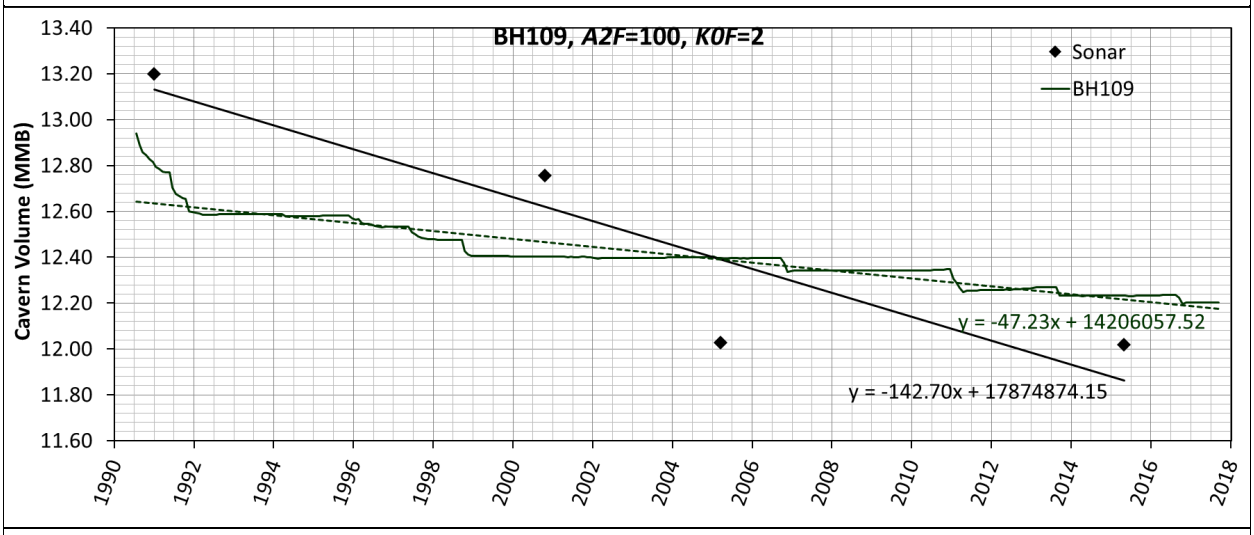
BH109, A2F=100, K0F=2
Sonar
BH109
Cavern Volume (MMB)
y = -47.23x + 14206057.52
y = -142.70x + 17874874.15
13.40
13.20
13.00
12.80
12.60
12.40
12.20
12.00
11.80
11.60
1990
1992
1994
1996
1998
2000
2002
2004
2006
2008
2010
2012
2014
2016
2018

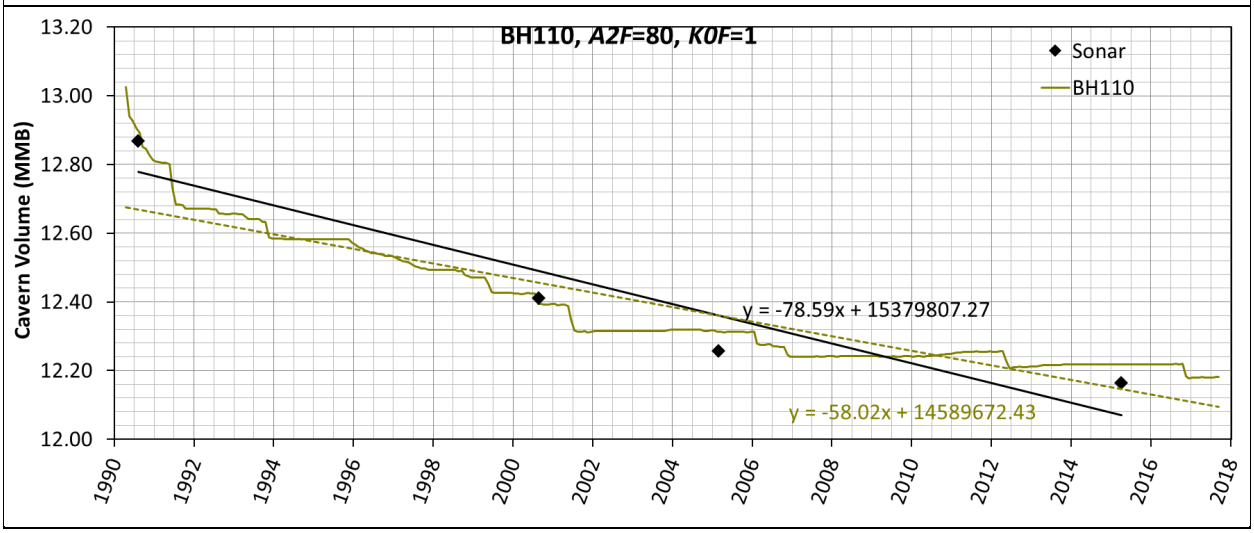
BH110, A2F=80, K0F=1
Sonar
BH110
Cavern Volume (MMB)
y = -78.59x + 15379807.27
y = -58.02x + 14589672.43
13.20
13.00
12.80
12.60
12.40
12.20
12.00
1990
1992
1994
1996
1998
2000
2002
2004
2006
2008
2010
2012
2014
2016
2018

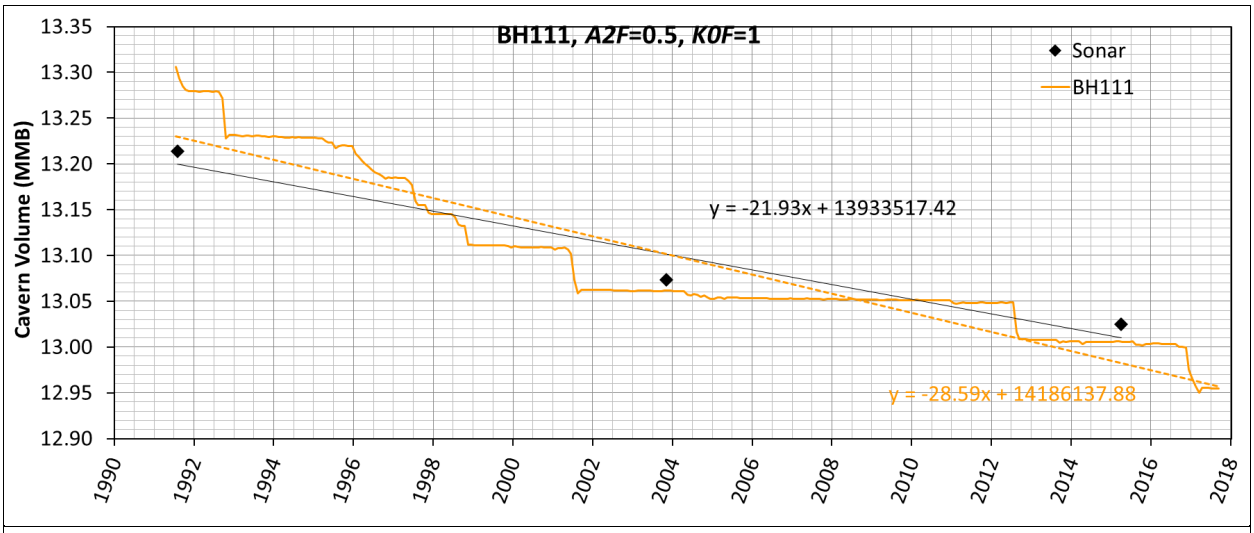
BH111, A2F=0.5, K0F=1
Sonar
BH111
y = -21.93x + 13933517.42
y = -28.59x + 14186137.88
Cavern Volume (MMB)
13.35
13.30
13.25
13.20
13.15
13.10
13.05
13.00
12.95
12.90
1990
1992
1994
1996
1998
2000
2002
2004
2006
2008
2010
2012
2014
2016
2018

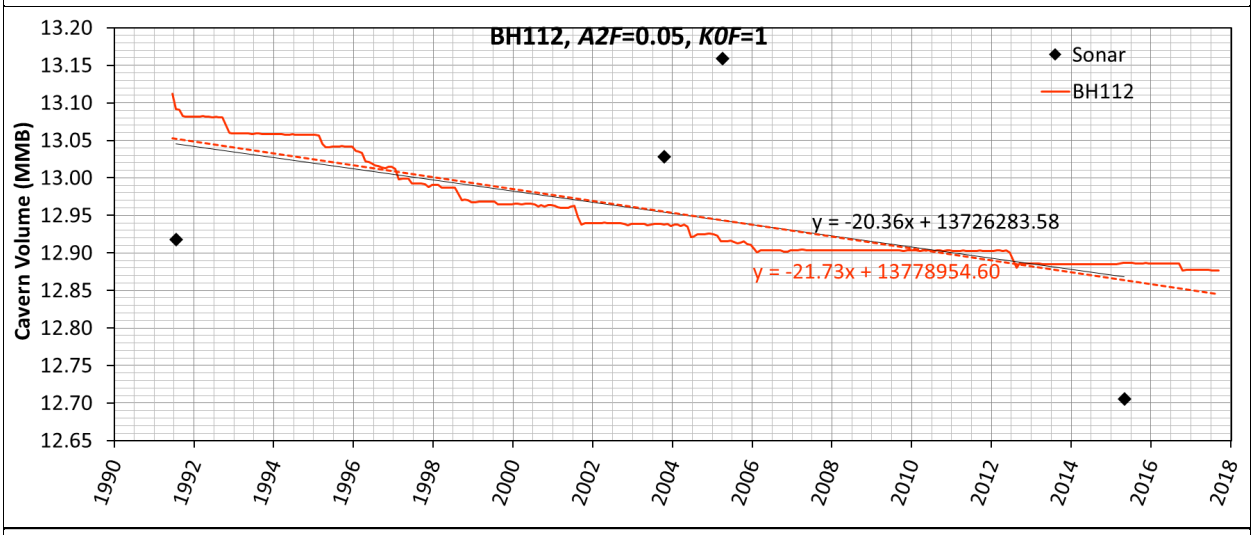
BH112, A2F=0.05, K0F=1
Sonar
BH112
y = -20.36x + 13726283.58
y = -21.73x + 13778954.60
Cavern Volume (MMB)
13.20
13.15
13.10
13.05
13.00
12.95
12.90
12.85
12.80
12.75
12.70
12.65
1990
1992
1994
1996
1998
2000
2002
2004
2006
2008
2010
2012
2014
2016
2018

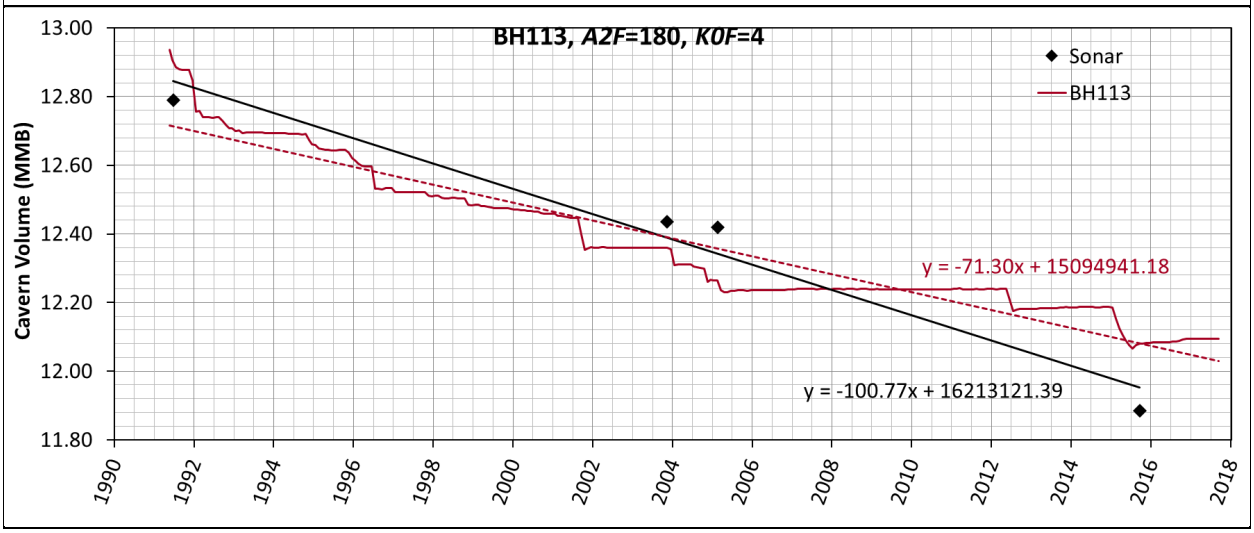
BH113, A2F=180, K0F=4
Sonar
BH113
y = -71.30x + 15094941.18
y = -100.77x + 16213121.39
Cavern Volume (MMB)
13.00
12.80
12.60
12.40
12.20
12.00
11.80
1990
1992
1994
1996
1998
2000
2002
2004
2006
2008
2010
2012
2014
2016
2018

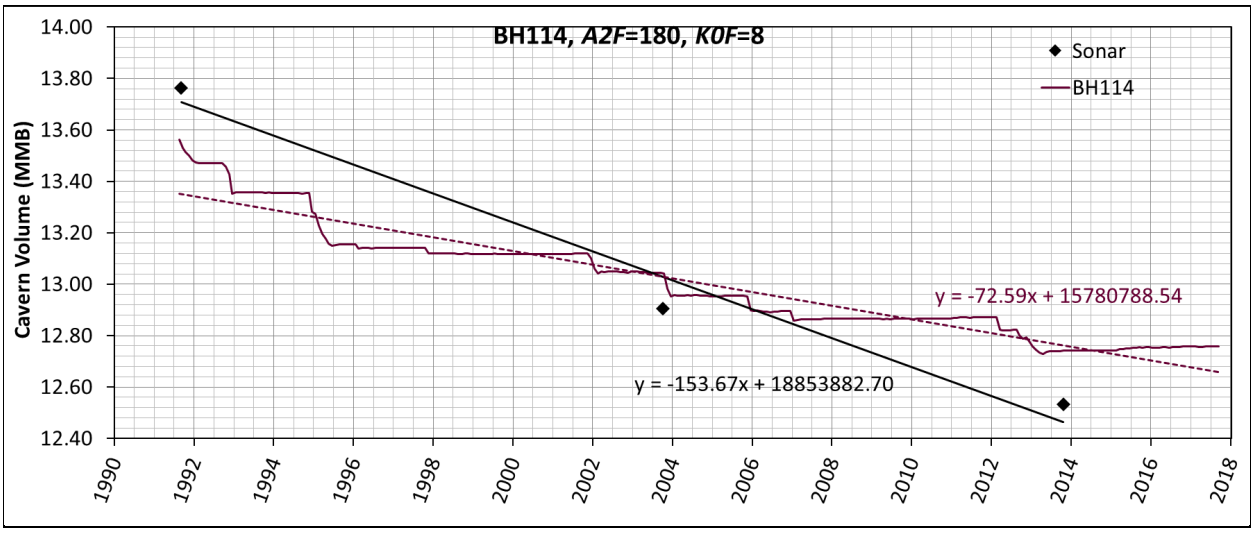

Figure 34. Predicted individual cavern volumetric change over time with *A2F* and *K0F* values in Table 7; and sonar measurements considering leached volume with linear trendlines. Units of the numbers in equations on the chart are bbl/day for slope, and bbl for intercept

This page left blank

8. SUMMARY AND DISCUSSIONS

The numerical analysis model, which consists of a realistic mesh capturing the geometries of the Big Hill SPR site and M-D salt constitutive model using the daily wellhead pressure data and oil-brine interface depth obtained from the field office, has been upgraded. The upgraded model contains the shear zone to examine the interbed behavior in a realistic manner. Calibration exercises have been performed to attempt to match model predictions of cavern volumetric closure with field measurements. The salt creep rate is not uniform across the salt dome and the creep test data of BH salt is limited. Therefore, model calibration is necessary to correctly simulate the geomechanical behavior of the salt dome.

The structure factor, A_2, and transient strain limit factor, K_0, in the M-D constitutive model were used as the calibration factors. The A_2 value obtained experimentally from BH salt and K_0 value of WIPP salt are used for the baseline values. To adjust the magnitude of A_2 and K_0, multiplication factors *A2F* and *K0F* are defined, respectively. The *A2F* and *K0F* values of the salt dome have been determined to be 100 and 1.0, respectively, through a number of back fitting analyses. The value for the salt skins surrounding each cavern has also been determined to meet the different salt creep rate at each cavern location.

The cavern volumetric closures calculated from the new model do not match those from CAVEMAN during the periods between workovers of each cavern. The cavern volume change estimated by CAVEMAN is probably unreliable, because CAVEMAN was developed for monitoring a cavern pressure from which cavern volume closure is calculated. Instead, sonar measurement data can be and is used as the field reference for calibrating the analysis model in this study, since the sonar surveyed cavern volume should be more direct measurement than the CAVEMAN estimation.

The A_2 and K_0 values are calibrated to produce the best match between the sonar measurement and model predictions. The multiplication factor values of *A2F* and *K0F* are determined through the back-fitting analyses. The trendlines of the predictions and sonar data matchup well for BH 101, 103, 104, 106, 110, 111, 112, and 113. The sonar data are close to the predicted curves for BH 102 and 114. However, the predicted curves for BH 105, 107, 108, and 109 have a fairly large discrepancy compared to the sonar data. There is an inconsistency in the sonar data, i.e. the sonar measurements increase during some periods for BH 101, 104, 106, 107, and 112. The causes might be the followings:

1. Uncertainty in the sonar measurements – The cavern volume measured by the sonar survey is known to have an error of about ±9%, and the sonar measurement techniques and methods used in the 1990s and 2000s have changed.
2. Leak of data - There is no row water injection data prior to 1997.

There is a limitation to calibrate the prediction using *A2F* and *K0F* because the closure rates increase until a certain value of them, but decrease after that. Project discussions are needed to determine possibilities on how to resolve the issues and determine the best path forward for future computer modeling attempts. The shear zone in the salt dome is not considered, but only in the caprock layers in this study. The comparison of the results between with and without considering the shear zone in the salt dome is needed in the future work.

This page left blank

REFERENCES

Ballard, S. and Ehgartner, B.L., 2000. *CAVEMAN Version 3.0: System for SPR Cavern Pressure Analysis,* SAND2000-1751, Sandia National Laboratories, Albuquerque, NM 87185-0750.

Blanford, M.L., M.W. Heinstein, and S.W. Key, 2001. *JAS3D. A Multi-Strategy Iterative Code for Solid Mechanics Analysis. User's Instructions, Release 2.0*. SEACAS Library, JAS3D Manuals, Computational Solid Mechanics / Structural Dynamics, Sandia National Laboratories, Albuquerque, New Mexico.

Bettin, G., D. Hart, A. Lord, B.Y. Park, B. Roberts, and S. Sobolik, 2018. *Geotechnical Analysis with Regards to Possible Site Closure Decision*, HQ report requested by DOE headquarters on May 23, 2018, Sandia National Laboratories, Albuquerque, New Mexico.

Butcher, B.M. 1997. *A Summary of the Sources of Input Parameter Values for the WIPP Final Porosity Surface Calculations*, SAND97-0796, Albuquerque, NM: Sandia National Laboratories.

Ehgartner, B., S. Ballard, M. Tavares, S. Yeh, T. Hinkebein, and R. Ostensen, 1995. *A Predictive Model for Pressurization of SPR Caverns*, Fall Meeting Solution Mining Research Institute, October 23-24, San Antonio, TX

Ehgartner, B.L. and Bauer, S., 2004, *Large Scale Salt Deformation: Comments on Subsidence using thermal, creep and Dissolution modeling to assess volumetric strain*, SAND2004-0095C, Sandia National Laboratories, Albuquerque, NM 87185.

Hart, D.B., 2018. *Month-by-month raw water movements from 1997 to 9/29/2017*, e-mail to B.Y. Park on 7/18/2018, Excel spread sheets, Sandia National Laboratories, Albuquerque, New Mexico.

Hoffman, E.L. and Ehgartner, B.L., 1992. *Evaluating the Effects of the Number of Caverns on the Performance of Underground Oil Storage Facilities*, SAND92-2183C, Sandia National Laboratories, Albuquerque, New Mexico.

Hogan, R.G., 1980. *Strategic Petroleum Reserve (SPR) Geological Site Characterization Report Bayou Choctaw Salt Dome*, SAND80-7140, Sandia National Laboratories, Albuquerque, New Mexico.

Hull, J., 1988. Thickness-displacement relationships for deformation zones, *J. Struct. Geol.,* 10, 431-435.

Lama, R.D. and V.S. Vutukuri, 1978. *Handbook on Mechanical Properties of Rocks – Testing Techniques and Results* -, Series on Rock and Soil Mechanics, Vol. 3, No.2, Trans Tech Publications.

Linn J.K., 1997. Memorandum to R.E. Myers, November 25, 1997 with attachment on *SPR Ullage Study* by B.L. Ehgartner, Sandia National Laboratories, Albuquerque, New Mexico.

Magorian, T.R., and J.T. Neal, 1988. *Strategic Petroleum Reserve (SPR) Additional Geologic Site Characterization Studies Big Hill Salt Dome*, Texas, SAND88-2267, Sandia National Laboratories, Albuquerque, NM.

Munson, D.E., 1979. *Preliminary Deformation-Mechanism Map for Salt (with Application to WIPP)*, SAND70-0079, Sandia National Laboratories, Albuquerque, New Mexico.

Munson, D.E. and P.R. Dawson, 1979. *Constitutive Model for the Low Temperature Creep of Salt (With Application to WIPP).* SAND79-1853, Sandia National Laboratories, Albuquerque, New Mexico.

Munson, D.E. and P.R. Dawson. 1982. *A Transient Creep Model for Salt during Stress Loading and Unloading*. SAND82-0962, Sandia National Laboratories, Albuquerque, New Mexico.

Munson, D.E. and P.R. Dawson, 1984. Salt Constitutive Modeling using Mechanism Maps. *1st International Conference on the Mechanical Behavior of Salt, Trans Tech Publications*, 717-737, Clausthal, Germany.

Munson, D.E., A.F. Fossum, and P.E. Senseny. 1989. *Advances in Resolution of Discrepancies between Predicted and Measured in Situ WIPP Room Closures*. SAND88-2948, Sandia National Laboratories, Albuquerque, New Mexico.

Munson, D.E., 1998. *Analysis of Multistage and Other Creep Data for Domal Salts*, SAND98-2276, Sandia National Laboratories, Albuquerque, New Mexico.

Munson, D.E., 2000. *Relative Evaluation of the Independent Volume Measures of Caverns*, SAND2000-2041, Sandia National Laboratories, Albuquerque, New Mexico.

Park, B.Y., B.L. Ehgartner, M.Y. Lee, and S.R. Sobolik, 2005. *Three Dimensional Simulation for Big Hill Strategic Petroleum Reserve (SPR)*, SAND2005-3216, Sandia National Laboratories, Albuquerque, NM.

Park, B.Y., Herrick, C.G, Ehgartner, B.L., Lee, M.Y., and Sobolik, S.R., 2006. Numerical Simulation Evaluating the Structural Integrity of SPR Caverns in the Big Hill Salt Dome, *The 41st U.S. Symposium on Rock Mechanics (USRMS): "50 Years of Rock Mechanics - Landmarks and Future Challenges.", held in Golden, Colorado, June 17-21, 2006.*, ARMA/USRMS 06-924.

Park, B.Y. and B.L. Ehgartner, 2011. *Allowable Pillar to Diameter Ratio for Strategic Petroleum Reserve Caverns,* SAND2011-2896, Sandia National Laboratories, Albuquerque, New Mexico.

Park, B.Y. and B.L. Ehgartner, 2012. *Interface Modeling to Predict Well Casing Damage for Big Hill Strategic Petroleum Reserve*, SAND2012-1206, Sandia National Laboratories, Albuquerque, New Mexico.

Park, B.Y. 2014a. Interbed Modeling to Predict Wellbore Damage for Big Hill Strategic Petroleum Reserve. *Journal of Rock Mech Rock Eng (2014) 47:1551-1561*. DOI 10.1007/s00603-014-0572-2

Park, B.Y. 2014b. *Geomechanical Analysis to Predict the Oil Leak at the Wellbores in Big Hill Strategic Petroleum Reserve*, SAND2014-0669, Sandia National Laboratories, Albuquerque, NM.

Park, B.Y., Sobolik, S.R., & Herrick, C.G. 2014. Wellbore Deformations and Proposed Steel Casing Size for Remediation in Big Hill Strategic Petroleum Reserve. SAND 2014-1846 C, *Rock Mechanics for Natural Resources and Infrastructure, SBMR 2014 – ISRM Specialized Conference 09-13 September, Goiania, Brazil.* © CBMR/ABMS and ISRM, 2014.

Park, B.Y. and B.L. Roberts, 2015. *Construction of Hexahedral Elements Mesh Capturing Realistic Geometries of Bayou Choctaw SPR site*, SAND2015-7458, Sandia National Laboratories, Albuquerque, New Mexico.

Park, B. Y., Roberts, B. L., and Sobolik, S. R. 2017. Construction of hexahedral finite element mesh capturing realistic geometries of a petroleum reserve. *Finite Elements in Analysis and Design*, 135, 68–78. https://doi.org/10.1016/j.finel.2017.07.007

Park, B.Y. 2017. *Geomechanical Simulation of Bayou Choctaw Strategic Petroleum Reserve - Model Calibration*, SAND2017-2103, Sandia National Laboratories, Albuquerque, New Mexico.

Park, B. Y., S.R. Sobolik, and C.G. Herrick. 2018. Geomechanical Model Calibration Using Field Measurements for a Petroleum Reserve. *Journal of Rock Mechanics and Rock Engineering*, ISSN 0723-2632, https://doi.org/10.1007/s00603-017-1370-4

Park, B.Y. 2018. *Geomechanical Simulation of Big Hill Strategic Petroleum Reserve - Model Calibration*, SAND2018-13783, Sandia National Laboratories, Albuquerque, New Mexico.

Shipton, Z.K., A.M. Soden, J.D. Kirkpatrick, A.M. Bright, and R.J. Lunn, 2006. How thick is a fault? Fault displacement-thickness scaling revisited. In Abercrombie, R. (Eds) *Earthquakes: Radiated Energy and the Physics of Faulting*, pages pp. 193-198, AGU.

SIERRA Solid Mechanics Team, 2018. *Sierra/Solid Mechanics 4.50 User's Guide*. SAND2018-10673, Sandia National Laboratories, Albuquerque, New Mexico.

Sobolik, S.R. 2015. *Analysis of Cavern and Well Stability at the West Hackberry SPR Site Using a Full-Dome Model*, SAND2015-7401, and Sandia National Laboratories, Albuquerque, New Mexico.

Wawersik W. R., 1985. Memorandum to R.R. Beasley, January 3, 1985, "Creep Measurements on Big Hill Salt," Sandia National Laboratories, Albuquerque, NM.

This page left blank

DISTRIBUTION

Hardcopy—Internal

Number of Copies	Name	Org.	Mailstop
5	Carolyn L. Kirby	8862	MS0750
10	Byoung Y. Park	8862	MS0751

Email—External [redacted]

Name	Company Email Address	Company Name
Wayne Elias	wayne.elias@hq.doe.gov	U.S. Department of Energy Office of Fossil Energy Washington, DC
Diane Willard	diane.willard@spr.doe.gov	U.S. Department of Energy SPR Project Management Office New Orleans, LA

Email—Internal

Name	Org.	Sandia Email Address
Erik K. Webb	8860	ekwebb@sandia.gov
Kirsten Chojnicki	8862	kchojni@sandia.gov
Donald M. Conley	8862	dconley@sandia.gov
Dylan Michael Moriarty	8862	dmmoria@sandia.gov
Anna C. Snider Lord	8862	acsnide@sandia.gov
Barry L. Roberts	8862	blrober@sandia.gov
Steven R. Sobolik	8862	srsobol@sandia.gov
David Hart	8865	dbhart@sandia.gov
David Lord	8865	dllord@sandia.gov
Giorgia Bettin	8866	gbettin@sandia.gov
Technical Library	1977	libref@sandia.gov

This page left blank

Sandia National Laboratories is a multimission laboratory managed and operated by National Technology & Engineering Solutions of Sandia LLC, a wholly owned subsidiary of Honeywell International Inc. for the U.S. Department of Energy's National Nuclear Security Administration under contract DE-NA0003525.